Alma Mater Studiorum - Università di Bologna

DOTTORATO DI RICERCA IN

MECCANICA E SCIENZE AVANZATE DELL'INGEGNERIA

Ciclo 35

Settore Concorsuale: 09/A2 - MECCANICA APPLICATA ALLE MACCHINE

Settore Scientifico Disciplinare: ING-IND/13 - MECCANICA APPLICATA ALLE MACCHINE

PREVENTING WORKERS' MUSCULOSKELETAL DISORDERS WITH WEARABLE INERTIAL SENSORS: ERGONOMICS AND MODELLING OF PHYSICAL HUMAN-ROBOT INTERACTIONS

Presentata da: Giulia Avallone

Coordinatore Dottorato

Lorenzo Donati

Supervisore

Nicola Sancisi

Co-supervisore

Rocco Vertechy

Esame finale anno 2023

A Marco,

sei sempre con me.

Abstract

The most widespread work-related diseases are musculoskeletal disorders (MSD) caused by awkward postures and excessive effort to upper limb muscles during work operations. The use of wearable IMU sensors could monitor the workers constantly to prevent hazardous actions, thus diminishing work injuries. In this thesis, procedures are developed and tested for ergonomic analyses in a working environment, based on a commercial motion capture system (MoCap) made of 17 Inertial Measurement Units (IMUs). An IMU is usually made of a tri-axial gyroscope, a tri-axial accelerometer, and a tri-axial magnetometer that, through sensor fusion algorithms, estimates its attitude. Effective strategies for preventing MSD rely on various aspects that are all analyzed in this thesis: firstly, the accuracy of the IMU, depending on the chosen sensor and its calibration; secondly, the correct identification of the pose of each sensor on the worker's body; thirdly, the chosen multibody model, which must consider both the accuracy and the computational burden, to provide results in real-time; finally, the model scaling law, which defines the possibility of a fast and accurate personalization of the multibody model geometry on the worker's body. Moreover, the MSD can be diminished using collaborative robots (cobots) as assisted devices for complex or heavy operations to relieve the worker's effort during repetitive tasks. All these aspects are considered to test and show the efficiency and usability of inertial MoCap systems for assessing ergonomics evaluation in real-time and implementing safety control strategies in collaborative robotics. Validation is performed with several experimental tests, both to test the proposed procedures and to compare the results of real-time multibody models developed in this thesis with the results from commercial software. As an additional result, the positive effects of using cobots as assisted devices for reducing human effort in repetitive industrial tasks are also shown, to demonstrate the potential of wearable electronics in on-field ergonomics analyses for industrial applications.

Contents

Introduction

In an advanced society, the health of every citizen should be ensured and safeguarded through regulations that firstly guarantee health and safety at work. It is estimated by the European Agency for Safety and Health at Work that three out of five workers report musculoskeletal disorders (MSD) annually [1]. Uncontrolled tasks, such as excessive loads on the back and upper limbs, extended and prolonged awkward postures, or excessive movement repetitions increase the risk of injuries for workers and cause chronic and dysfunctional diseases. The reduction of MSD has not only ethical but also economic implications. Injuries at work are of dominant concern in many industrial fields because MSDs account for one-third of all workers' compensation costs. Effective prevention strategies reduce absenteeism and sick leaves, increase productivity, and save insurance and legal costs. However, the workers’ health is the most important motivation for prevention and one of the most robust investments for the company's future. In general, MSD could be prevented or largely reduced by designing an ergonomic workplace [2] where human physical conditions are at least as important as productivity. Implementing a health and safety strategy in the workplace helps to identify potential risks and significant hazards and to activate powerful risk reduction and prevention strategies [3].

In this context and within the paradigm of Industry 4.0, innovative technologies integrated into sensorized systems are powerful tools for monitoring humans and safeguarding their health. In this sense, the widespread of lightweight, accurate, and stable sensors can be used as passive tools to provide continuous measures of the risk of possible disorders for the workers in real-time or, at least, with fast and frequent evaluations. Furthermore, the ongoing growth of the collaborative robotics market is pushing the use of cobots in industrial scenarios, where humans work in strict collaboration with robotics systems without any protective fences. For example, the workers can manually guide the cobot to perform a specific task, while the robotic systems reduce human overload. Otherwise, the cobot can help humans for moving and lift excessive weights. Apart from advantages in the production, a safe human-robot collaboration could also favor the reduction of

MSD, but it requires the continuous monitoring of the distance between the human and the cobot, ensuring that no unintentional contact or dangerous situation could occur. In this case, new sensors can be used as active tools to devise new control strategies that minimize the risk for the worker during human-robot interaction.

Motion Capture (MoCap) systems are measuring devices for recording human motion. The most used MoCap system to define safety control strategies relies on markerless or marker-based systems. While the first group exploits RGBD or deep cameras for determining the shapes and the motion of humans, in marker-based systems, infrared cameras measure the 3D position of optoelectronic markers positioned in specific anatomical landmarks. The major drawbacks of these systems are that the detection fails when external objects obstruct the camera’s field of view, or if the surrounding lights are too bright or gloomy. Moreover, they work only in a restricted volume where the camera maintains good visibility. As an alternative, wearable inertial sensors are gaining growing interest for their high portability, small dimension, lightweight, and reduced cost [4], [5]. The peculiarity of these sensors is that they are directly positioned over the body to determine the joint angles, they do not suffer from occlusion and light problems, and they are usable both indoors and outdoors. Conversely, they must be light, soft, and safe and specifically designed to be comfortable for humans. The ideal would be a completely flexible system without cables that do not interfere in any sense with the working task, thus being easily acceptable by the workers for safeguarding their health.

Examples are inertial MoCap systems, where an Inertial Measurement Unit (IMU) is associated with each body segment. An IMU is made by a tri-axial gyroscope, a tri-axial accelerometer and, most of the time, by a tri-axial magnetometer. Through sensor fusion algorithms, the IMUs output their orientation in an earth coordinate frame [6]–[8]. Then, the attitude of each body segment is estimated by the IMU orientation signals. Generally, only orientation is determined from the measures, thus it is necessary to associate a biomechanical model to compute the position of the segments' motion. As a consequence, the goodness of human body tracking depends on the accuracy of the sensors' attitude estimation and on the fidelity of the biomechanical model used [4].

The thesis' objective is to evaluate the potentiality of using IMU MoCap systems, in conjunction with musculoskeletal modelling, as the principal actors to study and improve safety at work. The most impactful advantage of these MoCap systems is that they can work online. This characteristic can be used to estimate if the workers are assuming awkward postures or performing repetitive motions that could be dangerous for their health. Alternatively, the IMU data can be used within the robot control system to inform the robot about the pose of the human [9].

Moreover, if inertial MoCap systems are integrated with a measure of the loads exerted by the worker, for instance using additional force and torque sensors or an estimate based on a preliminary load evaluation, a musculoskeletal model of the worker can estimate the joint and muscle loads and detect if overloads occur, causing possible injuries. The limits for joints' angles and moments are defined by ergonomics standards, which gather different indices and protocols to perform a preventive risk assessment of the work and reduce musculoskeletal disorders. Thus, comparing the online estimation of posture and force applied to the human body with the standards' limits allows the determination of potentially dangerous situations in real time. In this case, the constant tracking of the workers' behaviour could be a promising and effective method to assess prevention risk strategy by warning the workers with visual or auditive feedback.

As already noted above, an effective strategy for preventing musculoskeletal disorders with wearable inertial sensors depends on different aspects: 1) the accuracy of the measuring system, i.e., the quality of the sensor and, in particular, of its calibration [10]; 2) the correct identification of the pose of the sensor on the subject, i.e., the so-called sensor-to-segment calibration [11], [12]; 3) the choice of the multibody model, which cannot only take into account the accuracy, but also the time required by each simulation and the possibility of providing results in real time; 4) the scaling law, which defines the possibility of a fast and accurate personalisation of the model geometry starting from a reduced set of measures on the subject. These points are important also for the second application considered here, related to the human-robot interaction with cobots. This Thesis will analyse and deal with all these aspects.

In particular, as for the choice of the model (point 3 above), while the calculous of joint angles and corresponding body poses are relatively straightforward to assess with IMU MoCap systems, the determination of joint moments and muscle effort is more complex. The resolution of human dynamics is intricate and an open-research topic in biomechanics. Usually, through global and static optimization resolution, commercial multibody software estimates the angle joints and muscle effort of complete and detailed musculoskeletal models[13], [14]. They represent the standard to perform both kinematic and dynamic evaluations of given motion tasks and are gaining growing interest in ergonomics assessments. However, these general models cannot work in real-time, thus they could have important limitations in some of the applications considered here. On the contrary, real-time simulations can be obtained using very simplified and custom models [15], [16] whose accuracy could be similar to the more complex and complete general models, if defined for the specific application. Thus, to evaluate the potentiality of both types of multibody models, both a commercial offline model [17] and a custom fast online model are tested for ergonomics assessment, in the same collaborative robotics scenario. In this way, the advantages of both approaches are described to guide the choice of the best solution for a specific application.

As for point 4 above, the goodness of the simulation results depends on the similarity between the simulated musculoskeletal model and the property of the subject human body analysed. The standard model has to be scaled and modified to respect the actual anthropometric measures, joint kinematic motion, and muscle and tendon characteristics of the subject. It has been shown that subject-specific musculoskeletal models, defined by specific joint geometry through MRI images or by sophisticated joint models, describe human motion behaviour and peculiarities better[18], [19]. However, a full personalisation of the model is unfeasible in real industrial scenarios. Thus, defining an automatic scaling law to identify musculoskeletal models with advanced joints characteristic is an interesting topic for increasing the overall accuracy of the considered applications.

Thus, this thesis has multiple objectives, which are treated individually in each chapter.

In the first chapter, an extensive study of the working principle of the IMU evaluates the strategies and the current methods to obtain a drift-less and noise-less computation of the attitude. One of the possible causes of errors is the accelerometer and gyroscope's noisy or incorrect output. A precise accelerometer and gyroscope output depend on the goodness evaluation of the mathematical terms that describe the possible errors over the sensor output. The sensor calibration identifies those values. Since commercial calibration methods require expensive equipment, a low-cost accelerometer and gyroscope calibration method is proposed and validated.

The second chapter describes the IMU MoCap algorithm implemented. For accurate motion estimation, the anthropometric model has to be very similar to the subject, and the orientation of each IMUs with respect to the attached bodies has to be determined precisely. In this chapter, a novel sensor-to-segment calibration procedure is proposed and tested.

The third chapter gathers the ergonomics assessments. After a detailed literature review on the use of wearable inertial sensors in ergonomics and the differences between standards, a collaborative robotics scenario is described. The operator hand guides the cobot in the drilling position and performs the drilling task with the help of the cobot. The IMU MoCap system tracks human motion, while a force and torque sensor measures the forces of interaction between the cobot and the subject. Thus, the multibody software simulates the physical human-robot interaction. The OCRA index, an ergonomic parameter that considers the motion range and the muscle effort and fatigue of shoulder, elbow, and wrist muscle in repetitive tasks, is calculated with commercial multibody software to mathematically estimate the advantages of using collaborative robotics in industrial applications for reducing musculoskeletal disorders. Moreover, an algorithm for estimating the upper-limbs human joint wrenches in real-time is defined and validated with the results obtained with the commercial software.

The fourth chapter, instead, evaluates the usability of IMUs for commanding the collision avoidance strategy of a redundant robot in the null space. The test wants to demonstrate the validity of the integration of IMU MoCap algorithms and the robot controller for safety purposes.

Finally, the fifth chapter describes the works made in collaboration with the University of Ottawa about automatic methods for scaling advanced and subject-specific knee joint models using PCA. The idea is to define a robust dataset to predict the knee kinematic features using the position of four markers during a static acquisition. The results of the proposed method are promising, even if we expect that more populated datasets will improve the estimation.

References

[1] European Agency for Safety and Health at Work., IKEI., e Panteia., *Work-related musculoskeletal disorders: prevalence, costs and demographics in the EU.* LU: Publications Office, 2019. Consultato: 22 ottobre 2022. [Online]. Disponibile su: https://data.europa.eu/doi/10.2802/66947

[2] G. C. David, «Ergonomic methods for assessing exposure to risk factors for work-related musculoskeletal disorders», *Occupational Medicine*, vol. 55, fasc. 3, pp. 190–199, mag. 2005, doi: 10.1093/occmed/kqi082.

[3] L. Peppoloni, A. Filippeschi, E. Ruffaldi, e C. A. Avizzano, «A novel wearable system for the online assessment of risk for biomechanical load in repetitive efforts», *International Journal of Industrial Ergonomics*, vol. 52, pp. 1–11, mar. 2016, doi: 10.1016/j.ergon.2015.07.002.

[4] D. Roetenberg, H. Luinge, e P. Slycke, «Xsens MVN: Full 6DOF Human Motion Tracking Using Miniature Inertial Sensors», p. 10, 2013.

[5] A. Filippeschi, N. Schmitz, M. Miezal, G. Bleser, E. Ruffaldi, e D. Stricker, «Survey of Motion Tracking Methods Based on Inertial Sensors: A Focus on Upper Limb Human Motion», *Sensors*, vol. 17, fasc. 6, p. 1257, giu. 2017, doi: 10.3390/s17061257.

[6] S. O. H. Madgwick, A. J. L. Harrison, e R. Vaidyanathan, «Estimation of IMU and MARG orientation using a gradient descent algorithm», in *2011 IEEE International Conference on Rehabilitation Robotics*, Zurich, giu. 2011, pp. 1–7. doi: 10.1109/ICORR.2011.5975346.

[7] R. Mahony, T. Hamel, e J.-M. Pflimlin, «Nonlinear Complementary Filters on the Special Orthogonal Group», *IEEE Trans. Automat. Contr.*, vol. 53, fasc. 5, pp. 1203–1218, giu. 2008, doi: 10.1109/TAC.2008.923738.

[8] A. M. Sabatini, «Quaternion-Based Extended Kalman Filter for Determining Orientation by Inertial and Magnetic Sensing», *IEEE Trans. Biomed. Eng.*, vol. 53, fasc. 7, pp. 1346–1356, lug. 2006, doi: 10.1109/TBME.2006.875664.

[9] M. Safeea, «Minimum distance calculation using laser scanner and IMUs for safe human-robot interaction», *Robotics and Computer Integrated Manufacturing*, p. 10, 2019.

[10] U. Qureshi e F. Golnaraghi, «An Algorithm for the In-Field Calibration of a MEMS IMU», *IEEE Sensors J.*, vol. 17, fasc. 22, pp. 7479–7486, nov. 2017, doi: 10.1109/JSEN.2017.2751572.

[11] B. Bouvier, S. Duprey, L. Claudon, R. Dumas, e A. Savescu, «Upper Limb Kinematics Using Inertial and Magnetic Sensors: Comparison of Sensor-to-

Segment Calibrations», *Sensors*, vol. 15, fasc. 8, pp. 18813–18833, lug. 2015, doi: 10.3390/s150818813.

[12] N. Choe, H. Zhao, S. Qiu, e Y. So, «A sensor-to-segment calibration method for motion capture system based on low cost MIMU», *Measurement*, vol. 131, pp. 490–500, gen. 2019, doi: 10.1016/j.measurement.2018.07.078.

[13] S. L. Delp *et al.*, «OpenSim: Open-Source Software to Create and Analyze Dynamic Simulations of Movement», *IEEE Trans. Biomed. Eng.*, vol. 54, fasc. 11, pp. 1940–1950, nov. 2007, doi: 10.1109/TBME.2007.901024.

[14] M. Damsgaard, J. Rasmussen, S. T. Christensen, E. Surma, e M. de Zee, «Analysis of musculoskeletal systems in the AnyBody Modeling System», *Simulation Modelling Practice and Theory*, vol. 14, fasc. 8, pp. 1100–1111, nov. 2006, doi: 10.1016/j.simpat.2006.09.001.

[15] C. Latella *et al.*, «Towards real-time whole-body human dynamics estimation through probabilistic sensor fusion algorithms: A physical human–robot interaction case study», *Auton Robot*, vol. 43, fasc. 6, pp. 1591–1603, ago. 2019, doi: 10.1007/s10514-018-9808-4.

[16] W. Kim, J. Lee, N. Tsagarakis, e A. Ajoudani, «A real-time and reduced-complexity approach to the detection and monitoring of static joint overloading in humans», in *2017 International Conference on Rehabilitation Robotics (ICORR)*, London, lug. 2017, pp. 828–834. doi: 10.1109/ICORR.2017.8009351.

[17] M. E. Lund, S. Tørholm, Divyaksh S. Chander, e J. Menze, «The AnyBody Managed Model Repository (AMMR)». Zenodo, 8 luglio 2022. Consultato: 25 ottobre 2022. [Online]. Disponibile su: https://zenodo.org/record/6809697

[18] M. Conconi, N. Sancisi, e V. Parenti-Castelli, «Prediction of Individual Knee Kinematics From an MRI Representation of the Articular Surfaces», *IEEE Trans. Biomed. Eng.*, vol. 68, fasc. 3, pp. 1084–1092, mar. 2021, doi: 10.1109/TBME.2020.3018113.

[19] K. B. Smale *et al.*, «Effect of implementing magnetic resonance imaging for patient-specific OpenSim models on lower-body kinematics and knee ligament lengths», *Journal of Biomechanics*, vol. 83, pp. 9–15, gen. 2019, doi: 10.1016/j.jbiomech.2018.11.016.

.

Chapter 1

Inertial Measurements Units

The development of micro-electro-mechanical systems (MEMS) has enabled low-cost, low-power, light, and small-sized sensors, spreading their use in several applications. An example is MEMS Inertial Measurement Units (IMUs), sensors able to estimate their poses. Their first use was for aerial vehicles' attitude estimation, but nowadays, their use has spread to automotive, robotics, body motion tracking, rehabilitation, medicine, and clinical navigation industries. For example, automotive industries use single MEMS gyroscopes for car electronic stability control, and smartphone and drone companies use MEMS accelerometers as inclinometers for pose estimation. Healthcare industries utilize IMU for measuring clinically relevant motion patients' outcomes or as supportive devices in orthopaedics and laparoscopic surgery.

In fact, the small dimensions and lightness of MEMS IMUs have promoted their use in wearable networks of sensors for Motion Capture (MoCap) systems, which identifies the discipline that digitally tracks and records the movements of objects or living beings in spaces [1]. The biggest challenge in motion tracking is to reach high accuracy with non-invasive sensors in an unlimited workspace, such as to measure body motion in complex and various environments without losing accuracy. The most common MoCap devices are camera-based systems, divided into marker-based or marker-less solutions. The first group relies on infrared (IR) cameras, which triangulate the locations of retroreflective markers attached to the targeted subjects. The second one exploits the potentiality of depth-sensitive cameras that project light toward the objects and estimate its depth based on the time delay from light emission to backscattered light detection, or more common

Figure 1 *Commercial IMU MoCap system and a single IMU sensor*

RGB cameras. The major drawbacks of these systems are time-consuming and frequent calibration, a restricted working area, and light and occlusion problems. Conversely, IMUs' MoCap can be used outdoors and indoors and represent validated instrumentation for measuring human movements in clinical, video games, and entertainment. In the last few years, it has become an enabling technology for several industrial applications, such as localization, human-robot interaction, rehabilitation, and ergonomics. This development is due to the increasing number of manufacturing companies, such as General Electric Company (U.S.), Bosch GmbH (Germany), Xsense (Netherlands), or start-ups that manufacture and sell IMU as a single sensor or as an integrated MoCap system with its specific software. Figure 1 shows a commercial MoCap wearable suit and a single IMU.

An IMU consists of a tri-axial accelerometer and a tri-axial gyroscope, sometimes integrated with a tri-axial magnetometer. A gyroscope measures the angular velocity, whereas the accelerometer senses the linear acceleration including gravity. A magnetometer measures the geomagnetic field vector to gather information about its orientation with respect to the north pole. The sensitive axes of these three sensors are aligned together and define a technical coordinate system (TCS) physically attached to the IMU case. The gravity vector in TCS estimates the pitch angle, while the magnetic field vector assesses the orientation with respect to the yaw axis. Mathematically, the gyroscope signals integration provides a first estimation of the sensor pose, corrected by the acceleration after subtraction of the gravity vector [2]–[4]. Since both the gyroscope and accelerometer suffer from time-varying biases and noise, their integration implicates drifting, mitigated by magnetometer estimation.

The literature collects several sensor fusion techniques for the attitude assessment from all the signals gathered. In most cases, the filters adopted are complementary and Kalman filters: the attitude is calculated in discrete settings at successive time steps based on previous time step estimation and current time step measures [5]. Researchers have proposed several filter formulations with different mathematical orientation representations, various filter designs, or distinct strategies to fuse signal information. Despite the number of papers that compare sensor fusion algorithms in testing scenarios [6]–[10], it is difficult to identify the “best” algorithm and filtering approach [11]. Moreover, the results of the same sensor fusion algorithms differ between different studies due to various experimental conditions (rotation rates, acceleration magnitude, ferromagnetic disturbances, types of motion, etc.). The IMU orientation output has been compared with the one obtained with optical markers positioned on the human body [8], in a gimbal table [6], pendulum [9], or differently using robotic systems [7] that can control and replicate frequency and initial orientation of the IMU. The latter experimental setup proves that absolute accuracy in attitude estimation depends on aptitude, frequency, and motion direction. Differences in performance are evident with rotation against and along the gravity axis. In these cases, the correction effect of the magnetometer fails to reduce the drifting error. There are no statistically significant differences between several sensor fusion algorithms; however, appropriate filter parameters and tuning set selection are fundamental for incrementing accuracy [11]. Deep knowledge of the sensors' output parameters, such as noise distribution or bias, is necessary for increasing the goodness in modelling the sensor estimation and tuning the sensor fusion algorithms. One of the methods for determining the sensors ‘characteristics is calibration. The raw sensor data, usually voltage signals proportional to the sensed physical dimension, are compared with known reference outputs for determining the parameters that transform the raw data into meaningful values. The more the calibration can fully describe the model parameters, the more the sensor output is noise and bias-free. This fact reduces the drifting error caused by signal integration and produces a more stable and correct attitude estimation. Thus, a rigorous calibration procedure permits to have IMUs more performing for evaluating human motion and, consequently, safety at work.

This chapter gives an overview of the IMU sensors in a general sense: it explains the working principle and the most common sensor error model of accelerometers, gyroscopes, and magnetometers. Sensor calibration is necessary to estimate the values that accurately describe each sensor's output, such as bias, noise, and scale factors. Since commercial calibration instrumentations are expensive, we propose a low-cost calibration method for gyroscopes and accelerometers, exploiting the free fall motion of a pendulum. Results and the sensitivity analysis of this approach are described in the last section.

1.1 Working principle

1.1.1 Gyroscope

A gyroscope is a device mounted on a 3D frame able to sense angular velocity components along each axis. The first pioneering instrumentation to accomplish the scope measured the torque necessary to change the orientation of a spinning body rotating about its axis. A second version was introduced in 1852 by the physicist Léon Foucault, who installed the spinning disc on a gimbal allowing it to navigate freely in the three directions. When the spinning axis rotates, it maintains its spin axis direction fixed regardless the orientation of the outer frame, according to the conservation of the angular momentum. Later the spinning body was substituted by a vibrating element to miniaturize the system. Therefore, a MEMS gyroscope is built using silicon micro-machining techniques and consists of a mass, m, driven to vibrate along an axis with a given frequency. The in-plane velocity v of the mass is dependent of the frequency and its cosine. The mass can move only in one direction and is tethered to a polysilicon frame. When an angular velocity ω is applied to the sensor, a secondary vibration is induced perpendicular to the vibrating axis due to the Coriolis force, which is equal to:

$$F_c = -2m(\omega \wedge v) \tag{1}$$

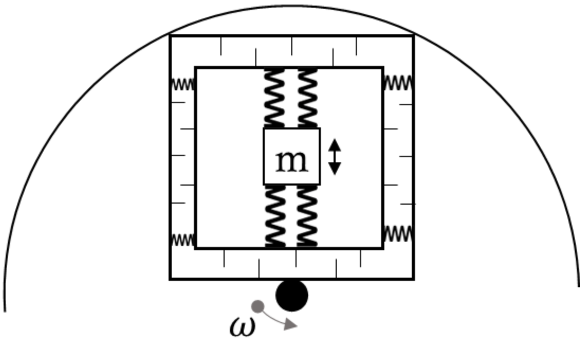

Figure 2 Schematic representation of the gyroscope working principle

The polysilicon frame is attached to a substrate with springs positioned perpendicular to the vibrating axis and is free to move. An external frame contains sense fingers that measure the displacement due to the motion through capacitive transducers in response to the force exerted by the mass. Figure 2 shows a schematic representation of the gyroscope. If the entire structure rotates, the resonating mass and the frame move under the Coriolis acceleration. As the rate of rotation increases, so do the displacement due to the Coriolis force and the signals captured. However, the Coriolis acceleration is so little to produce small capacitance changes, thus must be amplified by an integrated circuit.

Ideally, a gyroscope would be sensitive only to rotation rate, but in practice, it is sensitive to acceleration due to asymmetry of its mechanical designs and micromachining inaccuracies.

The errors in the gyro output influence the accuracy of the angle reconstruction. The performance factor of the gyroscope can be classified into five parameters [12]:

1. Angles Random Walk (ARW) defines the broadband white noise present in the gyro output due to thermo-mechanical noise. It is caused by the constant vibration of the mass and noises over the detection electronics, which fluctuates at a rate much greater than the sensor sampling rate [13]. It is evaluated through the Allan variance technique.
2. Bias Offset Error defines the error in the nonzero output when the rotation is null. It is dependent on different temperatures but fixed for each of them. Thus, it can be easily individuated and corrected.
3. Bias Instability describes the instability over temperatures of Bias Offset Error. Its effect is impactful in long measurement periods and thus is difficult to calibrate. Allan variance technique identifies this error.
4. Temperature Sensitivity describes the negative effect of temperature on the gyro sensor.
5. Shock and Vibration Sensitivity identify the noise and bias offset degradation under vibration and shock input.

Finally, “calibration errors” [13] describe those errors strictly dependent on the calibration procedure: scale factors and alignment factors. While the scale factor converts the raw sensor signals in standard metric systems, the alignment factors identify the possible micromachining non-orthogonality errors between the sensitive axes. These errors, which noise the sensor outputs, accumulate during the integration procedure comporting an additional drift but can be mitigated by an effective calibration procedure.

1.1.2 Accelerometer

The MEMS accelerometers are sensors able to detect linear acceleration along the three axes. They can be divided into two distinct classes depending on the sensing modality [14]. In one case, the output depends on the displacement of a proof mass supported by a hinge or flexure, whereas in the other case, the linear acceleration is related to a change in the frequency of a vibrating mass element. The first case comprehends the popular pendulous-mass accelerometers, which consist of a silicon substrate. When an external motion determines a sensor's acceleration, specific electrodes measure the movements between the proof mass and the substrate. According to the working principle exploited to measure this gap variation, MEMS accelerometers can be divided into piezoresistive, piezoelectric, capacitive, tunnel, resonant, electromagnetic, thermocouple, optical, inductive, etc. [15]. Since the mass value, the hinge's elastic constant, and the displacements due to the motion are known, the linear acceleration of the system perpendicular to the plane is obtained through the Hooke law and the second principle of dynamics. Usually, three perpendicular pendulum-mass accelerometers compose the three-axial MEMS accelerometer. The advantage is its versatility of being packed in small electronic devices, and as for gyroscopes, they are small, low-power, and light. Figure 3 shows an example of MEMS accelerometer.

Similar to gyroscope the error characteristics are [13]:

1. The constant bias, which is estimable knowing the precise orientation of the device with respect to the gravity vector averaging long-term outputs.
2. Velocity Random Walk which is influenced by the electronic noise of the sensor.
3. Bias instability that causes the bias to wander over time.

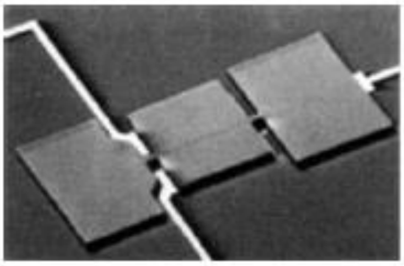

Figure 3 MEMS accelerometer

4. Temperature effect that, like the gyroscope, causes fluctuation in the bias of output signal and depends specifically on the devices and is often highly nonlinear.

Then calibration is necessary to identify both the scale factor and axis misalignment and will be described in the section 2.

1.1.3 Magnetometer

The convection currents of a mixture of molten iron and nickel in the Earth's core, due to the natural process of the geodynamo, create a magnetic field that makes the Earth a magnetic dipole. The magnitude of the magnetic field varies on the Earth's surface ranging from 25 to 65 µT. Its direction is described with the declination and the inclination angles, which are the angle with the north-south geographic axis and the Earth's surface, respectively.

MEMS magnetometers are devices that measure the strength and direction of a magnetic field and are classified into two main groups: sensors exploiting the force generated by the response of ferromagnetic materials deposited on top of the silicon structures [16], and sensors based on the Lorentz-Force principle. Here a low-resistivity silicon structure is suspended over the glass substrate by torsional beams, fixed by anchors bonded onto the substrate. An excitation coil with a known length is above the silicon structure and activated by a direct current. If a magnetic field perpendicular to it is present, the Lorenz forces generated perpendicular to the two planes cause movements of the suspended mass, which can be sensed in multiple ways, such as capacitive, piezoresistive, and optical [17].

The Lorenz force is generated by the sum of the Earth's magnetic field and any local fields present in the sensor proximity. The latter are due to ferromagnetic materials, electric motors, payload instruments, and attitude control torquers

[18]. A performing calibration procedure allows estimation of the local fields and their compensation.

The main magnetometer error characteristics are:

1. The constant Bias Error that, differently from the gyroscope, seems to remain constant for the entire lifespan of the sensor [19].
2. The non-orthogonality error, which is the misalignment between the direction of each sensitive axis.
3. Cross Axis Sensitivity errors that cause a variation of the magnitude sensed by each axis, varying the scale factors.
4. Sensor noise is due to the noise over the electronics and is a stochastic process.
5. Temperature dependence of the calibration parameters.
6. Magnetic Field Specific Errors due to the magnetic perturbation, and it is divided into:
    - Hard Iron effect, resulting from permanent magnets and magnetic hysteresis of the sensor components.
    - Soft Iron effect, due to the interaction with ferromagnetic compounds that induces external magnetic fields that changes both the intensity and the direction of the sensed field.

If we rotate a perfectly calibrated magnetometer not surrounded by any ferromagnetic materials, it will sense a constant magnetic field. Output lies on a sphere centred at the origin of the reference system. The soft iron effect distorts the sphere that becomes an ellipsoid, while the hard iron effects offset the ellipsoid centre from the origin. Thus one of the most used algorithms to calibrate the magnetometer and identify the magnetic disturbances in a specific field relies on an ellipsoid fitting problem over the theoretical sphere[19]–[21]. The benefits of using this approach are that the ellipsoid fitting problem is widely studied in the literature, and the movement is easy to implement and perform. It is sufficient to fit a sphere over the magnetometer output sensed by performing roughly 360° sensor rotations. This process should be done during the setting phase of the magnetometer in a new environment for detecting and correcting all external disturbances.

1.1.4 Sensor fusion algorithm

Data from the gyroscope, accelerometer, and magnetometer are fused to determine the sensor attitude through the sensor fusion algorithm. Usually, rotation matrices, Euler angles, and director cosine express spatial orientation. However, recently almost all algorithms rely on unit quaternion representation, which parametrizes the rotation with four variables and, compared to the other parametrizations, does not suffer from the gimbal lock problem, thus avoiding singularities [22], and reducing computational costs. Moreover, the quaternion derivative is easily defined and used to represent angular velocity.

The objective of sensor fusion algorithms is to use the information gathered from all the available sensors and express the orientation of the sensor's technical frame (TCS), defined by its sensitive axes, in the Earth coordinate system (ECS). The latter is a universal reference frame commonly used in navigation practices, characterized by an axis pointing to the north pole, one along the gravity direction, and the last composing the right-handed triad. The quaternion derivative (${}^{ECS}_{TCS}\dot{\boldsymbol{q}}$), describing the rate of change of the sensor's TCS orientation in ECS (${}^{ECS}_{TCS}\boldsymbol{q}$), is correlated with the gyroscope output with [2]:

$$ {}^{ECS}_{TCS}\dot{\boldsymbol{q}} = \frac{1}{2}\,{}^{ECS}_{TCS}\boldsymbol{q} \otimes \boldsymbol{\omega}^{s} = \frac{1}{2}\,{}^{ECS}_{TCS}\boldsymbol{q} \otimes [0 \quad \omega_x^s \quad \omega_y^s \quad \omega_z^s] \tag{2} $$

where ⊗ identifies the Hamiltonian product among quaternions, and $\boldsymbol{\omega}^{s}$ the angular velocity sensed by the gyroscope. Knowing the initial condition, this term can be numerically integrated to obtain the orientation of the sensor in the earth frame. Since the numerical integration of noisy signals suffers from drift, this first estimation is corrected using the information gathered from accelerometers and magnetometers. How these sensors are fused mostly differentiates the sensor fusion algorithms. Many methods exploit complementary filters: a “low frequency” attitude is estimated from the acceleration due to gravity and from the magnetometer through optimization resolution [3], [23] and fused with specific weights with the gyroscope attitude estimation. Most works ignore the effect of linear acceleration because it is much lower than the gravity vector, but others [24] add some kinematic constrain estimating the linear acceleration and subtracting it from the accelerometer signal. The most used algorithms rely on TRIAD [25], [26] and QUaternion ESTimation (QUEST) [27]. Both create triads from the accelerometer and magnetometer output and determine the suboptimal orientation estimation between the two systems with, respectively, a mathematical cross-product and minimization of a loss function. The latter two are very popular for their easy implementation and efficiency in real-time scenarios. Moreover, among sensor fusion algorithms, the Kalman filter [28]–[30], or the improved Extended Kalman filter [4], that deal with nonlinearities, are widely used. However, the number of works that treat sensor fusion algorithms is high, and they will not be discussed here. An excellent literature review is made by Filippeschi et al. [5], with a focus on the algorithm used for motion tracking of the upper limbs. As mentioned in the introduction of this chapter, it is difficult to assess which is the best strategy to fuse the information gathered by the IMUs, because the results are strongly dependent on experimental conditions. Firstly, it depends on the disturbances present in the environments: temperature variation, types of motion, and ferromagnetic perturbation. Secondly, it depends on the type of test performed: a rotation aligned to the gravity vector will reduce the gyroscope drift correction from the accelerometer output.

Research continues to investigate how to obtain robust attitude estimation working on several fronts: development of more stable sensor and electronic circuits able to reduce noise and temperature dependencies, improvement of the calibration procedure and mathematical sensor models that better describe the signal, implementation of new sensor fusion algorithm able to better estimate the attitude, and finally by integrating other sensors, such as GPS or cameras [31], [32], for correct the position calculation in 3D space.

1.2 Commercial IMU systems

Companies that sell IMUs generally use their algorithms with specific tuning parameters obtained during the calibration phase to estimates the sensor attitudes. Usually, they don’t specify the algorithm used, and they output the gyroscope, accelerometer, and magnetometer signals, as well as the attitude estimations in the forms of quaternion, Euler angles, or rotation matrices. In this way, the use of commercial IMU is dual: the raw sensor signals are proper to study and develop proprietary sensor fusion strategies; alternatively, the use of self-estimated sensor attitudes of several IMUs is fundamental for motion tracking implementation.

In this project, we studied and compared two commercial motion tracking systems: the Shadow® Mocap Suit (2022 Motion Workshop, USA) and the

ShowmotionTM (NCS Company SpA, ITA). The principal difference between the two systems is that Showmotion has wireless IMUs that transfer sensor data to a laptop with proprietary software. Differently, the IMUs of the Shadow Mocap Suit are connected by cable to a portable controller that hosts a Wi-Fi network. Each system provides raw data (accelerometer, magnetometer, and gyroscope) and the orientation represented in rotation matrix, Euler Angles, and quaternions.

The sensor fusion algorithm is unknown in both commercial systems.

- *Showmotion* IMU contains two accelerometers to augment the sensor redundancy and reduce noise and the drifting problem over the orientation estimation. Each IMU is positioned on the body through tapes and elastic bands after a set-up phase needed to connect each IMUs wirelessly to a USB antenna connected to the laptop. Frequency is dependent on the number of sensors and type and dimension of data transferred: for instance, for a typical upper limb and shoulder setup, 5 IMUs are needed, and, with standard data, frequency is 60 Hz [33]. Each IMU is equipped with LiPo batteries with a capacity of 240 mAh, which, if fully charged, has a run-time of 2.5-3 hours, depending on the data rate and temperature.
- *Shadow* system comprehends 17 IMUs and a pair of pressure insoles. A series of pockets sewn into a t-shirt fix the sensors of the body core, while elastic bands hold the IMUs over the limbs. The portable Wi-fi hub gathers five cables, each connecting 3 or 4 IMUs in series. The sampling rate can reach 1000 Hz if a single IMUs is used or 400 Hz if all the 17 sensors are connected. The output data can be treated in two ways: they can be saved and imported using proprietary software or with the Motion Software Development Kit (SDK). It is an open-source collection of classes in C++, C#, Java, and Python that provides real-time access to the sensor's output to

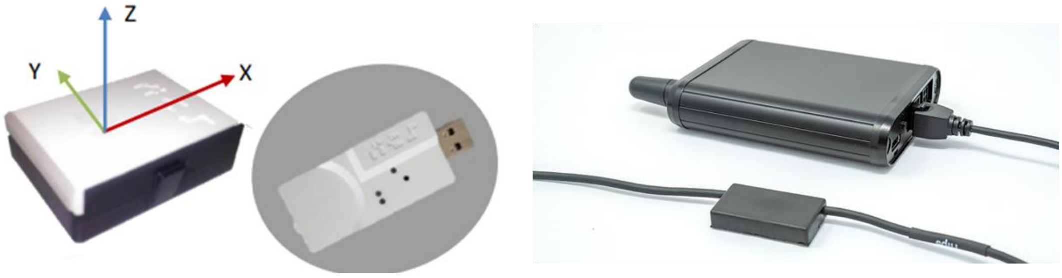

Figure 4 *ShomotionTM system (https://ncs-company.com) and Shadow Mocap Suit (https://www.motionshadow.com)*

simplify the development of third-party applications. The portable controller mounts the Motion Service that exports real-time data streams over TCP socket connections and sends the current output data to the client as soon as it becomes available. It is possible to choose the type of output depending on the application. For example, one could consider only raw sensor data, orientation estimates, or body position analysis captured with the biomechanical model and kinematic chains defined in the software. The SDK is a powerful tool because it allows the easy import of the IMU outputs inside other pipelines, such as a robot controller, as it will be done in this Thesis.

The main characteristics of the IMU of the two systems are listed in Table 1.

As well as for all wearable devices, one of the main drawbacks of these systems is soft tissue artifacts and corresponding movements of the sensors over the skin. Each IMUs has to be fixed as much straight as possible to the body. During the calibration, the orientation of the IMU over the segment is captured and then subtracted from the measured output during the experimentation phase. The relative motion between bones and sensors changes the orientation and leads to inaccuracies in rigid body poses and kinematics analysis.

It is then fundamental to fix the IMU as much as possible to the body without creating discomfort or interfering with natural human movements. However, the MEMS IMU sensors are rigid cases with a size of approximately 50 x 60 x 30 mm and a weight of 70 grams. Despite their size, it is not always comfortable and easy to fix them firmly to the body, ensuring no movements during the analysis. That is why a new promising research topic is the development of textile sensors that integrate the MEMS chips inside the fabric, thus reducing the size and discomfort to the human[34]–[36]. Textile sensors are a promising new version of traditional MEMS in wearable electronics, not only because they exploit the properties of flexible materials but also because they have the advantages of low cost, good conformality, comfort, and wearability. However, they present technological issues such as balancing good electrical conductivity and air permeability, poor durability, and improved integration of active materials and fabric.

Table 1 Commercial IMU characteristics (NOTE: Showmotion data refers to the system used in this study, but a full body set with 10 IMUs is also available)

Name	**Sensors range**			**Max Data rate**	**IMU's number**	**Connection**
	Accelerometer	**Gyroscope**	**Magnetometer**			
Shadow	±8 g	±4000 °/s	±800 µT	400 Hz	17	Cable
Showmotion	±8 g	±3000 °/s	±1600 µT	60 Hz	5	Wireless

1.3. Low-cost gyroscope and accelerometer calibration

A proper IMU calibration procedure estimates the causes of errors in outputs, thus reducing drifting in signal integration and increasing attitude estimate accuracy. The raw MEMS outputs consist of a tension proportional to the corresponding measured physical quantity: calibration is the process of determining those coefficients which relate the raw sensor outputs to known reference data over a wide range of values. Generally, gyroscope and accelerometer calibrations rely on mechanical platforms, which rotate the sensor about controlled axes at a known rotational velocity. This highly automated equipment guarantees high accuracy but is expensive. It is not economical to use costly equipment that expenses many times more than low-cost MEMS sensors, especially if the numerosity is low, like in the case of an end-user who wants to recalibrate his IMU system. This can be the typical scenario of an industrial application, where the calibration would be performed occasionally to improve the accuracy of the overall system, like for the applications presented in this Thesis. In the next section, a low-cost method based on the free-falling motion of a planar pendulum is described, which can be easily implemented in practice also in industry. The physical parameters of a theoretical motion model of the pendulum are identified and used to generate the reference signals of the calibration.

1.4 Sensor error model

The sensor error model has the scope to mathematically describe the error characteristic of the sensor, thus, finding those parameters that better describe the output and mitigate their negative effect. The simplest error model considers only a scale factor and a constant offset along the three axes. However, even if the manufacturing process is precise and highly automatized, the sensor sensitivity axes are usually not mutually orthogonal. This error component is called non-orthogonality misalignment, and it is become a common practice to include it in the sensor error model [37]–[40]. Some researchers consider also adding noise [41], [42] temperature effect [43] or propose nonlinear time-varying model [44]. Nonlinear time-varying models with many parameters offer better accuracies at the expense of complexity, which requires too costly iterative numerical solvers than the benefits brought to the solution. The effect of higher-order nonlinearities is often very mild, particularly when compared to the magnitude of the other noises. On the contrary, it is worth noting that the gyroscope's scale factor and bias change with temperature [45]. Yang and co. [43] calibrate the gyroscope along a range of -40 – 50 °C and prove that scale factors have a linear relationship with temperature, whereas the bias change with temperature with a no-mathematical describing law. Therefore, some companies have integrated a temperature sensor into the IMU sensor.

In our application, IMU sensors composing the MoCap systems are worn by workers who are supposed to work indoors or in industrial settings with a controlled temperature of around 20° C. Therefore, the temperature effect over the bias can be ignored, thus reducing the number of unknowns and the complexity of the sensor model. Similarly, since the purpose is to propose a low-cost and easily implementable calibration procedure for gyroscopes and accelerometers with a simple mathematical model, the non-linearities depending on the noise are not considered. The sensor error model depends on nine unknown parameters equal to scale factors, bias, and non-orthogonality misalignment for both the accelerometer and gyroscope. Supposing that the latter error is small, it is possible to project the measured quantities from non-orthogonal to orthogonal axes using an upper diagonal matrix ***T***, such as [38]:

$$\boldsymbol{T}^{-1} = \begin{bmatrix} 1 & -\theta_{yz} & \theta_{zy} \\ 0 & 1 & -\theta_{zx} \\ 0 & 0 & 1 \end{bmatrix} \tag{3}$$

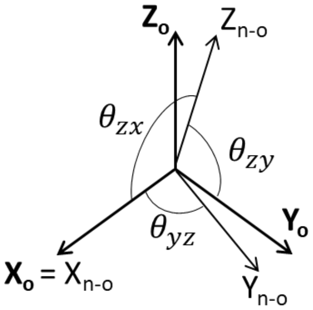

Figure 5 *Representation of non-orthogonality misalignment*

where the x axes of the non-orthogonal (X_{n-o}) and orthogonal system (X_o) are aligned, and the y axis of the non-orthogonal system lies (Y_{n-o}) in the x-y plane of the orthogonal system. Figure 5 represents the non-orthogonality misalignments. Here θ_{ij} is the rotation of the i-th non-orthogonal axis about the j-th orthogonal axis.

By adding the parameters for the bias and scale factors, the complete error model of the gyroscope and accelerometer is:

$$\mathbf{a}^s = (\boldsymbol{KT})^{-1}\mathbf{a}^0 + \mathbf{b} \tag{4}$$

where: $\mathbf{a}^s$ is the sensor's real output in the non-orthogonal system; $\mathbf{a}^0$ is the theoretical output in the orthogonal system; $\boldsymbol{K}$ is a diagonal matrix with the 3 scale factors k_x, k_y and k_z on the main diagonal; **b** is a column vector with 3 biases, b_x, b_y and b_z. The 9 unknowns are collected in the vector **x** for the calibration.

1.5 Pendulum Model

1.5.1 Methods

The proposed calibration procedure counts on the free fall motion of a physical pendulum. It consists of two separate steps: firstly, an identification of the pendulum parameters, and secondly, the correlation of the raw sensor output with the angular velocity and linear acceleration reference signals derived from the pendulum models. The pendulum is made by a cylindrical mass hanging from a metallic threaded rod and fixed at a pivot point by a revolute joint. Through a 3D printed structure, the sensor is attached to the distal extremity of the pendulum, in a structure that is easily disassemble for quickly changing the sensor orientation during the experiment. The moment of inertia, *I*, about the revolute joint axis and

Table 2 *Pendulum parameters*

Parameters	Value
Cylinder mass	0.358 Kg
Cylinder diameter	50 mm
Cylinder high	25 mm
Pivot diameter	10 mm
Threaded rod mass	0.102 Kg
Threaded rod diameter	8 mm
Threaded rod length	286 mm
IMU case mass	0.05 Kg
IMU case dimension	41 x 34 x 20 mm

the centre of mass position along the cylinder axis, z_g, are calculated from the pendulum parameters listed in Table 2. The total mass, denoted as m_t, is the sum of all the pendulum masses.

The physical parameters of the theoretical motion model of the pendulum are identified by fitting the angular motion of a real pendulum measured by an incremental encoder over the revolute joint (Trinamic TMCS-28). With respect to similar methods [46], the pendulum motion model includes both the kinetic (ρ) and viscous (η) friction terms.

A widely used model for kinetic friction is the dry friction or Coulomb friction. The model is valid for dry surfaces, or those surfaces covered by a thin lubricant film that does not prevent contact. The kinetic term depends on the material properties and the characteristics of the surfaces of the contacting bodies, the amount and type of fluid between the contacting points, and temperature. Friction force opposes the motion and the resistive moment due to this term (M_{fk}) is equal to:

$$M_{fk} = -\rho\, r \|\boldsymbol{f_n}\| \operatorname{sign}(\omega) \tag{5}$$

where $\|\boldsymbol{f_n}\|$ is the magnitude of the normal reaction force at the revolute joint, with radius r (5 mm). The reaction forces depend on the weight forces $\mathbf{f}_{\boldsymbol{w}}$ and the inertial forces $\mathbf{f}_{\boldsymbol{I}}$ (see Figure 6). For the second-Newton law, the resistive force is equal to:

$$\|\boldsymbol{f_n}\|^2 = (m_t z_g(\omega^2 \mathrm{s}(\theta) + \dot{\omega}\mathrm{c}(\theta)))^2 + (m_t(\dot{\omega} z_g \mathrm{s}(\theta) - g - \omega^2 z_g \mathrm{c}(\theta)))^2 \tag{6}$$

where c(θ) and s(θ) stands for cos(θ) and sin(θ) respectively; ω is the pendulum angular velocity; $\dot{\omega}$ is the angular acceleration and g is the gravity acceleration. The analysis of the amplitude of all components in Eq. 6 shows that the terms including $\dot{\omega}$ are negligible with respect to the other terms and can be ignored. Thus, the M_{fk} can be simplified as:

$$M_{fk} = -\rho\, r\sqrt{(m_t g)^2 + \left(m_t z_g \omega^2\right)^2 + \left(2 m_t^2 g z_g \omega^2 \mathrm{c}(\theta)\right)^2}\ \ \tanh\left(\frac{\omega}{\omega_0}\right) \tag{7}$$

where ρ is the friction coefficient, which for metal and plastic materials is between 0.1 and 0.3. The function $\tanh(\cdot)$ approximates the sign function with a continuous function, to allow a robust integration of the pendulum dynamic model. The value ω_0 is a tuning parameter used both to make the tanh argument dimensionless and to tune the differences between the tanh and sign functions. Here we assumed $1/\omega_0$=10 s/rad since it showed to be the optimal compromise between approximation and computational stability in preliminary tests.

For the moment equilibrium about the centre of the revolute joint, the motion equation of the pendulum is:

$$I\dot{\omega} + \eta\omega + m_t g z_g \mathrm{s}(\theta) + M_{fk} = 0 \tag{8}$$

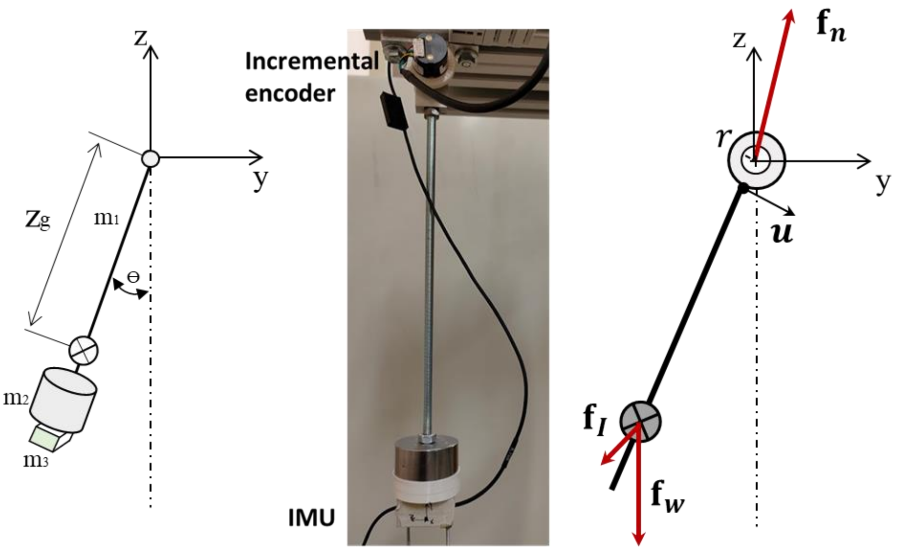

Figure 6 *left) pendulum parameters scheme - middle) real pendulum – right) force representation*

The test consists of recording the angle data with the encoder while the pendulum performs a dynamic planar free-fall motion starting from a known static initial angle. Here, the free fall motion starts from an angle of $\pi/2$, but could be an arbitrary value that produces a pendulum motion with a wide range of angular velocity and acceleration values.

The parameters ρ, η and z_g are estimated using the Matlab function *nlgreyest* (Matlab R2020a). It estimates the parameters of a nonlinear grey-box model, by considering the system's initial state and by fitting Eq. 8 solution to the encoder data. The other model parameters are not optimized.

The identification of the pendulum model is performed using six different encoder datasets. To quantify the advantages of using this complete pendulum model, it is compared to the traditional pendulum model that considers only a friction term dependent on ω:

$$I\dot{\omega} + \eta\omega + m_t g z_g \mathrm{s}(\theta) = 0 \tag{9}$$

The mean squared error (MSE) between the reconstructed and the measured angles are evaluated in both cases and compared.

1.5.2 Results

The Matlab function estimates the parameters from 200 data sample of the encoders, which measures with a frequency of 100 Hz. In order to test the validity of the results, six different tests are performed. Both the mean values and the standard deviation among the test are reported in Table 3. Results shows a low variability and are congruent with standard values of kinetic and viscous friction.

Table 3 *Pendulum parameter results*

Parameters	Value
ρ	0.13 ± 0.03
η [Nms]	(23.8 ± 5) 10-6
zg [mm]	234 ± 3

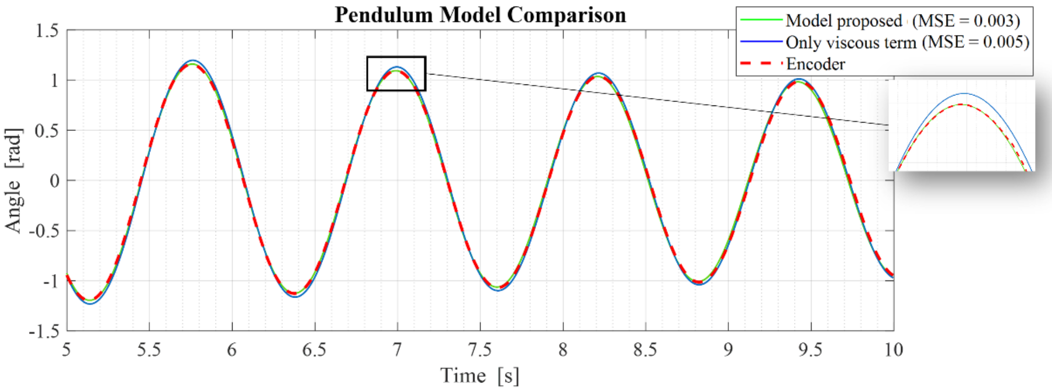

Figure 7 *Comparison between the pendulum's angle measured by the encoder and the one obtained by the dynamic model with and without kinetic friction over 5 seconds*

The dynamic pendulum model described in this study shows better results than a traditional pendulum model, which considers only one friction term dependent on ω. As shown in Figure 7, the mean squared error (MSE) of the response of our model compared to the encoder measurement data has a lower value than the model with only the viscous term. The model proposed has a MSE equal to 0.003, compared to 0.005 for the model containing only the friction term. As expected, the major discrepancies are visible at low velocity where the contribution of non-modelled friction terms are more effective.

1.6 Calibration method

Several algorithms have been used for identifying the sensor error model unknown parameters from experimental data, from Kalman filtering techniques [41], [44], [47], [48], especially for real-time applications. However optimization algorithms are a widespread and suitable method for sensor calibration [39]. Both Newton method [37], [38], or non-linear least square algorithms [42] are proposed: the cost function minimizes the difference between the pendulum model results and the experimental sensor output. Since it can reach several local optima, the definition of the initial starting values has to be determined carefully. Moreover, it is fundamental to provide more data points than the number of parameters to determine, such as to avoid unconsidered conditions in the reachable sensor range.

Similarly, our approach is based on the Matlab function lsqcurvefit, which solves nonlinear curve-fitting problems in the least-square sense. The Trust-

Region-Reflective Least Squares have been used in [49], [50]. The unknown calibration parameters of the accelerometer and gyroscope, collected in the **x** vector, are defined by minimizing the error function describing the deviation of the sensor output from the magnitude of the corresponding measure estimated by the pendulum model. Defined **h** as the function which, for any sensor output, relates $\mathbf{a}^s$ with $\mathbf{a}^0$, from Eq. 4 results:

$$\mathbf{a}^0 = \mathbf{h}(\mathbf{a}^s, \mathbf{x}) = \boldsymbol{KT}(\mathbf{a}^s - \mathbf{b}) \tag{10}$$

Since each axis has to be considered, the measure is performed by placing the IMU at three different positions *i* =1,2,3, to align the three corresponding x, y and z gyroscope's sensitive axes along the pendulum rotation axis. Thus, the optimization problem becomes:

$$\min_{\mathbf{x}} \left\{ \sum_{i=1}^{3} \sum_{j=1}^{N} \left\| \mathbf{h}\left(\mathbf{a}_j^s, \mathbf{x}\right)_i - \mathbf{p}(\theta_j, \omega_j, \dot{\omega}_j)_i \right\|^2 \right\} \tag{11}$$

where **p** denotes the reference signal derived by the pendulum model; j = 1,…,N with *N* equal to the number of measures.

To obtain the first guess for the optimization, we perform a standard 6-positions calibration, firstly described in [51]. It consists of placing the sensor on a plane perpendicular to the gravity in up ($a_{i,up}^s$) and down ($a_{i,down}^s$) positions for each sensitive axis and performing a static measure. The raw static signals from the accelerometer and gyroscope are averaged throughout 1 s to reduce noise.

Since the accelerometer always measures gravity, bias (b_i) and scale factors (k_i) for each axis can be estimated using the average sensor raw output over the entire static measure [38]:

$$k_i = \frac{a_{i,up}^s - a_{i,down}^s}{2g} \tag{12}$$

$$b_i = \frac{a_{i,up}^s + a_{i,down}^s}{2} \tag{13}$$

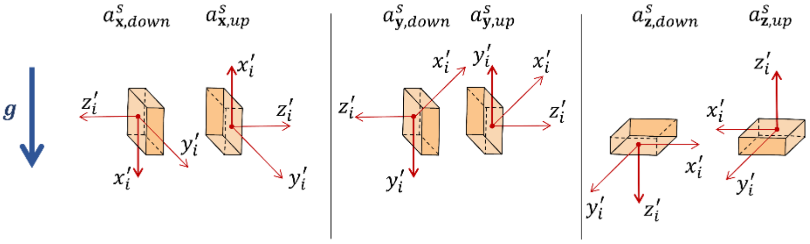

Figure 8 Static 6-poses calibration

Differently, for the gyroscope, the bias is estimated as in Eq. 13, and the scale factors are chosen equal to the ratio between the maximum value of ω from the model and the *i*-th gyroscope axis during dynamic tests. For both sensors, the first guess for all misalignment angles is zero.

After the static calibration, the sensor is positioned at the pendulum extremity in 3 different positions to align each gyroscope axis with the angular velocity vector. A 3d printed structure holds the case within the IMU case, whose reposition is performed manually with no sophisticated instruments. This fact could implicate a misalignment of the sensor axis about the pendulum frame that could reduce the calibration procedure accuracy.

Thus, an additional orientation error is considered and evaluated during this phase. The latter can be due to 1) a rotation of the sensor within the IMU case and 2) a misalignment of the case respecting the pendulum axis. The so-called matrix $\boldsymbol{R}_t^s$ accounts for both errors, which involve two different possible scenarios. If the first error is present, the error sensor model should contain an additional misalignment matrix that describes the angle between the three-sensor axis and the external cover case. This parameter identification is possible only with a rigorous orientation of the IMU case about the pendulum, thus, ignoring the influence of error 2. On the contrary, if error 1 is negligible, the positioning of the

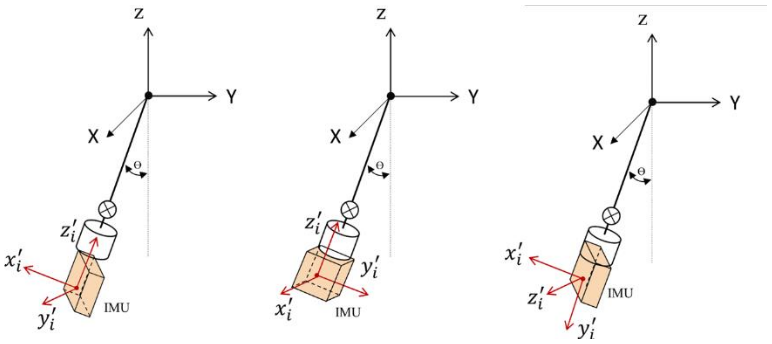

Figure 9 Three poses of the dynamic calibration

IMU case could be less accurate, thus simplifying the calibration procedure. In this context, we consider the second scenario and identify the positioning misalignment error through an optimization problem. By choosing an XYZ Euler angle parametrization of ξ, β and γ angles, the matrix R_t^s can be written as:

$$\boldsymbol{R}_{\boldsymbol{t}}^{\boldsymbol{s}} = \begin{bmatrix} 1 & 0 & 0 \\ 0 & \mathrm{c}(\xi) & -\mathrm{s}(\xi) \\ 0 & \mathrm{s}(\xi) & \mathrm{c}(\xi) \end{bmatrix} \begin{bmatrix} \mathrm{c}(\beta) & 0 & \mathrm{s}(\beta) \\ 0 & 1 & 0 \\ -\mathrm{s}(\beta) & 0 & \mathrm{c}(\beta) \end{bmatrix} \begin{bmatrix} \mathrm{c}(\gamma) & -\mathrm{s}(\gamma) & 0 \\ \mathrm{s}(\gamma) & \mathrm{c}(\gamma) & 0 \\ 0 & 0 & 1 \end{bmatrix} \tag{14}$$

While $\boldsymbol{R}_{\boldsymbol{t}}^{\boldsymbol{s}}$ describe the positioning error, the experimental orientation of the sensor with respect to the pendulum model is the rotation matrix $\boldsymbol{R}_{\boldsymbol{p}}^{\boldsymbol{t}}$ defines the theoretical orientation of the IMU-sensitive axes with respect to the pendulum motion plane (YZ-plane) in the 3 different experimental alignments.

Both the matrices correct the sensor raw output, namely the angular velocity $\boldsymbol{\omega}^*$ for the gyroscope and the linear acceleration $\boldsymbol{\alpha}^*$ for the accelerometer. Then, the reference gyroscope signal $\mathbf{p}_g$ and the reference accelerometer signal $\mathbf{p}_a$ are given by

$$\mathbf{p}_g(\theta_j, \omega_j)_i = \boldsymbol{\omega}_{i,j}^* = \boldsymbol{R}_{\boldsymbol{t},i}^{\boldsymbol{s}} \, \boldsymbol{R}_{\boldsymbol{p},i}^{\boldsymbol{t}} \begin{bmatrix} \omega_j \\ 0 \\ 0 \end{bmatrix} \tag{15}$$

and

$$\mathbf{p}_a(\theta_j, \omega_j, \dot{\omega}_j)_i = \boldsymbol{\alpha}_{i,j}^* = \boldsymbol{R}_{\boldsymbol{t},i}^{\boldsymbol{s}} \, \boldsymbol{R}_{\boldsymbol{p},i}^{\boldsymbol{t}} \left(\begin{bmatrix} 1 & 0 & 0 \\ 0 & \mathrm{c}(\theta_j) & \mathrm{s}(\theta_j) \\ 0 & -\mathrm{s}(\theta_j) & \mathrm{c}(\theta_j) \end{bmatrix} \begin{bmatrix} 0 \\ 0 \\ -g \end{bmatrix} + \begin{bmatrix} 0 \\ -L\dot{\omega}_j \\ -L\omega_j^2 \end{bmatrix} \right) \tag{16}$$

where L represent the IMU position along the cylinder axis. The three error angles ξ, β and γ are found before sensor calibration, by minimizing Eq. 11-12 over the error angles.

A sensitivity analysis quantifies to which extent the calibration procedure is robust. It compares the calibration parameters over several experiments with controlled changes in mounting angles. The calibration procedure is robust when the sensor parameters are the same with different external assembling conditions, such as high position misalignment errors.

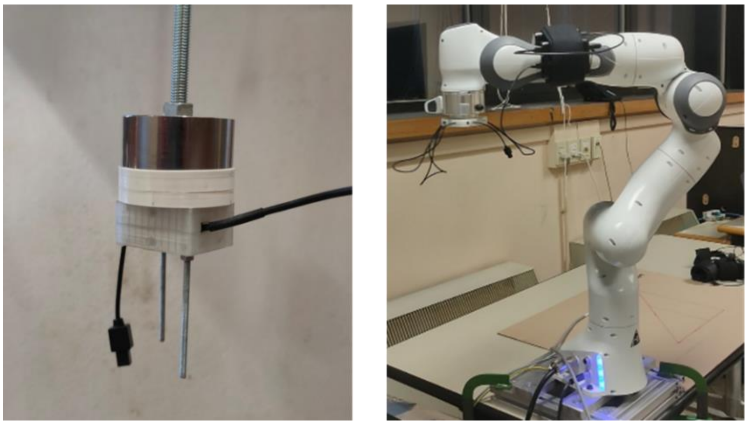

Figure 10 *left) Picture of the IMU misalignment over the pendulum for the sensitivity analysis right) set-up for the test with the robot*

An additional test is performed using the Franka Emika Panda robot (FRANKA EMIKA GmbH, DE) to test the goodness of the calibration results. A 3D-printed connection interface fixes the sensor to the end-effector, which rotates about its axis with an angular velocity of 0.2 rad/s. The angular velocity obtained with the sensor error model terms resulting from the calibration optimization process is compared with the robot one and the gyroscope output made with the calibration performed by the company.

1.7 Results

Both the accelerometer and gyroscope are calibrated starting from the 16-bit signed integer raw sensor data, using the angular velocity and linear acceleration reconstructed by the pendulum parameters model. The sensor error parameters obtained with different calibration tests, performed with a controlled IMU mounting positioning are listed in Table 3. These values correspond to the mean of each sensor error model parameters over the 3 results and their corresponding standard deviation (SD). The sensitivity analysis showed that the proposed calibration algorithm is robust since calibration parameters are almost insensitive up to orientation errors of about 10°. The SD is low (<2%) and demonstrates that the algorithm for correcting the mounting misalignments doesn’t influence the goodness of calibration. The only exception is the value of the Y-axis bias of the accelerometer that shows a higher SD (>20%). This could be due to some non-modelled additional noise over that specific sensor axis, which thus require some reasonable attention in mounting the IMU on the pendulum.

__Table 4__ Calibration results of gyroscope and accelerometers

Parameters	Value	Parameters	Value
kx	487 ± 4	kx	470 ± 4
ky	483 ± 1	ky	431 ± 5
kz	465 ± 4	kz	433 ± 0.3
bx [°/s]	14 ± 0.06	bx [m/s2]	211 ± 4
by[°/s]	1 ± 0.5	by[m/s2]	299 ± 67
bz [°/s]	-6 ± 0.17	bz [m/s2]	15 ± 2
θyz [rad]	(-7 ± 1) 10-5	θyz [rad]	(3 ± 0.15) 10-2
θzy [rad]	(4 ± 0.8) 10-4	θzy [rad]	(-5 ± 0.05) 10-2
θzx [rad]	(8 ± 2) 10-4	θzx [rad]	(1 ± 0.4) 10-2

Since all the other values have a small variability over the test, we can consider the proposed low-cost calibration methods a good compromise between costs and performance, especially for companies or institutions where the numerosity of IMU to calibrate is low. Moreover, is a simple method to test the goodness, stability and range of the sensors. This method requires acceptable attention during assembly, and the setup is easy to build and implement without using sophisticated and expensive instrumentation.

Figure 11 shows that the custom-calibrated gyroscope signal reproduces accurately the angular velocity of the end-effector, removing some inaccuracies in the gyroscope output obtained using only the company calibration.

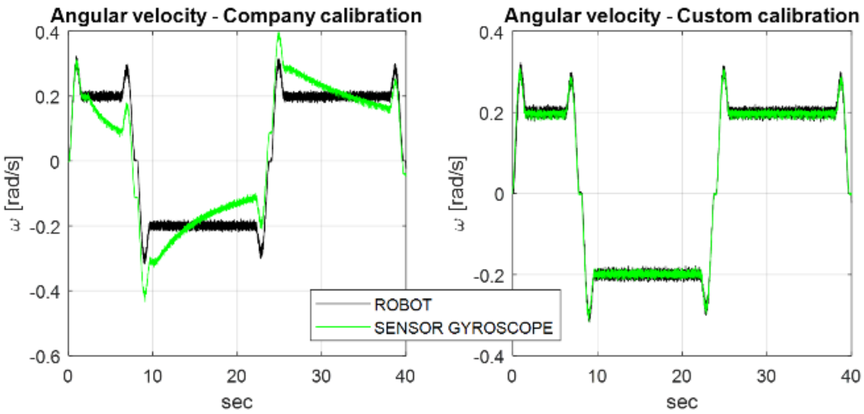

***Figure 11** Comparison between the angular velocity imposed by the robot and the corresponding measures obtained using the same sensor, with the company (left) and proposed (right) calibration.*

The sensor error model used in this work better describes the gyroscope output for low dynamics than the one used by the company. In addition, this procedure is suitable for implementing more sophisticated sensor error models, which consider other parameters such as noise distribution. For the bias instability term implementation, it is however necessary to perform the calibration in a oven with controlled temperature at the expense of the system cost.

The major drawback of this approach is that the sensor's acquisition frequency has to be high enough to map and detect the free-fall pendulum motion. The pendulum estimation of the friction terms increases the accuracy in defining the reference signals during the first 20 seconds of free falling. However, the movement reconstruction could be less accurate in the last period when the angular velocity is low. The calibration is rigorous in the first phase of pendulum free-falling motion, but a low sensor data rate could not map sufficient data points to assess a complete and high variable dataset for calibration. A possible solution, where reasonable, is to increment the length L of the pendulum thus diminishing the natural pendulum motion and its frequency.

In conclusion, the proposed calibration method is low-cost and easy to implement and represents a valid alternative to the expensive and complex instrumentation used for gyroscope and accelerometer calibration.

References

[1] M. Menolotto, D.-S. Komaris, S. Tedesco, B. O'Flynn, e M. Walsh, «Motion Capture Technology in Industrial Applications: A Systematic Review», *Sensors*, vol. 20, fasc. 19, p. 5687, ott. 2020, doi: 10.3390/s20195687.

[2] S. O. H. Madgwick, A. J. L. Harrison, e R. Vaidyanathan, «Estimation of IMU and MARG orientation using a gradient descent algorithm», in *2011 IEEE International Conference on Rehabilitation Robotics*, Zurich, giu. 2011, pp. 1–7. doi: 10.1109/ICORR.2011.5975346.

[3] R. Mahony, T. Hamel, e J.-M. Pflimlin, «Nonlinear Complementary Filters on the Special Orthogonal Group», *IEEE Trans. Autom. Control*, vol. 53, fasc. 5, pp. 1203–1218, giu. 2008, doi: 10.1109/TAC.2008.923738.

[4] A. M. Sabatini, «Quaternion-Based Extended Kalman Filter for Determining Orientation by Inertial and Magnetic Sensing», *IEEE Trans. Biomed. Eng.*, vol. 53, fasc. 7, pp. 1346–1356, lug. 2006, doi: 10.1109/TBME.2006.875664.

[5] A. Filippeschi, N. Schmitz, M. Miezal, G. Bleser, E. Ruffaldi, e D. Stricker, «Survey of Motion Tracking Methods Based on Inertial Sensors: A Focus on Upper Limb Human Motion», *Sensors*, vol. 17, fasc. 6, p. 1257, giu. 2017, doi: 10.3390/s17061257.

[6] K. Lebel, P. Boissy, M. Hamel, e C. Duval, «Inertial Measures of Motion for Clinical Biomechanics: Comparative Assessment of Accuracy under Controlled Conditions – Changes in Accuracy over Time», *PLOS ONE*, vol. 10, fasc. 3, p. e0118361, mar. 2015, doi: 10.1371/journal.pone.0118361.

[7] L. Ricci, F. Taffoni, e D. Formica, «On the Orientation Error of IMU: Investigating Static and Dynamic Accuracy Targeting Human Motion», *PLOS ONE*, p. 15, 2016.

[8] E. Bergamini, G. Ligorio, A. Summa, G. Vannozzi, A. Cappozzo, e A. Sabatini, «Estimating Orientation Using Magnetic and Inertial Sensors and Different Sensor Fusion Approaches: Accuracy Assessment in Manual and Locomotion Tasks», *Sensors*, vol. 14, fasc. 10, pp. 18625–18649, ott. 2014, doi: 10.3390/s141018625.

[9] M. A. Brodie, A. Walmsley, e W. Page, «Dynamic accuracy of inertial measurement units during simple pendulum motion: Technical Note», *Comput. Methods Biomech. Biomed. Engin.*, vol. 11, fasc. 3, pp. 235–242, giu. 2008, doi: 10.1080/10255840802125526.

[10] A. G. Cutti, A. Giovanardi, L. Rocchi, e A. Davalli, «A simple test to assess the static and dynamic accuracy of an inertial sensors system for human movement analysis», in *2006 International Conference of the IEEE Engineering in Medicine and Biology Society*, New York, NY, ago. 2006, pp. 5912–5915. doi: 10.1109/IEMBS.2006.260705.

[11] M. Caruso *et al.*, «Analysis of the Accuracy of Ten Algorithms for Orientation Estimation Using Inertial and Magnetic Sensing under Optimal Conditions: One Size Does Not Fit All», *Sensors*, vol. 21, fasc. 7, p. 2543, apr. 2021, doi: 10.3390/s21072543.

[12] V. M. N. Passaro, A. Cuccovillo, L. Vaiani, M. De Carlo, e C. E. Campanella, «Gyroscope Technology and Applications: A Review in the Industrial Perspective», *Sensors*, vol. 17, fasc. 10, p. 2284, ott. 2017, doi: 10.3390/s17102284.

[13] O. J. Woodman, «An introduction to inertial navigation», p. 37.

[14] D. H. Titterton e J. L. Weston, *Strapdown inertial navigation technology*, 2. ed. Stevenage: The Inst. of Engineering and Technology, 2009.

[15] W. Niu *et al.*, «Summary of Research Status and Application of MEMS Accelerometers», *J. Comput. Commun.*, vol. 06, fasc. 12, pp. 215–221, 2018, doi: 10.4236/jcc.2018.612021.

[16] H. H. Yang *et al.*, «Ferromagnetic micromechanical magnetometer», *Sens. Actuators Phys.*, vol. 97–98, pp. 88–97, apr. 2002, doi: 10.1016/S0924-4247(01)00809-3.

[17] D. Ren, L. Wu, M. Yan, M. Cui, Z. You, e M. Hu, «Design and Analyses of a MEMS Based Resonant Magnetometer», *Sensors*, vol. 9, fasc. 9, pp. 6951–6966, set. 2009, doi: 10.3390/s90906951.

[18] F. L. Markley e J. L. Crassidis, *Fundamentals of Spacecraft Attitude Determination and Control*. New York, NY: Springer New York, 2014. doi: 10.1007/978-1-4939-0802-8.

[19] J. F. Vasconcelos, G. Elkaim, C. Silvestre, P. Oliveira, e B. Cardeira, «Geometric Approach to Strapdown Magnetometer Calibration in Sensor Frame», *IEEE Trans. Aerosp. Electron. Syst.*, vol. 47, fasc. 2, pp. 1293–1306, apr. 2011, doi: 10.1109/TAES.2011.5751259.

[20] M. Kok e T. B. Schon, «Magnetometer Calibration Using Inertial Sensors», *IEEE Sens. J.*, vol. 16, fasc. 14, pp. 5679–5689, lug. 2016, doi: 10.1109/JSEN.2016.2569160.

[21] V. Renaudin, M. H. Afzal, e G. Lachapelle, «Complete Triaxis Magnetometer Calibration in the Magnetic Domain», *J. Sens.*, vol. 2010, pp. 1–10, 2010, doi: 10.1155/2010/967245.

[22] H. Parwana e M. Kothari, «Quaternions and Attitude Representation». arXiv, 29 agosto 2017. Consultato: 4 ottobre 2022. [Online]. Disponibile su: http://arxiv.org/abs/1708.08680

[23] Y. Tian, H. Wei, e J. Tan, «An Adaptive-Gain Complementary Filter for Real-Time Human Motion Tracking With MARG Sensors in Free-Living Environments», *IEEE Trans. Neural Syst. Rehabil. Eng.*, vol. 21, fasc. 2, pp. 254–264, mar. 2013, doi: 10.1109/TNSRE.2012.2205706.

[24] A. D. Young, «Use of Body Model Constraints to Improve Accuracy of Inertial Motion Capture», p. 7.

[25] H. D. Black, «A passive system for determining the attitude of a satellite», p. 2.

[26] M. D. Shuster e S. D. Oh, «Three-axis attitude determination from vector observations», p. 8, 1981.

[27] X. Yun, E. R. Bachmann, e R. B. McGhee, «A Simplified Quaternion-Based Algorithm for Orientation Estimation From Earth Gravity and Magnetic Field Measurements», *IEEE Trans. Instrum. Meas.*, vol. 57, fasc. 3, p. 13, 2008.

[28] D. Roetenberg, H. Luinge, e P. Slycke, «Xsens MVN: Full 6DOF Human Motion Tracking Using Miniature Inertial Sensors», p. 10, 2013.

[29] R. Zhu e Z. Zhou, «A Real-Time Articulated Human Motion Tracking Using Tri-Axis Inertial/Magnetic Sensors Package», *IEEE Trans. Neural Syst. Rehabil. Eng.*, vol. 12, fasc. 2, pp. 295–302, giu. 2004, doi: 10.1109/TNSRE.2004.827825.

[30] X. Yun e E. R. Bachmann, «Design, Implementation, and Experimental Results of a Quaternion-Based Kalman Filter for Human Body Motion Tracking», *IEEE Trans. Robot.*, vol. 22, fasc. 6, pp. 1216–1227, dic. 2006, doi: 10.1109/TRO.2006.886270.

[31] P. Zhang, J. Gu, E. E. Milios, e P. Huynh, «Navigation with IMU/GPS/digital compass with unscented Kalman filter», in *IEEE International Conference Mechatronics and Automation, 2005*, Niagara Falls, Ont., Canada, 2005, vol. 3, pp. 1497–1502. doi: 10.1109/ICMA.2005.1626777.

[32] H. Deilamsalehy e T. C. Havens, «Sensor fused three-dimensional localization using IMU, camera and LiDAR», in *2016 IEEE SENSORS*, Orlando, FL, USA, ott. 2016, pp. 1–3. doi: 10.1109/ICSENS.2016.7808523.

[33] M. A. Ruiz Ibán *et al.*, «Evaluation of a novel portable three-dimensional scapular kinematics assessment system with inter and intraobserver reproducibility and normative data for healthy adults», *J. Exp. Orthop.*, vol. 7, fasc. 1, p. 31, dic. 2020, doi: 10.1186/s40634-020-00238-6.

[34] M. Li *et al.*, «Integration and Testing of a Three-Axis Accelerometer in a Woven E-Textile Sleeve for Wearable Movement Monitoring», *Sensors*, vol. 20, fasc. 18, p. 5033, set. 2020, doi: 10.3390/s20185033.

[35] C. Mattmann, O. Amft, H. Harms, G. Troster, e F. Clemens, «Recognizing Upper Body Postures using Textile Strain Sensors», in *2007 11th IEEE International Symposium on Wearable Computers*, Boston, MA, USA, ott. 2007, pp. 1–8. doi: 10.1109/ISWC.2007.4373773.

[36] A. Tognetti, F. Lorussi, N. Carbonaro, e D. de Rossi, «Wearable Goniometer and Accelerometer Sensory Fusion for Knee Joint Angle Measurement in Daily Life», *Sensors*, vol. 15, fasc. 11, pp. 28435–28455, nov. 2015, doi: 10.3390/s151128435.

[37] I. Skog e P. Handel, «CALIBRATION OF A MEMS INERTIAL MEASUREMENT UNIT», p. 6.

[38] U. Qureshi e F. Golnaraghi, «An Algorithm for the In-Field Calibration of a MEMS IMU», *IEEE Sens. J.*, vol. 17, fasc. 22, pp. 7479–7486, nov. 2017, doi: 10.1109/JSEN.2017.2751572.

[39] M. Sipos, P. Paces, J. Rohac, e P. Novacek, «Analyses of Triaxial Accelerometer Calibration Algorithms», *IEEE Sens. J.*, vol. 12, fasc. 5, pp. 1157–1165, mag. 2012, doi: 10.1109/JSEN.2011.2167319.

[40] W. T. Fong, S. K. Ong, e A. Y. C. Nee, «Methods for in-field user calibration of an inertial measurement unit without external equipment», *Meas. Sci. Technol.*, vol. 19, fasc. 8, p. 085202, ago. 2008, doi: 10.1088/0957-0233/19/8/085202.

[41] T. Beravs, J. Podobnik, e M. Munih, «Three-Axial Accelerometer Calibration Using Kalman Filter Covariance Matrix for Online Estimation of Optimal Sensor Orientation», *IEEE Trans. Instrum. Meas.*, vol. 61, fasc. 9, pp. 2501–2511, set. 2012, doi: 10.1109/TIM.2012.2187360.

[42] Z. F. Syed, P. Aggarwal, C. Goodall, X. Niu, e N. El-Sheimy, «A new multi-position calibration method for MEMS inertial navigation systems», *Meas. Sci. Technol.*, vol. 18, fasc. 7, pp. 1897–1907, lug. 2007, doi: 10.1088/0957-0233/18/7/016.

[43] H. Yang, B. Zhou, L. Wang, H. Xing, e R. Zhang, «A Novel Tri-Axial MEMS Gyroscope Calibration Method over a Full Temperature Range», *Sensors*, vol. 18, fasc. 9, p. 3004, set. 2018, doi: 10.3390/s18093004.

[44] P. Batista, C. Silvestre, P. Oliveira, e B. Cardeira, «Accelerometer Calibration and Dynamic Bias and Gravity Estimation: Analysis, Design, and Experimental Evaluation», *IEEE Trans. Control Syst. Technol.*, vol. 19, fasc. 5, pp. 1128–1137, set. 2011, doi: 10.1109/TCST.2010.2076321.

[45] M. El-Diasty, A. El-Rabbany, e S. Pagiatakis, «Temperature variation effects on stochastic characteristics for low-cost MEMS-based inertial sensor error», *Meas. Sci. Technol.*, vol. 18, fasc. 11, pp. 3321–3328, nov. 2007, doi: 10.1088/0957-0233/18/11/009.

[46] K.-Y. Choi, S.-A. Jang, e Y.-H. Kim, «Calibration of Inertial Measurement Units Using Pendulum Motion», *Int. J. Aeronaut. Space Sci.*, vol. 11, fasc. 3, pp. 234–239, set. 2010, doi: 10.5139/IJASS.2010.11.3.234.

[47] M. Stakkeland, G. Prytz, W. E. Booij, e S. T. Pedersen, «Characterization of Accelerometers Using Nonlinear Kalman Filters and Position Feedback», *IEEE Trans. Instrum. Meas.*, vol. 56, fasc. 6, pp. 2698–2704, dic. 2007, doi: 10.1109/TIM.2007.908145.

[48] M. S. Grewal, V. D. Henderson, e R. S. Miyasako, «Application of Kalman filtering to the calibration and alignment of inertial navigation systems», *IEEE Trans. Autom. Control*, vol. 36, fasc. 1, pp. 3–13, gen. 1991, doi: 10.1109/9.62283.

[49] H. Byrd, B. Schnabel, e G. A. Shultz, «Approximate solution of the trust region problem by minimization over two-dimensional subspaces», p. 17.

[50] M. A. Branch, T. F. Coleman, e Y. Li, «A Subspace, Interior, and Conjugate Gradient Method for Large-Scale Bound-Constrained Minimization Problems», *SIAM J. Sci. Comput.*, vol. 21, fasc. 1, pp. 1–23, gen. 1999, doi: 10.1137/S1064827595289108.

[51] F. Ferraris, I. Gorini, U. Grimaldi, e M. Parvis, «Calibration of three-axial rate gyros without angular velocity standards», *Sens. Actuators Phys.*, vol. 42, fasc. 1–3, pp. 446–449, apr. 1994, doi: 10.1016/0924-4247(94)80031-6.

Chapter 2

Motion Tracking System

A good estimation of the IMU sensor attitude is insufficient for obtaining an accurate motion-tracking analysis for two main reasons: inaccuracies in the biomechanical model definition and errors in the identification of the IMU position on the body segments. Moreover, the effects of these errors increment with the number of bodies considered and the type of analysis performed. A standard position analysis, i.e. the determination of the joint angles of the subject, useful for ergonomics or rehabilitation purposes, is affected by errors on the IMUs outputs, by noise on attitude estimation, and by inaccuracies on the choice of the anthropometric model. Indeed, since IMUs generally output only their attitude, the pose of each segment of the body is generally obtained by driving a multibody model of the subject with the IMUs data, but it is necessary to attribute correct lengths to segments and proper joint connections. In addition, the errors increase if the absolute position of a moving subject is needed. The latter can be estimated only with additional sensors, such as pressure insoles, cameras, or proximity sensors, that reduce the overall drifting errors in position estimation. Precisely, during simple gait, the absolute position is estimated by adding the exact location of the contact points of the foot during different steps. Thus, even little errors in the segments' length definition or in the angles cause a rapid propagation of errors only after several steps. In our application, when we talk about body position, we mean the localization of the segments in space but not the body's absolute position in a specific area, since the main interest is on the biomechanics activity in the workplace, or independently from the position in the working area.

The human body is schematized as a group of kinematics chains connected to the trunk. The position of the distal body segments stands on the location of the previous bodies composing the kinematic chain. It depends on the orientation and the lengths of all the preceding bodies. The chance of having higher errors increases with the number of bodies considered.

Each joint angle is estimated using two consecutive IMUs, one in the distal and one in the proximal segments. The joint angle would be the relative orientation of one sensor with respect to the other, expressed in the coordinate system used by the sensor fusion algorithm. Considering the impossibility to impose a precise location of each IMU on the body and considering also the relative IMU-bone motion due to soft-tissue artifact, this definition does not have a physiological and anatomical meaning, and cannot be used as a standard approach for clinical practice. Thus, it is necessary to express the joint rotation in an anatomical sense by performing a calibration that assesses the pose of IMUs on each body. This calibration is called sensor-to-segment calibration. For the workers’ safety in industrial applications, which is the object of this Thesis, it is particularly important that also this calibration is performed accurately.

This chapter present a sensor-to-segment calibration procedure. More in general, the whole framework which reconstructs the entire body motion using 17 IMUs is presented, starting from the choice of the biomechanical models and the type of calibration performed. For those applications which require a real-time evaluation of biomechanical data, the anthropometric model is chosen among those proposed in the literature, and then specialised for the specific application. For instance, for the ergonomics and collaborative robotics applications considered in this Thesis, since we need to define an algorithm able to compute the body pose in real-time (100 Hz) for human safety, we propose a sensor-to-segment calibration using only the sensor's attitude data and not the signal from the gyroscope and accelerometer. This fact reduces the number of packets to stream to the robot controller. The validity of the proposed procedure is tested and compared with the motion analysis performed by an optoelectronic system, and the last section of this chapter lists the results obtained.

2.1 Anthropometric model

The definition of the kinematic biomechanical model is essential for capturing human body motion, especially with inertial sensors. The model can differ primarily by the type of mechanical joints and by the specific length of each body. In general, the simplest biomechanical model consists of rigid bodies connected by spherical joints. Five kinematic chains model the entire human body:

1. From pelvi to head
2. From thorax to right or left arm
3. From pelvis to right or left foot

Each body is expressed in its own body coordinates system (BCS), generally defined as a right-handed Cartesian coordinate system. The International Society of Biomechanics proposed a standard definition for body and joint coordinate systems of lower [1] and upper [2] limbs. According to this standardization, the body axes are defined through specific bone landmarks that are either palpable or identifiable from X-rays. Body motion is expressed in a Global coordinate system (GCS) equal to a right-handed orthogonal triad fixed in the ground with the +Y axis upward and parallel with the gravity vector, the +X axis corresponds to the principal direction of travel or work, and the +Y perpendicular to the two. In general, the BCS is a triad fixed at the segmental centre of mass with the +X axis anterior, +Y axis proximal, and +Z defined by the right-hand rule [3]. The joint coordinate system (JCS) is established for each of the two adjacent body segments, and the relative orientation is often parameterised using the Grood and Suntay's [4] or a similar convention. The latter is conceptual and easily communicable to clinicians and includes the calculations of clinically relevant joint rotations and translations.

The ISB describes how to define the BCS using the markers positioned on anatomical points, but it does not specify any general rules for IMU MoCap systems. It is up to the researcher to choose the anatomical system definition and the biomechanical model that best meets the needs. Similarly, there is no standard to follow for scaling the segment length and individuating the position of the centre of mass.

However, an approach for developing biomechanical models for IMU MoCap evaluation is based on statistical anthropometric models. These models describe human body size and shape using measurable features, such as body heigh and

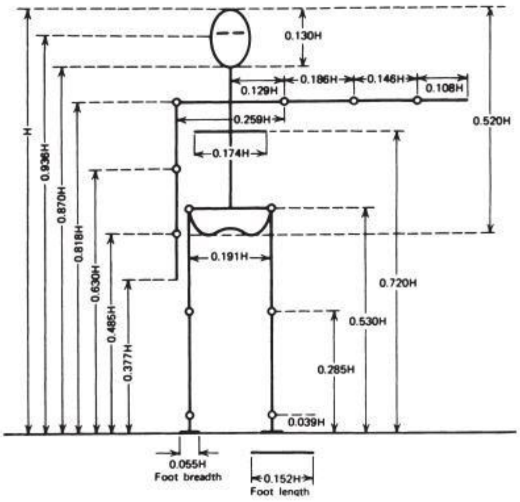

Figure 1 *Drillis and Contini model [5]*

weight. Even though body parameters are significantly influenced by body build, age, sex, ethnic origin, and diseases, some researchers gathered enough data to build statistical significance scaling laws for determining the inertia parameters and dimensions of each body segment. Some examples are the Drillis and Contini [5] and De Leva [6] models. Both individuate the value of segment length, the position of the centre of mass, mass, and moment of inertia from the body's total mass and height. Figure 1 shows the Drillis and Contini anthropometric model, where H is the to total height of the subject. It is the simplest model in the literature, in fact the De Leva models requires as input the length between two shoulders and the two hips, the foot length and width and the ankle position with respect to the ground floor.

Since there are no ISB recommendations specifically for the biomechanical model to use with IMUs, commercial IMU systems and software all use different models. One of the more impactful drawbacks is the difficulty of defining a systematic and robust protocol for evaluating the angle movements and comparing the motion results with other commercial systems and musculoskeletal models. Differences in the BCS and CCS definition and body inertial properties among different biomechanical systems causes miscalculation both in the kinematic and dynamics results. For example, XSens [7] claims to combine the Drillis and Contini model with measured body dimensions, such as arm span and foot size, for scaling the biomechanical models. Differently, the Shadow software proposes two different skeletal models, only dependent on human height.

It is not clear which anthropometric model better describes the length of each segment thus we developed a simple study for choosing the model to use in our motion tracking algorithm.

2.1.1 Comparison between anthropometric models

Three subjects (2 male and 1 female) with an average height of 1.714 m, are selected for the study. The objective is to compare the length values obtained by the different anthropometric models and comparing with the true values measured manually with a calibre. Small square tapes are fixed to the subject's anatomical points, as shown in Figure 2. The distances between all those are measured and set as reference.

The anthropometric models compared are Drillis and Contini, De Leva, and one of the two models implemented inside the Shadow Motion Software. It scales all the segments with the total height as input. Table 1 reports the percentage of error over the length of 8 principal segments as:

$$E = \frac{l_{meas} - l_{model}}{l_{meas}} \cdot 100 \tag{1}$$

where l_{meas} is the measured segment 's length and l_{model} is the estimated one.

__Figure 2__ Pictures of the three subjects for the anthropometric study

***Table 4** Percentage of error E in the estimation of segment's length for different anthropometric models*

	Subject 1			Subject 2			Subject 3		
	Drillis	De Leva	Shadow	Drillis	De Leva	Shadow	Drillis	De Leva	Shadow
Head	4.50	17.24	25.70	11.00	21.00	30.08	0.50	9.68	21.08
Trunk	2.30	8.59	3.60	1.00	4.31	6.80	2.70	8.92	3.30
Thigh	7.70	14.35	11.50	8.80	26.36	12.60	7.40	14.52	11.20
Leg	0.60	1.31	3.60	10.80	12.26	7.50	10.70	9.44	13.40
Foot	5.10	3.08	15.70	4.50	9.54	16.30	2.00	4.39	21.40
Arm	10.50	3.90	9.00	12.30	4.20	7.50	16.10	1.00	4.40
Forearm	1.70	8.24	4.50	0.50	3.83	2.20	8.20	2.85	5.70
Hand	2.50	4.98	3.30	5.10	12.15	10.40	8.00	6.29	13.30
Mean	4.36	7.71	9.61	6.75	11.71	11.67	6.95	7.14	11.72

The mean of the percentage of error over the eight segments' is the last value of table 1. It shows that the model that better represents the lengths over the three subjects is the Drillis and Contini model, with an average error of 6%. The De Leva model has a mean value of about 8.9%, lower than the one estimated by the Shadow model, which is less performative. The Drillis and Contini model shows the highest errors in estimating the arm length, whereas the De Leva presents one of the lowest errors in that specific segment. However, the variability over the body segments varies among the three subjects. It depends on the individual characteristics of the bodies, which are difficult to detect by a model that considers only the height as an input parameter. Drillis and Contini's model uses the same scaling law for men and women. Conversely, the De Leva model differs in the values among different sex. However, the latter makes worst predictions in estimating the segment length for the woman subject (number 2) than the other two. Thus, this sex differentiation seems not to improve the overall estimation. One reason could be that the De Leva model comprehends a dataset based mostly on the Russian population, composed of Caucasian (white) individuals. The height of our female subject is 1.59 meters and could be lower than the average population datasets. Thus, the Drillis and Contini model definition is the most suitable for our application. It is implemented for the application from now on.

However, it is clear that residual errors in length will affect the position analysis of IMU MoCap systems. A more performing protocol would measure manually the segment length and correct the anthropometric model. Nevertheless, this implicates a more time-consuming calibration phase which is not always feasible in industrial applications. A possible solution would be to estimate the subject's lengths with external equipment, such as cameras. Supposing to develop an IMU suit integrated with reflective markers to be placed on joints, the distance between them could be estimated using the phone camera in a relatively short time. In this direction, we perform a simple study by implementing in Matlab, an image processing procedure that automatically estimate the number of pixels between successive markers positioned over the joints. By knowing the “pixel-centimetre” scale factor is possible to estimate the segment lengths. These values define a subject-specific anthropometric model reducing the overall error in segment position estimation.

2.2 IMU Motion tracking algorithm

Sophisticated motion tracking systems must respond to two main requests: quantify the joints' kinematics to allow the identification of healthy and pathological motion parameters for rehabilitation, medicine, sports, or ergonomics, and be a flexible instrument device with a short set-up phase to facilitate its practical use. As already presented, this is particularly true for the applications presented in this Thesis, where real-time IMU MoCap algorithms have to run in real time to evaluate ergonomics indices or to interact with the robot controller.

As mentioned in chapter 1, the sensible axes of the sensors composing an IMU should be aligned together and define a technical reference frame TRF. The orientation of the sensor in space is the TRF attitude with respect to an earth-base coordinates system (ECS) in the form of unit quaternion, rotation matrices, or Euler angles. The direction of ECS depends on the sensor fusion algorithm implemented and can vary among different commercial hardware solutions. For example, the Shadow MoCap system defines an orthonormal ECS with the x-axis pointing to the south, the y-axis pointing against gravity, and the z-axis pointing to the west. Conversely, the NCS output follows the NED (North-East-Down) convention, where the x-axis is along to the north, the y-axis points to the east, and the z-axis to down according to the gravity direction.

In motion tracking, several IMUs are positioned on each human segment to analyse. Usually, for the analysis of the total human body motion, seventeen different IMUs are used. From now on, the attitude of the i-th IMU TRF with respect to ECS is denoted as ${\boldsymbol{q}_{ECS}^{TRF}}_i$. The human body segment attitude is the orientation of the corresponding BCS. Thus, for computing the kinematic, each BCS is associated to the TRF of the corresponding IMUs. The relative orientation of the IMU with respect to the body is necessary to correlate the sensor output with the segment motion and is estimated with the sensor-to-segment calibration. Once the calibration is assessed, the human joint angle is equal to the relative rotation between two consecutive segments BCS and is easily identifiable.

Since the IMU's outputs depend on the ECS definition, another virtual coordinate system (VCS) is determined during the calibration phase. This reference frame is initially similar to the previously defined GCS, fixed on the pelvis position. It is necessary to eliminate the residual angle between the body and the north-axis direction. This coordinate system will be discussed in the next paragraphs.

2.2.1 Sensor-to-segment calibration

Though no standard procedures are universally accepted to calibrate the sensors over the body segments, different methods have been proposed in the current literature, differing by complexity and tasks performed. Sensor-to-segment calibrations mostly divide into four groups [8]–[10]:

1. Manual calibration: one axis of the IMU's TRF is aligned manually with one axis of the corresponding BCS [11], [12]. It is not a straightforward procedure because it requires high user expertise to position the IMUs correctly aligned.
2. Static calibration: the subject maintains specific poses while the IMU misalignment is computationally estimated. Usually, the acceleration output, compared to the gravity vector, defines its relative orientation with respect to the segment attitude in that specific pose. By performing different poses, the complete tern is calculated [13], [14]. The accuracy of the entire calibration relies on the ability to hold a given posture precisely for a specific time, depending on the human performance. Adding external constraints, such as the one obtained by making the subject seating in a seat [15], reduces the variability over the posture and can be performed by people with reduced mobility. Another possibility is to utilize directly the IMU orientation instead of the accelerometer signals [16]. For example, [17] performs 23 different static poses, collecting the quaternions of all the IMUs and finding the final calibration matrices with mean and linear regression among all the experimental

poses. Static calibration is straightforward, easy, and fast and is usually the starting point for more complex types of calibration.

3. Dynamic calibration: the subject performs different types of movements of variable complexity, such as elbow or knee flexion-extension of leg squats. The oldest and more common approach computes the axis of rotation of a specific joint from gyroscope output integration [18], [19]. Other procedures use more sophisticated algorithms, such as PCA, to estimate the principal axis of calibration [20]. The base of this approach is that the movements have to be performed accurately and strictly in an anatomical plane so as to calculate from the gyroscope signals an axis orthogonal to that plane. With two complementary movements over the same joint, an anatomical plane is normal to two functional axes' directions [21]. This procedure is more similar to the standards for optoelectronic systems for estimating anatomical reference frames.
   Another approach is to exploit kinematic constraints of the joints during functional movements through Gauss-Newton algorithms. It has been implemented for 1 DOF joint of knees [22]–[24], and for 2 DOF elbow joints [25]. This method is particularly adapted to hinge joints and less for spherical joints that require motion mostly around all three axes, thus resembling the classical functional methodology [26].
4. CAST protocol: the examiner uses a device, such as cameras and markers, placed on the IMUs, to locate anatomical landmarks or a segment axis respecting the IMU's TRS[27], [28]. This protocol is quite old, bulky, and costly due to the usage of an external device. It is preferred for ambulatory or clinical analysis where very high accuracy is requested, but it is not suitable for other types of applications.

Quite often, these different methods are combined to use all advantages of the different techinques into a unique solution that better describes the sensor orientation over the body [29]–[31]. Additionally, the Xsens company (Xsens Technologies, NED), which is one of the leader in the field, claims to fuse, during the calibration phase, the information of 2 static poses with the one obtained during a normal-speed walking through a machine learning algorithm [7].

A more complete review of the different types of calibration perfomed and an extensive list of works can be find in [8], [10], [32].

Moreover, some researchers compared sensor-to-segment calibrations for upper limbs [33], lower leg [26], and full-body [34]. The three studies compare angle joints resulting from IMUs kinematics after different calibration techniques, with angle joints measured with optoelectronic systems, considered the gold standard in biomechanics. However, this comparison method can suffer from systematic errors: firstly, all BCS defined with marker instrumentation follow a precise protocol, and the joint angle axis can differ from the one obtained with inertial sensors. These small misalignments could affect the joints' results, especially for non-planar movements and complex joint anatomy. Moreover, both the technology used suffers from soft tissue artifacts problems due to the motion of the wearable sensors over the body. The effect of these errors is different among the two systems, is stochastic, and not predictable, and the numerical identification in terms of general accuracy is difficult to estimate in advance. These could alter the "true" angle joints estimation and add noise to the comparison of the systems. However, at this moment, this is the only plausible setup for comparing and studying human motion kinematics. Regarding static poses, Robert-Lachaine et al. [34] compared two common single-pose calibrations (N-pose and T-pose) pointing out that, for the total body kinematics, single T-pose is more accurate than N-pose. However, Lebleu et al. [26] confirmed that for lower leg kinematics, the results are more accurate by applying functional calibration movements. Instead, Bouvier et al. [33], for upper limb kinematics, do not find significant differences between static poses by adding some calibration movements to the protocol.

More investigation needs to be done to assess and validate the best sensor-to-segment algorithm. It is challenging for the high variability due to the IMU performances (magnetic disturbances or less performing sensor fusion algorithms), the type of biomechanical model used, the movements and experimental protocol to perform, and finally, for the comparison method with a gold standard MoCap system.

2.2.2 Proposed IMU MoCap system calibration

To summarize, the coordinate systems involved in the sensor-to-segment calibration are:

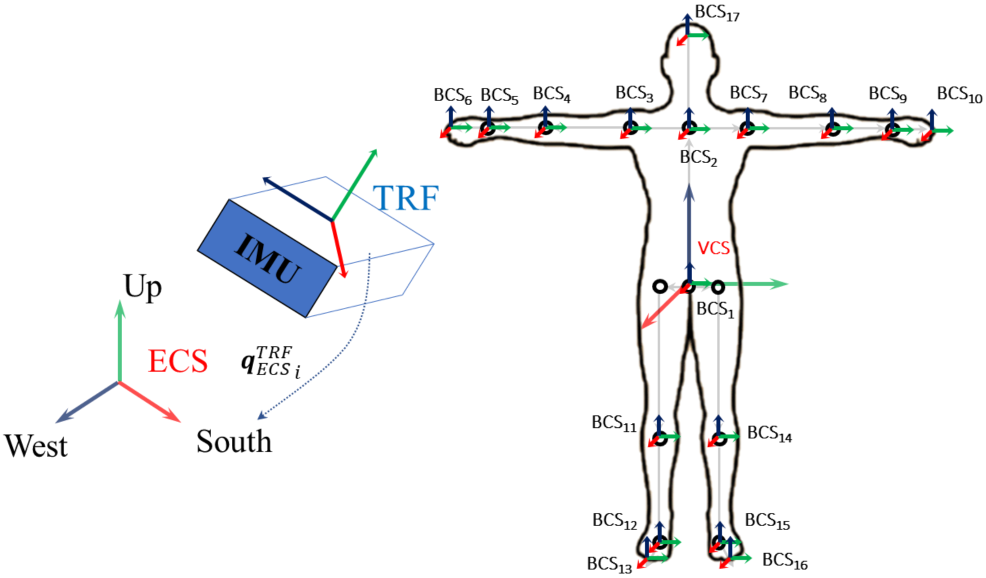

Figure 3 *Coordinates systems identified by the RGB triad (red: x-axis, green: y-axis, blue: z-axis)*

- TRF: Technical Reference Frame attached to the case of each IMU
- ECS: Earth Coordinates System in which the IMU's output is expressed.
- BCS: Body Coordinate System of each human body segments
- VCS: Virtual Coordinate System in which the human motion has to be expressed.

Figure 3 shows these reference systems.

Thus, the i-th body orientation is expressed into VCS for each time *t* ($\boldsymbol{q}_{VCS\,i}^{BCS}(t)$) through:

$$\boldsymbol{q}_{VCS\,i}^{BCS}(t) = \boldsymbol{q}_{ECS}^{VCS^*} \otimes \boldsymbol{q}_{ECS}^{TRF}(t)_i \otimes \boldsymbol{q}_{TRF\,i}^{BCS} \tag{2}$$

where $\otimes$ denotes the quaternion multiplication and * the conjugate of the quaternion. Moreover, $\boldsymbol{q}_{TRF\,i}^{BCS}$ is the relative orientation between the *i-th* BCS and the corresponding TRF estimated with the sensor-to-segment calibration, $\boldsymbol{q}_{ECS}^{TRF}(t)_i$ is the quaternion output of the *i-th* IMU, and $\boldsymbol{q}_{ECS}^{VCS}$ is the misalignment between the VCS and the ECS and is equal for each IMUs. Since the first assumption is that the sensors are rigidly attached to the body, both the $\boldsymbol{q}_{TRF\,i}^{BCS}$ and $\boldsymbol{q}_{ECS}^{VCS}$ are assumed constant during all MoCap analyses and are defined during the calibration phase.

The formalism of the relative orientation between VCS and ECS introduced here is useful to express the motion in a well-known reference system and overcome the dependencies of the output with the ECS, which is hard to evaluate and define, especially when the motion-tracking algorithms work in combination with other external systems, such as robots. Usually, in pure motion tracking algorithms, the orientation of the subject with respect to the north pole is detected during the calibration phase, and the human reconstruction starts by rotating the virtual skeleton of that specific value. Thus, after the sensor-to-segment calibration, the relative angles between two subsequent segments are calculated to drive the motion of the virtual human model. Conversely, in our approach, the dependence on the ECS is overcome by pre-multiplicating the sensor output with a specific rotation, thus tracking the body initially in a reference frame with the same orientation as the bodies at calibration. This approach is particularly succesfull when the position and orientation estimated by the IMU MoCap systems have to be referenced to another external reference frame, such as the robot coordinates systems.Thus, it is sufficient to define the relative position and orientation between the subject's initial pose and the external reference frame for integrating the two different environments. In this way, it is not necessary to use an external device such as in the work of [16], thus reducing the overall cost and redundancy of sensors. Even if the formalization of VCS is simple and it is common practice for marker-based MoCap system protocols, is new for IMU MoCap application. Moreover, with this definition, this misalignment is easily definable and will be discussed further in the chapter relating to the IMU MoCap system integration with collaborative robots.

The value of $\boldsymbol{q}_{ECS}^{VCS}$ is determined during the calibration phase and depends on the orientation of the sensor with respect to the VCS, which is equal to the BCS of each segment, at the first instants. In particular, it is a right-handed orthogonal triad fixed in the midpoint between the hips with the +Z axis upward and parallel with the gravity vector, the +X axis points anteriorly, and the +Y is perpendicular to the two. It can be calculated with the output of each IMU, whose orientation on the body is fixed and known. In the proposed calibration procedure, all IMUs can be placed with a random attitude except the one used for the $\boldsymbol{q}_{ECS}^{VCS}$ definition. We usually consider the IMU placed on the hips when we track the motion of the complete human body, or the one on the scapula, when we record only the upper limbs, supposing that those are fewer subjects to involuntary movements than the other IMUs during the recording sessions. For example, the IMU over the pelvis is usually positioned with its TRF’s z-axis and the x-axis aligned with the VCS’s y-axis and z-axis, respectively. Thus, the relative orientation between the two-reference frames over the hips ($\boldsymbol{q}_{TRF\,hips}^{VCS}$) is easily estimable. Hoverer, it is complex to align one TRF axis with the gravity vector direction since the body anatomy is variable and not rigid. Thus, its misalignment with respect to the vertical is estimated with the accelerometer output and used to correct the first estimation of $\boldsymbol{q}_{TRF\,hips}^{VCS}$. Then the relative rotation between the virtual frame and the Earth frame is equal to:

$$\boldsymbol{q}_{ECS}^{VCS} = \boldsymbol{q}_{ECS\,hips}^{TRF}(0^{*}) \otimes \boldsymbol{q}_{TRF\,hips}^{VCS} \tag{3}$$

where t=0* indicates the instant of calbration that last 3 seconds. The sensor quaternion output $\boldsymbol{q}_{ECS\,hips}^{TRF}$ is averaged in a 3 seconds range to reduce the overall noise. The average among quaternions is found with the algorithm described in [35].

Once the rotation between the ECS and VCS is defined, the sensor-to-segment calibration can be executed. The logic is to perform several static poses and average the results obtained by the three. Moreover, this calibration orientation estimation is corrected by performing specific functional movements of joints. This paragraph describes the logic behind static and dynamic calibration, but the actual experimentation will be discussed in the next section.

<u>Static sensor-to-segment calibration</u>

The BCS of each segment is defined while the subject performs the T-pose. It is a standing position with arms horizontally with the palms pointing downward. Differently from the ISB standards detailed in Section 2.1, the BCS in the T-pose has the +Z pointing up along the gravity direction, the +X axis pointing forward in the sagittal plane, and the +Y axis forms a right-handed system. This definition is like the ISB, with the difference that the Y and Z axes are switched together. During the T-pose, all BCSs have identical orientations that are also identical to the VCS frame definition. Then, $\boldsymbol{q}_{VCS}^{BCS}$ is equal to the unit quaternion for each IMU:

$$\boldsymbol{q}_{VCS_i}^{BCS}(0^{*}) = \boldsymbol{q}_{ECS}^{VCS^{*}} \otimes \boldsymbol{q}_{ECS}^{TRF}(0^{*})_i \otimes \boldsymbol{q}_{TRF_i}^{BCS} = [1\ 0\ 0\ 0] \tag{4}$$

Then, from (3) the value of ${}_t\boldsymbol{q}_{TRF_i}^{BCS}$ of each *i-th* IMU at T-pose is obtained:

$${}_t\boldsymbol{q}_{TRF_i}^{BCS} = \boldsymbol{q}_{ECS}^{TRF}(0^{*})_i^{\,*} \otimes \boldsymbol{q}_{ECS}^{VCS} \tag{5}$$

During the N-pose, the subject is asked to stand straight with the two arms along the body with the palms pointing internally. Compared to the T-pose, there is a

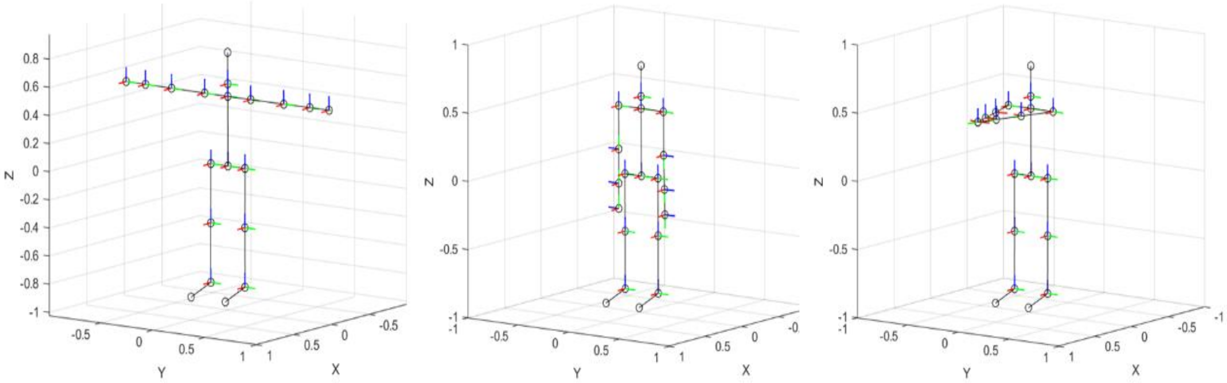

Figure 4 *Skeleton representation of T-pose, N-pose, and C-pose*

rotation of about 90° on the anteroposterior shoulder axis. Then, by supposing that the motion is a pure revolution on the frontal plane for both the arms, the relative orientation of their BCSs with respect to the fixed and previously defined VCS is equal to a pure rotation of ± 90°, depending on the arm considered, along the VCS x-axis. Then, in the N-pose, the $\boldsymbol{q}_{VCS_i}^{BCS}$ of the arms is:

$$\boldsymbol{q}_{VCS_i}^{BCS}(0^*) = \boldsymbol{q}_{ECS}^{VCS^*} \otimes \boldsymbol{q}_{ECS}^{TRF}(0^*)_i \otimes \boldsymbol{q}_{TRF_i}^{BCS} = \frac{\left[\frac{\pi}{4} \quad \pm\frac{\pi}{4} \quad 0 \quad 0\right]}{\left\|\left[\frac{\pi}{4} \quad \pm\frac{\pi}{4} \quad 0 \quad 0\right]\right\|} \tag{6}$$

Then the ${}_{n}\boldsymbol{q}_{TRF_i}^{BCS}$ is equal to:

$${}_{n}\boldsymbol{q}_{TRF_i}^{BCS} = \begin{cases} \boldsymbol{q}_{ECS}^{TRF}(0^*)_i^{\ *} \otimes \boldsymbol{q}_{ECS}^{VCS} \otimes \dfrac{\left[\frac{\pi}{4} \quad \pm\frac{\pi}{4} \quad 0 \quad 0\right]}{\left\|\left[\frac{\pi}{4} \quad \pm\frac{\pi}{4} \quad 0 \quad 0\right]\right\|} & i = arms \\ \boldsymbol{q}_{ECS}^{TRF}(0^*)_i^{\ *} \otimes \boldsymbol{q}_{ECS}^{VCS} & i \neq arms \end{cases} \tag{7}$$

The T-pose and N-pose are standard poses, usually implemented in most static calibration procedures. We propose a new pose dependent on the length of the arms and shoulders. In the so-called C pose, the subject, starting from the T-pose, closes the hand in front of his chest, maintaining both the arm as much straight as possible and the palms pointing downward. Figure 5 shows the proposed position.

Thus, the angle of the arms with the front plane is equal to:

$$\theta = \pi - cos^{-1}\frac{|\boldsymbol{p}_{shoulder} - \boldsymbol{p}_{thorax}|}{|\boldsymbol{p}_{hand} - \boldsymbol{p}_{shoulder}|} \tag{8}$$

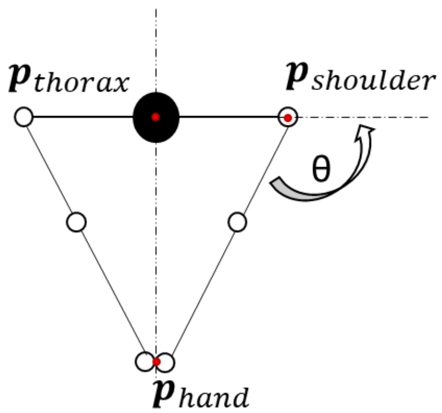

Figure 5 *Top-view of the skeleton in C-pose*

where the argument of the arc cosine is the ratio between the shoulder and arm length. Specifically, vector $\boldsymbol{p}$ indicates the position vector of the anatomical part. Thus, the $\boldsymbol{q}^{BCS}_{VCS_i}(0^*)$ during the C-pose can be supposed to be a rotation about the VCS z-axis equivalent to:

$$\boldsymbol{q}^{BCS}_{VCS_i}(0^*) = \boldsymbol{q}^{VCS^*}_{ECS} \otimes \boldsymbol{q}^{TRF}_{ECS}(0^*)_i \otimes \boldsymbol{q}^{BCS}_{TRF_i} = \frac{\left[\cos\frac{\theta}{2} \quad 0 \quad 0 \quad \pm\sin\frac{\theta}{2}\right]}{\left\|\left[\cos\frac{\theta}{2} \quad 0 \quad 0 \quad \frac{\theta}{2}\right]\right\|} \tag{9}$$

Then the corresponding ${}_{c}\boldsymbol{q}^{BCS}_{TRF_i}$ is:

$${}_{c}\boldsymbol{q}^{BCS}_{TRF_i} = \begin{cases} \boldsymbol{q}^{TRF}_{ECS}(0^*)_i^{\,*} \otimes \boldsymbol{q}^{VCS}_{ECS} \otimes \dfrac{\left[\cos\frac{\theta}{2} \quad 0 \quad 0 \quad \pm\sin\frac{\theta}{2}\right]}{\left\|\left[\cos\frac{\theta}{2} \quad 0 \quad 0 \quad \frac{\theta}{2}\right]\right\|} & i = arms \\ \boldsymbol{q}^{TRF}_{ECS}(0^*)_i^{\,*} \otimes \boldsymbol{q}^{VCS}_{ECS} & i \neq arms \end{cases} \tag{10}$$

Technically, the quaternions obtained with the three different calibrations of each *i-th* IMUs should be equal since they defined the orientation of the sensor’ TRS over the corresponding BCS. However, they slightly differ due to inaccuracies in estimating the sensor attitude in different known poses. Thus, the overall noise is reduced by geometrically averaging the results obtained from different static calibration poses. The geometric average is the algorithm cited previously. In this contest, only the sensors’ orientations over the bodies' coordinate systems are assessed. The IMU is rigidly attached to the segment body in a fixed position near the corresponding distal joints. This position has been suggested in other works regarding IMU MoCap systems. However, the effects of different IMU positioning in final joint angle estimation are not systematically clarified.

Dynamic sensor-to-segment calibration

The most common approach for dynamic calibration is the one described in [18], where the orientation of the IMU with respect to the forearm is found by elbow pronation-supination movements, assuming that the angular velocity during the motion is in the direction of the joint axis. This axis, in combination with the results of other movements, is then used to define a triplet specifically for that specific IMUs and the corresponding joints. Since it is fundamental for our application to develop an IMU MoCap strategy able to run in real-time (100 Hz), we study the capability of substituting the calculous of the axis performed with gyroscope signals with a similar computation using the quaternion. Thus, the data to stream to the robot controller consist of the solo quaternion output and not the gyroscope's raw data, reducing the total number of packages to transmit. According to the movement axis, the vector axis is defined, for each instant t of the calibration phase, by the numerical quaternion derivative:

$$X_m(t) = \frac{\omega_m}{|\omega_m|} = \frac{2\, Im\left(\boldsymbol{q}_{ECS}^{TRF}(t)_i^{\,*} \otimes \boldsymbol{q}_{ECS}^{TRF}(t+1)_i\right)}{\left|2\, Im\left(\boldsymbol{q}_{ECS}^{TRF}(t)_i^{\,*} \otimes \boldsymbol{q}_{ECS}^{TRF}(t+1)_i\right)\right|} \tag{11}$$

The direction of the axis is the vector average of the results of three controlled repetitive movements. However, these axis directions computed in each instant have opposite directions, according to the motion performed. Then, the classic mathematical mean can output a value null. Thus, the geometric mean is calculated similarly to the average quaternion formulation. Considering n vectors $\boldsymbol{v}$, the matrix $\boldsymbol{M}$ corresponds to:

$$\boldsymbol{M} = \sum_{i=1}^{n} \boldsymbol{v}_i \boldsymbol{v}_i^T \tag{12}$$

Then the average vector $\overline{\boldsymbol{v}}$ is equal to:

$$\overline{\boldsymbol{v}} = \underset{v \in S^3}{\operatorname{argmax}} (\boldsymbol{v}^T \boldsymbol{M} \boldsymbol{v}) \tag{13}$$

which is the eigenvector of M corresponding to the maximum eigenvalues.

2.2.3 Motion algorithm

Once the calibration is over, the actual motion algorithm takes part. The joint quaternion $\boldsymbol{q}_{i,j}^{Joint}(t)$ is the relative orientation between the *i-th* and *j-th* subsequent segments. For each instant t:

$$\begin{aligned}\boldsymbol{q}_{i,j}^{Joint}(t) = {} & \boldsymbol{q}_{VCS_i}^{BCS}(t)^* \otimes \boldsymbol{q}_{VCS_j}^{BCS}(t) = \\ & = \boldsymbol{q}_{TRF_i}^{BCS\,*} \otimes \boldsymbol{q}_{ECS_i}^{TRF}(t)^* \otimes \boldsymbol{q}_{ECS_j}^{TRF}(t) \otimes \boldsymbol{q}_{TRF_j}^{BCS}\end{aligned} \tag{14}$$

This term is independent of ECS and VCS both and is advantageous for performing ergonomics studies and biomechanical analysis. This equation is calculated recursively along each body chain, starting from the root of all the chains. The orientation of the first joint is calculated through the complete equation:

$$\boldsymbol{q}_{VCS_1}^{BCS}(t) = \boldsymbol{q}_{ECS}^{VCS^*} \otimes \boldsymbol{q}_{ECS_1}^{TRF}(t) \otimes \boldsymbol{q}_{TRF_1}^{BCS} \tag{15}$$

The first joint position is equal to zero, coincident with the origin of VCS. The positions of the other joints $\vec{\boldsymbol{p}}_j(t)$ is calculated recursively, with respect to VCS, by summing the position of the previous *i-th* joints with the segment vector $\vec{\boldsymbol{v}}_{i,j}$, connecting the *i-th* joints with the *j-th*, rotated by the corresponding angle joint $\boldsymbol{q}_{i,j}^{Joint}(t)$. Mathematically, it is equal to:

$$q\left(\vec{\boldsymbol{p}}_j(t)\right) = q\left(\vec{\boldsymbol{p}}_i(t)\right) + \boldsymbol{q}_{i,j}^{Joint}(t) \otimes q\left(\vec{\boldsymbol{v}}_{i,j}\right) \otimes \boldsymbol{q}_{i,j}^{Joint}(t)^* \tag{16}$$

where $q(\cdot)$ is the pure quaternion representation of the 3D vector.

2.3 Comparison between sensor-to-segment algorithms

Similar to other works that compare several sensor-to-segment algorithms [26], [32], [33], we tested the effectiveness of our formalizations by comparing the angle joints obtained with the one measured by an optoelectronic system which is considered a gold standard in biomechanics. The objective is to define a fast, simple, and reliable calibration methodology that can be performed by the operator without using any external equipment in a relatively short time. This approach is based on first performing static poses and then correcting the first estimation with dynamic calibration. In particular, we focus our attention on the elbow and wrist for the upper limbs and on the knee and ankle for the lower limbs. For each of these joints, two functional movements are performed, whose axes define the rotation matrix representing the orientation of the IMU over the body segment. This matrix contains the 3 unit vectors of the *i-th* body segment axes (BCS) with respect to the corresponding IMU coordinate systems (TRF):

$$\boldsymbol{R}_{TRF_i}^{BCS} = \begin{bmatrix} x_{TRF_i}^{BCS} & y_{TRF_i}^{BCS} & z_{TRF_i}^{BCS} \end{bmatrix} \tag{17}$$

The quaternion $\boldsymbol{q}_{TRF_i}^{BCS}$ corresponds to the latter rotation matrix. The next section describes the methodologies to define those axes for each joint. Then the experimental setup and the results will be discussed.

2.3.1 Joints functional movements

Elbow motion:

For the elbow, two different motions are performed: 1) the elbow flexion extension and 2) elbow pronation-supination. For each test, the body is maintained in the N-pose with all the body segments static and moving only the forearm with precise and constant movements. Figure 6 shows a schematic representation of the motion. The axes are estimated from the quaternion output by the IMU positioned on the forearm during all the instants of three repetitions, using Eq. 11. Specifically, the axis defined by the elbow flexion-extension is $\boldsymbol{J}_{elbow}^{flex}$, and the one obtained by the pronation-supination is $\boldsymbol{J}_{elbow}^{sup}$. The direction of this axis is chosen to be in the same direction as the corresponding axis defined by the quaternion $\boldsymbol{q}_{TRF_{elbow}}^{BCS}$ computed with the static T-pose. Since the flexion-extension of the elbow is a simpler and more controlled movement, the axes of the rotation matrix are defined as:

$$\begin{gathered}
\boldsymbol{z}_{TRF_{elbow}}^{BCS} = \boldsymbol{J}_{elbow}^{flex} \\
\boldsymbol{x}_{TRF_{elbow}}^{BCS} = \boldsymbol{J}_{elbow}^{sup} \wedge \boldsymbol{z}_{TRF_{elbow}}^{BCS} \\
\boldsymbol{y}_{TRF_{elbow}}^{BCS} = \boldsymbol{z}_{TRF_{elbow}}^{BCS} \wedge \boldsymbol{x}_{TRF_{elbow}}^{BCS}
\end{gathered} \tag{18}$$

Wrist motion:

With an identical approach to the elbow motion, the axes of the wrist are defined by the output of the IMU positioned on the hands, with 1) flexion-extension movements $\boldsymbol{J}_{wrist}^{flex}$ and 2) abduction and adduction movements $\boldsymbol{J}_{wrist}^{abd}$. The corresponding rotation matrix axes are defined, starting from $\boldsymbol{J}_{wrist}^{flex}$, as:

$$\begin{gathered}
\boldsymbol{x}_{TRF_{wrist}}^{BCS} = \boldsymbol{J}_{wrist}^{flex} \\
\boldsymbol{y}_{TRF_{wrist}}^{BCS} = \boldsymbol{J}_{wrist}^{abd} \wedge \boldsymbol{x}_{TRF_{wrist}}^{BCS} \\
\boldsymbol{z}_{TRF_{wrist}}^{BCS} = \boldsymbol{x}_{TRF_{wrist}}^{BCS} \wedge \boldsymbol{y}_{TRF_{wrist}}^{BCS}
\end{gathered} \tag{19}$$

Knee motion:

Differently, the knee is usually approximated with a single revolute joint depending on the flexion-extension axis $\boldsymbol{J}_{knee}^{flex}$. Thus, the rotational triad relies on that angle and the z-axis ${\boldsymbol{z}_{TRF}^{BCS}}_{knee}^{Tpose}$ computed with the T-pose. The final axes are defined as:

$$
\begin{aligned}
{\boldsymbol{y}_{TRF}^{BCS}}_{knee} &= \boldsymbol{J}_{knee}^{flex} \\
{\boldsymbol{x}_{TRF}^{BCS}}_{knee} &= {\boldsymbol{y}_{TRF}^{BCS}}_{knee} \wedge {\boldsymbol{z}_{TRF}^{BCS}}_{knee}^{Tpose} \\
{\boldsymbol{z}_{TRF}^{BCS}}_{knee} &= {\boldsymbol{x}_{TRF}^{BCS}}_{knee} \wedge {\boldsymbol{y}_{TRF}^{BCS}}_{knee}
\end{aligned}
\tag{20}
$$

Ankle motion:

The ankle motion axes are defined by 1) dorsiflexion-plantarflexion motion $\boldsymbol{J}_{ankle}^{flex}$ and 2) inversion-eversion motion $\boldsymbol{J}_{ankle}^{inv}$. The motions are performed in standing position, in two different moments for right and left foot. The subject can balance the equilibrium by leaning to a fixed surface, trying to remain as straight as possible. The axes are computed as:

$$
\begin{aligned}
{\boldsymbol{z}_{TRF}^{BCS}}_{ankle} &= \boldsymbol{J}_{ankle}^{inv} \\
{\boldsymbol{x}_{TRF}^{BCS}}_{ankle} &= \boldsymbol{J}_{ankle}^{flex} \wedge {\boldsymbol{z}_{TRF}^{BCS}}_{ankle} \\
{\boldsymbol{y}_{TRF}^{BCS}}_{ankle} &= {\boldsymbol{z}_{TRF}^{BCS}}_{ankle} \wedge {\boldsymbol{x}_{TRF}^{BCS}}_{ankle}
\end{aligned}
\tag{21}
$$

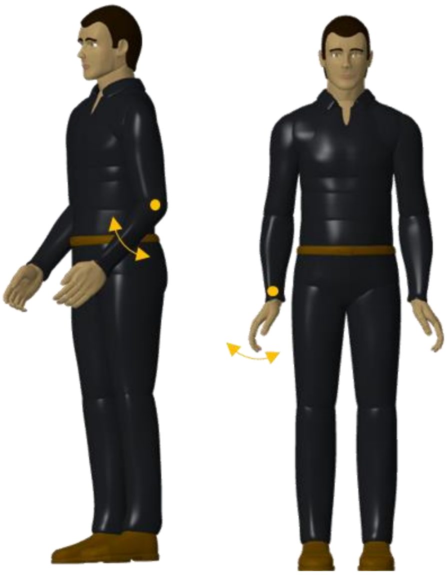

Figure 6 *Representation of Left) elbow flexion extension movements, Right) wrist flexion-extension movements*

2.3.2 Material and Methods

The wearable Shadow MoCap Suit and the optoelectronic Vicon system (©Vicon Motion Systems Ltd) are the sensors used to compare the results of different sensor-to-segment calibration methods. A man subject (172 cm, 62 Kg, 27 years old) with no mobility dysfunctions wears both the IMUs attached with tapes and straps and 42 reflective markers following the Plug-in-Gait (PiG) model available with the Vicon/Nexus software package. Figure 7 shows the sensor setup and disposition. The Vicon optoelectronic system consists of 6 Bonita and 2 Vero cameras, processing data within Nexus 2.5, and keeping all system settings at default values. The camera calibration is performed by sweeping the Vicon active wand in the entire control volume, using at least 3000 frames per camera. The Shadow Mocap sends the sensor output to a PC wireless with a frequency of 100 Hz, which saves data in a .csv file. The results are post-processed offline. The experiments are performed outdoors in a shaded area to have IMU signals without magnetometer interferences, thus analysing only the effect of the calibration algorithms and not errors in attitude computation of the IMU sensors. The subject performs a series of movements to calibrate the IMU MoCap systems, while the motion is captured simultaneously by the two hardware. The synchronization between the two systems occurs standing up on tiptoe at the beginning of each

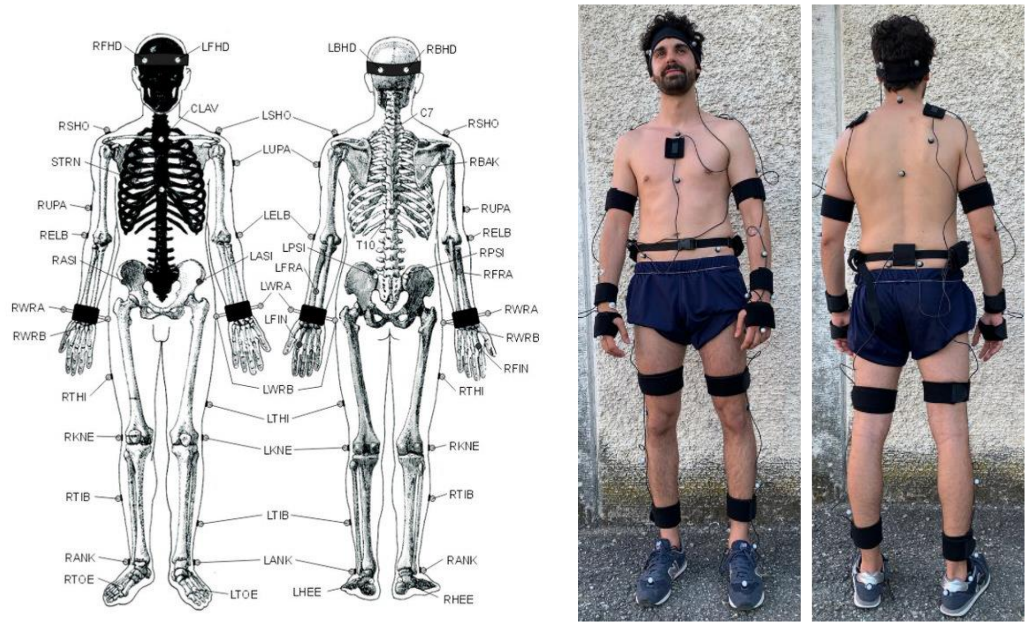

Figure 7 *Left: Plug-in-gate protocol, Right: Experimental set-up with markers and IMUs*

recording session. The Vicon data are exported as c3d file by Nexus 2.0 after a process of labelling, filtering, and filling markers' gaps. For determining the angle joints, we used a standard model and we import the motion data into the Anybody Modelling System (AMS), with a process that will be described accurately in the next chapters. The AMS output the joint angles, which are compared with the ones obtained with the IMU systems with different calibration methods. The comparison is developed offline in Matlab 2020a.

Different sensor-to-segment procedures of upper limbs are compared and listed in Table 2. Since the purpose is to develop a fast and reliable IMU MoCap calibration for ergonomics evaluation of upper limbs, the algorithms for the lower limbs are only proposed and implemented but not fully tested and detailed results will not be reported here. Briefly, visually the motion of the lower leg is coherent with reality using only the static poses, while the additional movements seem to have a limited influence on the calibration accuracy, on the contrary requiring extra time that could be safe for industrial procedures, especially if the calibration process has to be repeated several times during the working shift.

One of the drawbacks of this approach is the difference between the AMS model and the IMU MoCap system. The joint coordinate system defined in AMS depends on the morphology and shapes of the bones building up the musculoskeletal model, which is scaled over the subject using the position of the markers set. The same coordinate system on our model is built differently, starting from functional

Table 5 *Tested upper limbs sensor-to-segments procedures*

Name	Activity 1	Activity 2	Activity 3
T	T-pose		
N	N-pose		
C	C-pose		
Mean Static	T-pose	N-pose	C-pose
Elbow	T-pose	Elbow motion	
Wrist	T-pose	Wrist motion	
Functional 1	Mean Static	Elbow motion	Wrist motion

references which, though being related to the morphological ones, are not perfectly coincident. Thus, the two systems differ in definition, so the computed joint angles. Similar to the approach of [33], for determining the best strategies and the trueness of the results, the RMSE of the angle excursion between the joint angles, obtained with IMUs, and the AMS results are calculated. The joint angle $\boldsymbol{q}_{i,j}^{Joint}(t)$ from the IMU MoCap systems is calculated with the method described in Section 2.2.3 and decomposed with the Euler angle method. Similar to [33], the ZXY sequence, also proposed by the ISB, is used for the elbow joint, whereas the ZYX sequence is preferred for the wrist joints. The decomposition of the shoulder is complex because, due to its elevated range of motion, can reach mathematical singularities. The ZXY sequence is chosen for the shoulder. The RMSE is calculated in different tests performing five pure joint movements: shoulder flexion and abduction, elbow flexion and pronation, and wrist flexion and abduction.

However, the intrinsic errors of this comparison procedure make the results difficult to interpret. Beyond the differences in the joint coordinate systems, soft tissue artifacts could add noises to the optoelectronic system output, and errors could occur in AMS in calculating the angle joints by analysing the trajectories of the markers. Other differences due to distinct joint angle decomposition sequences between the models could cause misleading results. Another simple test evaluation is performed to overcome this problem. Starting from the N-pose, the subject closes his hands and executes random movements in the horizontal

Figure 8 *Hand closed test analysis in AMS*

and coronal plane. The distance between the endpoint of the hands, measured instantly for each upper limb's calibration procedure, should be proximal to zero because of the hand touching. The calibration procedure that shows the lowest values correspond to the approach that better tracks the motion of the upper limb. Figure 8 displays a frame of the test just described in AMS. Moreover, this test gives an overview of the capability of the IMU MoCap system to perform position analysis, which is of interest to the development of control strategy in collaborative robotics.

2.3.3 Results

Figure 9 shows the performance of different upper-limb sensor-to-segment calibrations proposed in the holding hand test. The test lasts almost 10 seconds, where the subject randomly moves the closed hands in front of the chest for the first 5 seconds, then above the head for the last 5 seconds. The distance between the end position of the hand is computed for each moment of the test. The T-pose performs the worst results (0.175 ± 0.042 m). The best performances are for the C-Pose (0.090 ± 0.035 m) and Functional 1 (0.098 ± 0.030 m). The similarity in the absolute values of the Elbow and Wrist calibration with the T-Pose indicates that results mainly depend on the shoulder calibration performance, which is the term that unites those algorithms and differs from the C-Pose and Functional 1.

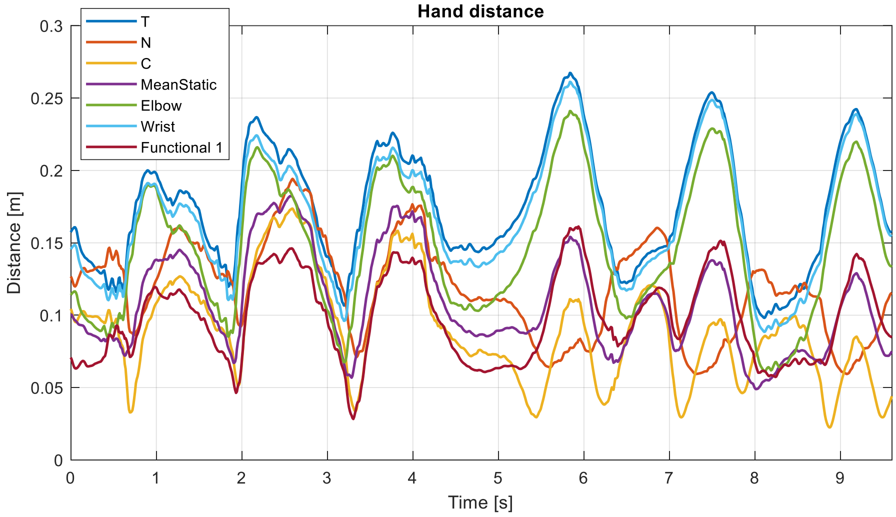

Figure 9 *Results of holding hand test of different upper limbs sensor-to-segment calibration algorithms. The theoretical values should be near 0, thus the performing algorithm is the one with the lowest values*

***Table 6** RMSE results of joint angles excursion during pure joint motion between different upper limb sensor-to-segment calibrations and AMS joint angles computed with an optoelectronic system*

	RMSE Left					
	Shoulder Flexion	Shoulder Abduction	Elbow Flexion	Elbow Pronation	Wrist Flexion	Wrist Abduction
T	8.56	8.39	4.79	17.94	10.65	10.61
N	23.43	7.32	4.64	19.67	5.33	9.57
C	8.14	7.42	5.66	18.54	8.23	11.13
Mean Static	12.34	7.47	7.20	18.67	8.90	10.70
Elbow	8.66	8.38	4.57	18.03	9.42	9.15
Wrist	8.56	8.39	4.79	17.94	9.27	5.74
Functional 1	12.34	7.47	6.76	18.23	9.24	5.69

	RMSE Right					
	Shoulder Flexion	Shoulder Abduction	Elbow Flexion	Elbow Pronation	Wrist Flexion	Wrist Abduction
T	5.39	7.58	21.82	19.41	6.51	5.24
N	30.28	6.48	4.86	20.50	5.77	11.58
C	6.27	6.20	9.64	21.11	6.38	9.04
Mean Static	11.54	6.42	1.91	20.29	7.06	8.87
Elbow	5.67	7.49	16.20	19.51	7.36	5.42
Wrist	5.39	7.58	21.82	19.41	6.43	5.90
Functional 1	11.54	6.42	2.57	19.92	6.75	8.67

Hoverer, dynamic calibration motion shows slightly better results than the standalone static pose. Nevertheless, the absolute value of the hand distance higher than zero indicates that residual errors are present in the position evaluation. In addition to mistakes in the definition of the anthropometric model underlined in Section 2.1.1, the simplified biomechanical model is a stick figure, which does not consider the volume and size of the body segments, and it could lead to additional position errors.

Table 3 gathers the RMSE of different upper limb sensor-to-segment calibrations. The values of RMSE are homogenous within the range reported by [33] and [32].

The shoulder shows 5.36° ≤ RMSE ≤ 30.28° with lower accuracy for N-Pose for the shoulder flexion. The elbow angle varies among a range of 1.91° ≤ RMSE ≤ 21.82°. The results confirm that elbow pronation-supination movements show poorer correlation and accuracy than elbow flexion-extension motion. Firstly, it is difficult to perform a pure pronation-supination elbow motion, and secondly, because the effects are "visible" on the distal part of the forearm, near the wrist joints. Thus, errors could occur in the interpretability of the elbow results by biomechanical models driven by both markers and IMUs MoCap system. The variability of the sensor-to-segment results over the left elbow is such low that there is no preferred algorithm. Differently for the right elbow, the T-Pose has the poorest outcomes. However, the poor results are averaged and corrected by the other static poses since the RMSE of the Mean Static case decades drastically. In general, the union of several pose calibrations and different techniques increases the accuracy of the evaluation and reduces the intrinsic errors of the calibration procedures. For wrist motion, the range is coherent with the literature with 5.24° ≤ RMSE ≤ 11.58°.

The proposed testing procedure is biased by analysing only pure joint motion. It is quite known that angle variability and accuracy increase with movement complexity [32]. Moreover, we tested only one subject, which is too low for a comprehensive calibration comparison. However, the acceptable results of the closing hand test confirm the validity of the proposed methods for the calibration of IMU MoCap systems.

Hoverer, the proposed sensor-to-segment calibration methods exploiting only the IMU orientation output without using the gyroscope and accelerometer signals, show results comparable to more standard approaches. The joint axis defined during the dynamic calibration by deriving the quaternion output exhibits effects equivalent to the literature that uses the gyroscope signals. Then, the algorithms proposed are promising for reducing the number of signals to stream online by the IMUs system to the PC or workstation, possibly reducing the overall latency. Additionally, the novel C-Pose definition, which adds anthropometric constraints to the calibration phase, shows encouraging results, especially if combined with other static poses or functional movements.

2.4 Conclusions

The anthropometric models and the motion tracking algorithms are tested and compared with the literature. Among the anthropometric measures, Drillis and

Contini's model shows the lowest percentage of error in the absolute value of segment length compared with measured body length. Thus, this model is chosen for all MoCap implementations, which will be described in the next chapter.

The proposed motion tracking algorithm can be integrated into any commercial IMUs system that outputs the sensor attitude estimates. The usage of quaternions is preferred when developing algorithms in real-time, however, the same logic is implementable using other orientation representations. The motion algorithm outputs the segment position and joint angle in a virtual reference frame attached to the human hips during the calibration phase. The latter is not dependent on the initial human orientation respecting the Earth's coordinates systems and makes the analysis free of this dependence. Despite the simplicity of the concept, this definition is new in the literature because the majority use IMUs systems for pure biomechanical studies where only joint angles and not the body positions in space are estimated. Also, fewer works study the usability of MoCap IMU in collaborative robotics applications. This definition is fundamental for easy integration with other external systems because only the relative position and orientation of the pelvis respect the associated reference frame origin is necessary.

Moreover, the proposed sensor-to-segment upper limbs calibration procedure shows results comparable to the literature, even if only the orientation output is used and not the raw gyroscope and accelerometer signals. This procedure consists of performing three static poses and four functional movements: T-Pose, N-Pose, and C-pose followed by flexion-extension and pronation-supination of the elbow and flexion-extension and abduction-adduction of the wrist. This procedure is relatively fast to execute since it requires a couple of minutes and shows performing results for position and angle analysis compared to the “true” motion measured with optoelectronic systems.

In conclusion, the IMU MoCap system is a promising tool for accurate track human motion. This system is wearable, low-cost, and lightweight and could constantly monitor the workers in industrial scenarios. The proposed algorithm estimates the body segments' motion but does not calculate the absolute position of the body in an external reference system. In other words, it cannot measure the distance computed by the worker by walking but can estimate the angle range motion, the position assumed, and in a second analysis, the effort performed. If the operator works stationary (such as cashiers, assembly line laborers, etc.) it could be implemented in safety control strategies of collision avoidance, whereas for moving workers is a powerful tool for measuring awkward posture or excessive effort, if integrated with force sensors. A fast calibration procedure allows being repeated several times during the working shift, thus reinitializing the system and reducing the drifting error effect. The major drawback of these systems is their high dependence on magnetic disturbances, which could be large in workshops or workplaces with high numbers of ferrous materials. However, researchers are studying sensor fusion algorithms that minimize these impactful effects or how to mitigate them by integrating other wearable and flexible sensors.

References

[1] G. Wu *et al.*, «ISB recommendation on definitions of joint coordinate system of various joints for the reporting of human joint motion—part I: ankle, hip, and spine», *Journal of Biomechanics*, vol. 35, fasc. 4, pp. 543–548, apr. 2002, doi: 10.1016/S0021-9290(01)00222-6.

[2] G. Wu *et al.*, «ISB recommendation on definitions of joint coordinate systems of various joints for the reporting of human joint motion—Part II: shoulder, elbow, wrist and hand», *Journal of Biomechanics*, vol. 38, fasc. 5, pp. 981–992, mag. 2005, doi: 10.1016/j.jbiomech.2004.05.042.

[3] G. Wu e P. R. Cavanagh, «ISB recommendations for standardization in the reporting of kinematic data», *Journal of Biomechanics*, vol. 28, fasc. 10, pp. 1257–1261, ott. 1995, doi: 10.1016/0021-9290(95)00017-C.

[4] E. S. Grood e W. J. Suntay, «A Joint Coordinate System for the Clinical Description of Three-Dimensional Motions: Application to the Knee», *Journal of Biomechanical Engineering*, vol. 105, fasc. 2, pp. 136–144, mag. 1983, doi: 10.1115/1.3138397.

[5] R. Contini, R. J. Drillis, e M. Bluestein, «Determination of Body Segment Parameters», *Hum Factors*, vol. 5, fasc. 5, pp. 493–504, ott. 1963, doi: 10.1177/001872086300500508.

[6] P. de Leva, «Adjustments to Zatsiorsky-Seluyanov's segment inertia parameters», *Journal of Biomechanics*, vol. 29, fasc. 9, pp. 1223–1230, set. 1996, doi: 10.1016/0021-9290(95)00178-6.

[7] D. Roetenberg, H. Luinge, e P. Slycke, «Xsens MVN: Full 6DOF Human Motion Tracking Using Miniature Inertial Sensors», p. 10, 2013.

[8] L. Pacher, C. Chatellier, R. Vauzelle, e L. Fradet, «Sensor-to-Segment Calibration Methodologies for Lower-Body Kinematic Analysis with Inertial

Sensors: A Systematic Review», *Sensors*, vol. 20, fasc. 11, p. 3322, giu. 2020, doi: 10.3390/s20113322.

[9] P. Picerno, «25 years of lower limb joint kinematics by using inertial and magnetic sensors: A review of methodological approaches», *Gait & Posture*, vol. 51, pp. 239–246, gen. 2017, doi: 10.1016/j.gaitpost.2016.11.008.

[10] R. V. Vitali e N. C. Perkins, «Determining anatomical frames via inertial motion capture: A survey of methods», *Journal of Biomechanics*, vol. 106, p. 109832, giu. 2020, doi: 10.1016/j.jbiomech.2020.109832.

[11] A. G. Cutti, A. Giovanardi, L. Rocchi, A. Davalli, e R. Sacchetti, «Ambulatory measurement of shoulder and elbow kinematics through inertial and magnetic sensors», *Med Bio Eng Comput*, vol. 46, fasc. 2, pp. 169–178, feb. 2008, doi: 10.1007/s11517-007-0296-5.

[12] P. Picerno, A. Cereatti, e A. Cappozzo, «Joint kinematics estimate using wearable inertial and magnetic sensing modules», *Gait & Posture*, vol. 28, fasc. 4, pp. 588–595, nov. 2008, doi: 10.1016/j.gaitpost.2008.04.003.

[13] E. Palermo, S. Rossi, F. Marini, F. Patanè, e P. Cappa, «Experimental evaluation of accuracy and repeatability of a novel body-to-sensor calibration procedure for inertial sensor-based gait analysis», *Measurement*, vol. 52, pp. 145–155, giu. 2014, doi: 10.1016/j.measurement.2014.03.004.

[14] Y.-T. Liu, Y.-A. Zhang, e M. Zeng, «Sensor to segment calibration for magnetic and inertial sensor-based motion capture systems», *Measurement*, vol. 142, pp. 1–9, ago. 2019, doi: 10.1016/j.measurement.2019.03.048.

[15] T. Maruyama, H. Toda, W. Ishii, e M. Tada, «Inertial Measurement Unit to Segment Calibration Based on Physically Constrained Pose Generation», *SICE Journal of Control, Measurement, and System Integration*, vol. 13, fasc. 3, pp. 122–130, mag. 2020, doi: 10.9746/jcmsi.13.122.

[16] N. Choe, H. Zhao, S. Qiu, e Y. So, «A sensor-to-segment calibration method for motion capture system based on low cost MIMU», *Measurement*, vol. 131, pp. 490–500, gen. 2019, doi: 10.1016/j.measurement.2018.07.078.

[17] M. Zabat, A. Ababou, N. Ababou, e R. Dumas, «IMU-based sensor-to-segment multiple calibration for upper limb joint angle measurement—a proof of concept», *Med Biol Eng Comput*, vol. 57, fasc. 11, pp. 2449–2460, nov. 2019, doi: 10.1007/s11517-019-02033-7.

[18] H. J. Luinge, P. H. Veltink, e C. T. M. Baten, «Ambulatory measurement of arm orientation», *Journal of Biomechanics*, vol. 40, fasc. 1, pp. 78–85, gen. 2007, doi: 10.1016/j.jbiomech.2005.11.011.

[19] W. H. K. de Vries, H. E. J. Veeger, A. G. Cutti, C. Baten, e F. C. T. van der Helm, «Functionally interpretable local coordinate systems for the upper extremity using inertial & magnetic measurement systems», *Journal of Biomechanics*, vol. 43, fasc. 10, pp. 1983–1988, lug. 2010, doi: 10.1016/j.jbiomech.2010.03.007.

[20] «Duong et al. - 2019 - Improving the Accuracy of Wearable Sensors for Hum.pdf».

[21] J. Favre, R. Aissaoui, B. M. Jolles, J. A. de Guise, e K. Aminian, «Functional calibration procedure for 3D knee joint angle description using inertial sensors», *Journal of Biomechanics*, vol. 42, fasc. 14, pp. 2330–2335, ott. 2009, doi: 10.1016/j.jbiomech.2009.06.025.

[22] A. Küderle, S. Becker, e C. Disselhorst-Klug, «Increasing the Robustness of the automatic IMU calibration for lower Extremity Motion Analysis», *Current Directions in Biomedical Engineering*, vol. 4, fasc. 1, pp. 439–442, set. 2018, doi: 10.1515/cdbme-2018-0104.

[23] T. Seel, T. Schauer, e J. Raisch, «Joint axis and position estimation from inertial measurement data by exploiting kinematic constraints», in *2012 IEEE International Conference on Control Applications*, Dubrovnik, Croatia, ott. 2012, pp. 45–49. doi: 10.1109/CCA.2012.6402423.

[24] Q. Hu, L. Liu, F. Mei, e C. Yang, «Joint Constraints Based Dynamic Calibration of IMU Position on Lower Limbs in IMU-MoCap», *Sensors*, vol. 21, fasc. 21, p. 7161, ott. 2021, doi: 10.3390/s21217161.

[25] D. Laidig, P. Müller, e T. Seel, «Automatic anatomical calibration for IMU-based elbow angle measurement in disturbed magnetic fields», *Current Directions in Biomedical Engineering*, vol. 3, fasc. 2, pp. 167–170, set. 2017, doi: 10.1515/cdbme-2017-0035.

[26] J. Lebleu, T. Gosseye, C. Detrembleur, P. Mahaudens, O. Cartiaux, e M. Penta, «Lower Limb Kinematics Using Inertial Sensors during Locomotion: Accuracy and Reproducibility of Joint Angle Calculations with Different Sensor-to-Segment Calibrations», *Sensors*, vol. 20, fasc. 3, p. 715, gen. 2020, doi: 10.3390/s20030715.

[27] A. Cappozzo, F. Catani, U. Della Croce, e A. Leardini, «Position and orientation in space of bones during movement: anatomical frame definition and determination», *Clinical Biomechanics*, vol. 10, fasc. 4, pp. 171–178, giu. 1995, doi: 10.1016/0268-0033(95)91394-T.

[28] M. Benedetti, F. Catani, A. Leardini, E. Pignotti, e S. Giannini, «Data management in gait analysis for clinical applications», *Clinical Biomechanics*, vol. 13, fasc. 3, pp. 204–215, apr. 1998, doi: 10.1016/S0268-0033(97)00041-7.

[29] M. Nazarahari e H. Rouhani, «Semi-Automatic Sensor-to-Body Calibration of Inertial Sensors on Lower Limb Using Gait Recording», *IEEE Sensors J.*, vol. 19, fasc. 24, pp. 12465–12474, dic. 2019, doi: 10.1109/JSEN.2019.2939981.

[30] B. Fasel, J. Spörri, P. Schütz, S. Lorenzetti, e K. Aminian, «Validation of functional calibration and strap-down joint drift correction for computing 3D joint angles of knee, hip, and trunk in alpine skiing», *PLoS ONE*, vol. 12, fasc. 7, p. e0181446, lug. 2017, doi: 10.1371/journal.pone.0181446.

[31] S. Cordillet, N. Bideau, B. Bideau, e G. Nicolas, «Estimation of 3D Knee Joint Angles during Cycling Using Inertial Sensors: Accuracy of a Novel Sensor-to-Segment Calibration Procedure Based on Pedaling Motion», *Sensors*, vol. 19, fasc. 11, p. 2474, mag. 2019, doi: 10.3390/s19112474.

[32] I. Poitras *et al.*, «Validity and Reliability of Wearable Sensors for Joint Angle Estimation: A Systematic Review», *Sensors*, vol. 19, fasc. 7, p. 1555, mar. 2019, doi: 10.3390/s19071555.

[33] B. Bouvier, S. Duprey, L. Claudon, R. Dumas, e A. Savescu, «Upper Limb Kinematics Using Inertial and Magnetic Sensors: Comparison of Sensor-to-Segment Calibrations», *Sensors*, vol. 15, fasc. 8, pp. 18813–18833, lug. 2015, doi: 10.3390/s150818813.

[34] X. Robert-Lachaine, H. Mecheri, C. Larue, e A. Plamondon, «Accuracy and repeatability of single-pose calibration of inertial measurement units for whole-body motion analysis», *Gait & Posture*, vol. 54, pp. 80–86, mag. 2017, doi: 10.1016/j.gaitpost.2017.02.029.

[35] F. L. Markley, Y. Cheng, J. L. Crassidis, e Y. Oshman, «Averaging Quaternions», *Journal of Guidance, Control, and Dynamics*, vol. 30, fasc. 4, pp. 1193–1197, lug. 2007, doi: 10.2514/1.28949.

Chapter 3

Ergonomic assessments

The European Agency for Safety and Health at Work (EU-OSHA) reported in 2019 [1] that roughly three out of every five workers in the EU-20 complain about musculoskeletal disorders (MSD). These are issues of muscles, joints, tendons, ligaments, nerves, cartilage, bones, and localized blood circulation systems. Work-related MSDs are caused or aggravated primarily by working conditions and environments. In 2015 the most common types of MSD were backache (43%) and muscular pain in the shoulder, neck, and upper limbs (41%). These cumulative disorders could be due to physical and biomechanical factors, organizational and psychological aspects, or individual and personal characteristics. Among all, excessive force application, awkward positions, heavy physical and repetitive work, lifting, or exposure to high and continuous vibrations or too-low temperatures are the most impactful on workers' health.

The effects of these aspects on the human body and how to contrast their outbreak are studied by ergonomics, the science that aspires to achieve safe, productive, effective and interactive systems of people, machines, environments, and devices, with a human-centered perspective. Ergonomics gathers standardized approaches and procedures for improving the performance of human-machine interactions, redesigning the human workplace, and diminishing MSD.

Wearable devices, if worn by the workers, could measure various physiological and kinematic parameters and monitor human movements and vital signs, thus improving physical well-being, reducing work-related injuries, and increasing work efficiency. A direct measurement method based on wearable IMUs systems allows the analysis in outdoor and unstructured environments. IMUs represent promising instruments for industrial safety ergonomic assessments for their high flexibility, portability, low dimension, low power consumption, and usability in complex scenarios. As mentioned in the previous chapter, MoCap IMU systems, allowing kinematics studies, are a powerful tool for determining in real-time the exposure of awkward positions and repetitive movements, which is one of the more impactful risk factors for MSD onset.

Another influential risk factors are physical loads. The most common approach in biomechanics for estimating muscle loads uses offline optimization techniques that resolve the kinematic and dynamic problem of validated musculoskeletal models. Software often utilized for biomechanical studies and ergonomics evaluation are OpenSim [2] and Anybody Modelling System (AMS)[3]. The motion data and external forces of a specific task are recorded and imported into the software environment, which estimates joint angles and muscle effort. After a software selection, AMS is designated among the two for its extensive shoulder, back, and upper arm musculoskeletal models, which are fundamental for precise ergonomic assessment in working scenarios. In the last few years, several researchers have used AMS for risk assessment in lifting loads in the supermarket sector [4], in construction manufacturing [5], and in assembly lines [6], [7], but no one performed an ergonomics analysis with robotic-aided systems of working tasks. Several studies with AMS regard physical interaction between humans and the exoskeletons, but no investigations evaluate physical interaction between humans and a serial collaborative robot, namely a cobot. Thus, this chapter describes a complete study of the physical human-cobot interaction during an industrial task with AMS. In particular, the advantages of using a cobot as an assisted device for repetitive drilling tasks are quantified by comparing the OCRA index, an ergonomic parameter that considers the motion range and the muscle effort and fatigue of shoulder, elbow, and wrist muscles. Thus, a novel methodology to exploit the AMS characteristics for completing a full ergonomics OCRA analysis for defining the best strategy to release workers by excessive efforts is defined.

However, using specific musculoskeletal software makes online ergonomics assessment impossible because it requires time to be settled and performed. Thus, we develop a simple biomechanical model able to estimate in real-time (100 Hz) the upper limbs' joints wrench by force exerted over the hand using a Newton-Euler approach. The model is tested and validated with the AMS output in the drilling-aided collaborative task. The idea is to study the feasibility and accuracy of a system made of IMUs and force sensors to determine in real-time ergonomics risk factors and warn the worker in dangerous or excessive load situations. Finally, a subject-specific and reduced biomechanical model definition is proposed.

This chapter comprehends five sections: the first one contains an extensive literature review on using IMU MoCap systems for ergonomics assessment, while in the second one, the characteristics of AMS are detailed. The third section describes the study and the experiments of the physical-human interaction, whereas the fourth section details the online wrenches estimation and ergonomics indices using IMU MoCap systems. Finally, a brief description of the ongoing work on defining a subject-specific and reduced biomechanical model for ergonomics assessments characterizes the fifth section.

3.1 Ergonomic methods for work-related musculoskeletal disorders

Ergonomics at work is of fundamental interest among researchers, public health systems, associations, and institutions for its impact on workers’ health and, consequently, on economic and social issues. An accurate analysis of workers’ exposure to dangerous factors is a preventive contribution to developing a safer working environment and reducing work-related MSD. It is fundamental to ergonomists, occupational health physicians, employee representatives, and regulating authorities to have robust, accurate, and reliable methods as the basis for risk and reduction programs. Thus, several approaches have been proposed in the literature in the last few years. These methods can be categorized under three big categories [8]:

Self-reports, including interviews and questionnaires to the workers for analysing the physical and psychosocial factors. It is proven that the accuracy in quantifying the duration or frequency of assuming specific postures is imprecise and unreliable [9], [10]. Similarly, workers show difficulties in assessing the correct weight of loads or amplitude of forces, tending to underestimate it. More accurate estimations occur with office workers [11]. Furthermore, difficulties with self-reports may arise from the varying level of comprehension and education of the workers, who could mislead or misunderstands the questions. Thus, multiple methods are needed to assess a precise ergonomics analysis.

Observational methods, where an external observer assesses postural and other critical factors, gathering the results on sheets. The considered physical factors differ among different procedures [12], which primarily evaluate the posture of upper limbs. This method is relatively low-cost and practical for use in several workplaces where more invasive techniques with additional sensors would not work. However, it suffers from intra- and inter-observer variability in risk factors assessment. More recently, ergonomists used video recording to improve posture analysis during the working shift, and researchers developed automatic video algorithms for detecting posture risk factors [13], [14] and excessive repetition [15], [16].

Direct methods, where sensors attached to the worker measure risk factors. It includes approaches based on optical MoCap systems, such as Microsoft Kinect depth cameras [17], [18] or markers-based optoelectronic hardware [19]. The kinematic data are integrated into specific software that assesses ergonomics risk factors. However, optical MoCap systems suffer from occlusions and light interferences. Thus other methods rely on inclinometer sensors [20], or flexible goniometers [21], [22] for upper limbs and trunk posture analysis. Nevertheless, these systems detect motion mostly on one plane and cannot measure the angles in both directions. Others use electromyography analysis (EMG) to estimate the muscle effort during assembly works [23], and integrate this system with kinematic sensors, thus to compute simultaneously posture and force risk factors [24], [25]. Despite the high development of EMG sensors, their signals are still noisy and require high resources in terms of equipment, competence, and set-up time. Moreover, IMU MoCap systems have been widely studied in the last decade since they efficiently perform a posture analysis and are easily integrable with other sensors for force studies. Therefore, direct measurements of the workers' conditions are the most effective method, especially with the widespread growth of lightweight and precise electronic sensors.

Specifically, a literature review of 2021 [26] identified twelve works based on IMUs for ergonomics analysis. Most of them rely on the ISO 11228 Standards[27]–

[29], the ergonomics guidelines for manual handling risk assessments. The latter consist of three parts, one specifically for lifting and carrying objects with a mass of 3 Kg or more (part 1), one for a standing pushing and pulling task applied by the two hands (part 2), and one for the handling of low loads at high frequency (part 3). Part 1 refers principally to the revised NIOSH lifting equation [30], which estimates the Lifting Index (LI) by dividing the load weight of a specific task by the recommended weight limit. This limit considers several factors: the horizontal and vertical distance of the lifted weight respecting the middle ankle point, the asymmetry of the lifting motion outside the mid-sagittal plane, the motion frequency, and the hands' coupling with the weight to be lifted. Part 2 relies on Snook & Ciriello’s force limits [31], which identify the maximum static strength exertions including age, gender, and stature. This value is then adjusted according to the distance and the frequency of pushing and pulling tasks. Part 3 accounts for several procedures for the risk assessment of repetitive movements and efforts of the upper limbs. For example, OWAS [32], RULA [33] and REBA [34] primary rely on posture analysis, whereas Strain Index (SI) [35] and QEC [36] consider other risk factors such as forces, duration of exertion and speed of work. Among all, the completest method is considered the OCRA index [37] because it takes into account posture, force, repetitiveness, the duration of repetitive tasks, and recovery time during a working shift.

The usage of MoCap IMU systems in ergonomics study is relatively recent, and Table 1 gathers, as far as we know, all the works whose aim is to use IMUs, both alone and in combination with other sensors, for working ergonomic evaluations. Among all the reviewed papers, only the work of Peppoloni et all. and Giannini et all. consider, besides the human kinematic evaluation of postures that is easily implementable with IMU sensors, also force factors. They measure the level of human effort and loads exerted on one human arm with offline analysis of EMG signals. The latter directly measures the muscle action potential which is transformed, through empirical models, into muscle tension first and ergonomics factors second. However, EMGs are often cumbersome, with procedures computationally expensive and difficult to use in real time. Moreover, no one performed a complete analysis of the OCRA index because of Lenzi et all. evaluate only the posture factors.

Table 7 Ergonomics studies with IMU MoCap systems

Study	**Hardware**	**Body part**	**Risk Factor**	**Test set-up**
Caputo et al. [38]	4 IMUs	Pelvis, trunk, arm, forearm (right)	EAWS [39] - posture	4-subject test in FCA plant assembly line
Conforti et al. [40], [41]	8 IMUs	Lower limbs, trunk	Classification of correct lifting movements	26-subject laboratory test to train machine learning algorithms
Giannini et al. [42]	17 IMUs and 2 EMG	Full body	NIOSH, Snook & Ciriello, REBA, SI	2-subject test of lift-on/lift-off of containers on a cargo ship
Lenzi et al. [43]	7 IMUs	Pelvis, arm, Forearm, Hands,	OCRA (only posture term)	7 test of real low-loads repetitive task
Lins et al. [44]	15 IMUs and vibrotactile interface	Full body without hands	OWAS	Lab test for vibrotactile interface to warn the workers in case of awkward postures
Melter et al. [45]	4 IMUs	Pelvis, trunk, arm, forearm (right)	RULA	53-surgeons test of surgical operations
Peppoloni et al. [46], [47]	4 IMUs and 8 channel EMG	Pelvis, trunk, arm, forearm (right)	RULA, SI (real-time)	1-subject test of grocery cashier activity
Sedighi et al [48]	4 IMUs and a heart rate monitor	Pelvis, trunk, arm, forearm	Physical fatigue	8-subject lab simulated manufacturing tasks
Valero et al. [49]	8 IMUs	Upper and lower back, arms, thighs, legs	Posture and productivity score	6-subjects test of bricklaying apprentices
Yan et al. [50]	2 IMUs	Back and head	Head posture	1 subject lab test working simulation

Lu et al. [51]	5 IMUs	Wrist, arm, forearm, back, thigh (right)	NIOSH	1 subject lab lifting tasks
Kim et al. [52]	17 IMUs	Total body	Study of lifting task	14 subject lab test of simulated material handling tasks

Thus, the novelty of our work is to calculate the complete OCRA index in a collaborative task. The kinematic is measured by a wearable system made of 17 IMUs, and the force exerted on the hands is measured by a 6-axis torque and force sensor placed on the end-effector (EE) of the cobot. The study is performed using the AMS software and a custom-made model that estimates the OCRA index.

3.1.1 OCRA index

The OCRA (Occupational Repetitive Action) index evaluates the effect of repeated actions and checks if the working procedure and shift subdivision are admissible. It performs a detailed analysis of all the main mechanical and organizational factors that may cause musculoskeletal overload risks for the operator's upper limbs. It is equal to the ratio between the number of Actual Technical Actions (ATA) carried out during a work shift and the number of Reference Technical Actions (RTA) for each upper limb [29]:

$$OCRA\ index = \frac{n_{ATA}}{n_{RTA}} \tag{1}$$

A technical action (TA) is defined as an elementary manual action required to complete the operation within a cycle (i.e. push, pull, grasp, reach). Defining the cycle time t_c as the time required to complete the total number of technical actions n_{TC}, the n_{ATA} in a working day (t) is equal to:

$$n_{ATA} = n_{TC} \cdot \frac{60}{t_c} \cdot t \tag{2}$$

The n_{RTA} is calculated by:

$$n_{RTA} = \sum_{j=1}^{n} \left[k_f \left(F_{Mj} \cdot P_{Mj} \cdot R_{eMj} \cdot A_{Mj} \right) \cdot\ t_j \right] \cdot \left(R_{cM} \cdot t_M \right) \tag{3}$$

where:

- n is the number of repetitive tasks during a shift.

- k_f is the constant of the frequency of technical actions per minute, usually equal to 30.
- F_M is the force multiplier that depends on the percentage of maximum contraction measured with EMG or the ratio between the force exerted and the force limit defined in [53].
- P_M is the posture multiplier determined by the percentage of time on which shoulder, elbow, and wrist joints angles exceed angle limits, listed in Table 2.
- R_{eM} is the repetitiveness multiplier in each task. If the same TA lasts for at least 50% of the cycle time or if the cycle time is shorter than 15 s, it equals 0.7. Otherwise, it is equal to 1.
- A_{Mj} evaluates the presence of additional factors such as vibrating tools, the requirement for absolute accuracy, the localized compression of anatomical structures, exposure to cold surfaces and environments, use of gloves, etc. It can assume four different values.
- t_j is the net duration, in minutes, of each *j-th* repetitive task.
- R_{cM} is the recovery multiplier and is the risk factor due to the lack of recovery periods.
- t_M is the duration multiplier and depends on the total duration of the repetitive task during a complete working shift.

Table 8 *Posture multiplier* $\mathbf{P}_M$ *for awkward postures [29]*

Awkward posture and/or movements		Portion of cycle time			
		1% - 24%	25% - 50%	51% - 80%	> 80%
Elbow	Supination (≥ 60°)	1	0.7	0.6	0.5
Wrist	Extension (≥45°) Flexion (≥45°)				
Hand	Hook grip or palmar grip (wide span)				
Elbow	Pronation (≥ 60°) Flexion/extension (≥ 60°)		1	0.7	0.6
Wrist	Radio/Ulnar deviation (≥ 20°)				
Hand	Pinch				

Thus, for each TA the values of force, posture, repetitiveness, and additional factors are determined and multiplied for their duration. The sum of all the obtained values determines the OCRA index, which indicates the workplace level of risk. A value ≤ 2.2 indicates no risk, whereas a value within 2.3 – 3.5 implies low risk, and improvements are necessary to reduce it. If the value is > 3.5, the risk is high, and the working tasks have to be modified to be more ergonomic.

Among all the factors, the force multiplier, F_M, is the less straightforward. Some ergonomists propose using EMG electrodes that directly estimate the muscle activation of each muscle. The amplitude of EMG signals can provide some insight measure of the muscle force, even if the direct relationship between the two is complicated by the fact that factors such as type of muscle fiber, muscle length, and muscle velocity can all influence the relationship between the electrical and mechanical activity of the muscle. Moreover, this method is noisy, expensive, and with a bulky setup. Thus, the standards propose two different procedures: a biomechanical approach based on a statistical strength distribution and the CR-10 Borg scale [54], a quantitative measure of perceived exertion during physical activity in questionnaire forms to the workers. The validity of using this scale increases with the number of workers interviewed. However, since the self-report responses tend to underestimate the effective force exercised [9], a more scientific and experimental approach is preferred. The statistical analysis described in [53] is a European Standard for determining the force limit for machinery operation. The maximal force is the maximal force-generating capacity of the user. It is determined for relevant actions within specified intended user populations that consider an equal representation of males and females. As a safer approximation, the distribution parameters belong to the female reference groups. Limits are referred for specific activities for the adult European working population and get closer to reality by changing over the logarithmic normal distribution, with:

$$\overline{F_{ln}} = \ln \overline{F} \tag{4}$$

$$\sigma_{ln} = \ln \frac{\overline{F} + \sigma}{\overline{F}} \tag{5}$$

where $\overline{F}$ and σ are the specific distribution parameters for the adult female population of specific working activity listed in [53]. For professional use, the maximal isometric force F_B is defined as the 15% percentile of the maximum force $\overline{F_{ln}}$ as follows:

$$F_{ln15\%} = \overline{F_{ln}} - 0.5244 \cdot \sigma_{ln} \tag{6}$$

$$F_{15\%} = F_B = e^{F_{ln15\%}} \tag{7}$$

The so-obtained force limits allow up to 85% of the adult European working population to execute the task without exceeding their physical capacity. For the upper limbs, the maximal isometric force F_B of the principal working activities are listed in Table 3. The F_B values could be used to estimate the force multiplier: if the force that solicits the workers during a specific task is known, the ratio between the measured value and the F_B defines a percentage of loading that estimates the force multiplier. Moreover, these values are necessary to determine the maximal admissible joint torque, Section 3.4.1, for the online estimation of the OCRA index.

Another solution to estimate the muscle effort is by simulating the working scenario with validated commercial musculoskeletal models. The external load applied to the worker can be modelized or imported by experimental measurements. The musculoskeletal model, scaled according to the workers' anthropometric measures, simulates the muscle effort, and determines the force multiplier of the OCRA index analysis.

Table 9 *Maximal isometric force* $\boldsymbol{F_B}$ *defined from the mean force* $\boldsymbol{\bar{F}}$ *and the specific distribution parameter* $\boldsymbol{\sigma}$ *for adult female population [53]*

Activity		$\bar{F}\ [N]$	$\sigma\ [N]$	$F_B\ [N]$
Hand work	Power Grip	278,00	62,20	250
Arm work: sitting posture	Upwards	58,00	18,40	50
	Downwards	88,60	33,20	75
	Outwards	65,50	26,20	55
	Inwards	85,60	24,60	75
	Pushing W trunk support	312,00	84,40	275
	Pushing W/O trunk support	78,00	42,70	62
	Pulling W trunk support	246,00	45,70	225
	Pulling W/O trunk support	67,90	33,50	55
Whole body work	Pushing	233,70	81,00	200
	Pulling	164,60	44,90	145

3.2 Multibody software for ergonomics

Musculoskeletal multibody software allows kinematic and dynamic human motion analysis by providing postures, joint loads, and muscle forces activity estimation. Both AMS and Opensim include complete and detailed musculoskeletal models and associated algorithms for simulating the human body working in concert with its environments. However, the body coordinate systems, algorithms, and modelling assumptions vary between the two systems. Firstly, Opensim scales the anthropometric measurements with static trials: segments are scaled separately along the principal axis to fit the joint centres and in the perpendicular plane to make experimental landmarks points coincident. Conversely, Anybody performs dynamic calibrations, and the segments are firstly scaled in the longitudinal dimension to match the markers' position and then scaled in width to obtain the specific mass property, estimated with length-mass scaling approaches [55]. While the theoretical approach of the kinematics and dynamics algorithms are the same for the two software, the musculoskeletal models differ because they are derived from different anatomical studies, and so do the numbers of muscle actuators and the properties of muscle and tendons. Therefore, a methodical comparison between the two systems is difficult to assess. The works of [55], [56], compares the muscles force estimations during gait at regular and different speed. They both underline that those two approaches show similar muscle activation patterns, even if some discrepancies are present in the actual values due to differences in models’ definitions and kinematic results. Similar conclusions are derived from the study of [57] that compare the results of the two software during lower-limb simple motion with EMG data. They highlighted that force-length velocity muscle properties are different between the two environments, thus causing differences in the muscle effort estimation. However, all those studies used standard marker-based approaches as input data for kinematic analysis. This comparison is even more complex when wearable IMU sensors are the input data because the method by which the data are imported differs completely.

Opensim uses Opensense [58], a toolbox that implements IMU-based kinematic measurements. The IMU’s attitude estimation, defined in the Earth coordinate system (ECS), and the correspondent values of the sensor-to-segment calibration are imported into the software and associated with the musculoskeletal model positioned in the same initial posture of the imported data. Then, each IMU is visualized inside the environment as a small square solid with specific coordinate frame that correspond to the IMU technical reference frame (TRF). If the simulated TRF differs from the actual TRF orientation, the simulated IMU can be moved and rotated. Then, the musculoskeletal kinematics relies on minimizing the weighted-square difference of the angle that defines the relative rotation between the IMU's rotation matrix in ECS and the rotation matrix that describes the segment attitude in the virtual frame. The complete formulation is in [58]. On the contrary, the approaches for importing IMU data of AMS depend on global optimization like the one for marker-based protocol. The IMU MoCap results are transformed into a moving skeleton and imported into AMS through the BVH file. Then, several markers are attached both to the BVH file and the musculoskeletal model in meaningful anatomical points. The kinematic resolution is by a least-square optimization of the distance between the AMS model's virtual markers and the trajectory of the ones moved by the IMU Mocap algorithm. As far as we know, a complete comparison of the results obtained by these two approaches in importing IMU data is not performed, and it is unknown which is the best performing. However, this factor is not a determinant for software selection. AMS has a more detailed shoulder and upper limb musculoskeletal model among the two solutions. Since the principal work-related MSD are of the upper body, AMS is chosen as the preferred multibody software for ergonomics assessment.

3.2.1 Anybody Modelling Repository

AMS is flexible and easily programmable: the Anybody Model Repository (AMMR) [55] is an open library of musculoskeletal models configurable in multiple ways, including different and partial limb segments, types of muscles, human scaling, and several recruitment solvers. Each body part is implemented from detailed cadaver/anatomy studies, ensuring high accuracy and anatomical fidelity. Originally the entire body model was developed at Aalborg University (Denmark), subsequently being updated with different body part models validated in other laboratories. In particular, the shoulder and arm models come from the Dutch Shoulder Group of the TU Delft University and contain data from two persons. The full-musculoskeletal body model is used for the ergonomics study assessment of upper limbs. It includes 947 muscle elements, and 80 degrees of freedom (DOF), subdivided in:

- 2x 3 DOF at the ankle joints

- 2x 1 DOF at knee joints
- 2x 3 DOF at hip joints
- 6 DOF at the pelvis
- 3 DOF between thorax and pelvis
- 12x 3 DOF for the cervical, thoracic, and lumbar spine
- 2x 3 DOF at the glenohumeral joints
- 2x 2 DOF at the elbow joints
- 2x 3 DOF at the sternoclavicular joints
- 2x 2 DOF at the wrist joints
- 1 DOF at the neck joints

The shoulder and arm model includes 20 and 10 muscle elements respectively, subdivided into several muscle bands positioned at various points with different lines of action. The musculoskeletal geometric and inertial parameters are firstly scaled to the subject by applying a length-mass-fat scaling law with the human's total mass and height as input. Secondly, another calibration procedure that considers the position of experimental markers in anatomical points can update the first estimation of anthropometric parameters. AMS models are driven by marker-based or markerless motion tracking systems using specific integration protocols, which are modifiable according to the type, number, and positions of markers used.

The AMS has four muscle model classes differing in complexity and accuracy of their representation of physiological muscles. However, higher complexity traduces on higher numbers of parameters to set up during the musculoskeletal model calibration and elevated computational costs during the analysis. The simplest model considers only the muscle’s isometric strength, that is its force in a static condition at its optimal length. This formalization, called AnyMuscleModel, works reasonably well with moderate contraction velocity and little joint angle variations since the muscle strengths do not depend on the muscle’s current length and contraction velocity. However, small and low motions are not typical of working scenarios, thus the full-blown Hill-type muscle models or three-element model [59] is preferred. Figure 1 shows a schematic representation of the muscle of AnyMuscleModel3E library. It considers three components: a contractile element (CE), representing the active properties of the muscle fibre, and two non-linear spring elements, one in series (T), which defines the elasticity of the tendon, and one parallel (PE) characterizing the passive stiffness of the muscle fibres.

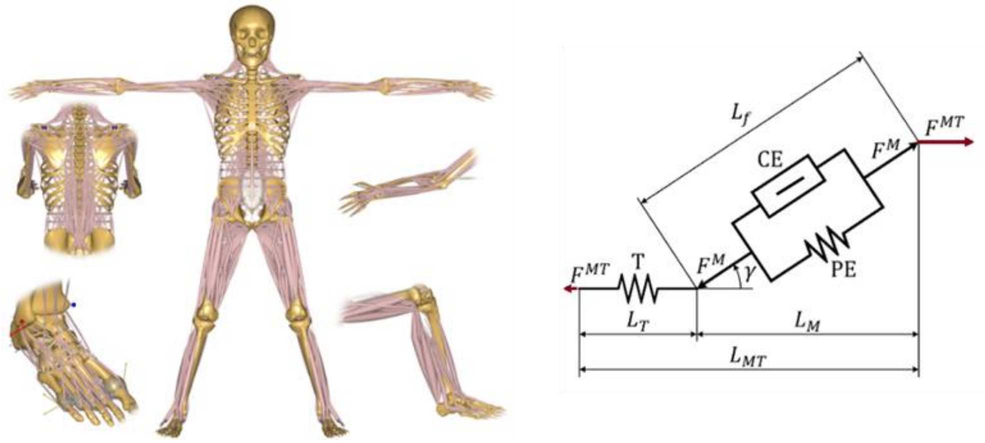

__Figure 1__ Left: details of the AMMR model, right: schematic representation of three-elements Hill-type muscle-tendon unit

Muscles are a collection of equal fibres in parallel orientated either in the direction of the tendon or at an acute angle. This angle is called pennation angle *γ*, and its value changes when the muscle extends or contracts. Referring to the Figure 1, the L_{MT} is the total length of the muscle element, which is equal to the sum of the tendon length L_T and the muscle fibre length L_F adjusted by pennation angle *γ*. Equally, the force in tendon F^{MT} is the force of muscle fibre F^M multiplied by the cosine of the pennation angle. Each muscle fibre is defined by ideal parameters with muscle at neutral fibre length and zero contraction velocity. In particular, F_0 is the maximal isometric muscle force, L_{f0} is the nominal muscle fibre length, L_{T0} is the nominal tendon length, and γ_0 is the nominal pennation angle.

One of the challenges in body modelling is to scale and change the size of musculoskeletal models reflecting individuals of different statures and weights. If this problem is complex for scaling the length of the body segments, it is even more problematic when calibrating muscle-tendon units. The basic idea in AMS is the assumption that each muscle-tendon fibre has its optimal length at some predefined position of the joint it spans. So, the muscle-tendon calibration procedure consists of moving the length-calibrated skeleton in those specific positions and adjusting the length of the tendons to give the attached muscles their optimal lengths in those positions. Table 4 and 5 gathers the principal muscle-tendon parameters of the shoulder and elbow fibres, scaled to a subject of 1.72 m and 62 Kg. In this case, the nominal tendon strain, which is a parameter that controls the elasticity, is equal to 0.053, and the relative amount of fast fibre is 0.4 for each muscle.

Table 10 *Muscle-tendon parameters of the shoulder group*

Shoulder Fibers Names	F_0 [N]	L_{f0} [m]	L_{t0} [m]	γ_0 [rad]
Biceps Brachi Caput breve (1)	152.24	0.15	0.1	0.0349
Biceps Brachi Caput longum (1)	157.55	0.1	0.1	0.0349
Coracobrachialis (1-6)	82.33	0.091	0.0182	0.0174
Deltoideus Posterior (1-4)	79.66	0.1155	0.02475	0
Deltoideus Lateral (1-4)	181.45	0.1155	0.02475	0
Deltoideus Anterior (1-4)	120.37	0.1405	0.02475	0
Infraspinatus (1-6)	120.55	0.065	0.0075	0
Latissimus Dorsi 1	38.41	0.14	0.021	0
Latissimus Dorsi 2	76.83	0.14	0.021	0
Latissimus Dorsi 3	98.78	0.14	0.021	0
Latissimus Dorsi 4	120.733	0.14	0.021	0
Latissimus Dorsi 5	159.148	0.14	0.021	0
Levator Scapulae (1-4)	76.14	0.1	0.02	0.087
Pectoralis Major Thoracic (1-10)	57.53	0.12	0.012	0.0872
Pectoralis Major Clavicular (1-5)	46.02	0.12	0.012	0.0872
Pectoralis Minor (1-4)	75.85	0.08	0.008	0.0872
Rhomboideus(1-3)	223.32	0.068	0.0136	0.0872
Serratus Anterior(1-6)	168.61	0.073	0.0073	0
Subscapularis (1-6)	221.284	0.08	0.04	0.0698
Supraspinatus (1-6)	69.04	0.047	0.00376	0
Teres Major (1-6)	44.25	0.1	0.01	0.0349
Teres Minor (1-6)	45.67	0.07	0.007	0.0349
Trapezius Scapular (1-6)	128.78	0.1	0.02	0.1745
Trapezius Clavicular (1-6)	128.78	0.1	0.01	0.1745

Table 11 *Muscle-tendon parameters of the elbow group*

Elbow Fibers Names	Maximal Isometric muscle force [N]	Optimal muscle fiber lenght [m]	Nominal Tendon Lenght [m]	Nominal Pennation angle
Triceps LH (1-2)	248.70	0.094	0.0329	0.523
Brachialis (1-2)	270.14	0.123	0.0185	0.261
Triceps ME (1-2)	400.56	0.087	0.01305	0.7853
Triceps LA (1-2)	212.27	0.055	0.01375	0.5235
Brach rad (1-2)	97.36	0.128	0.0192	0.2617
Anconeus (1-2)	8.1765	0.024	0.006	0.5235
Pronator teres caput humeral (1-2)	82.472	0.0665	0.0099	0.2617
Pronator teres caput ulnare (1-2)	164.94	0.0665	0.0099	0.2617
Supinator Humerus (1-2)	263.45	0.04	0.006	0.2617
Supinator Ulna (1-2)	263.45	0.04	0.006	0.2617

Once the muscles are scaled, an optimization problem estimates the force generated by each muscle. For the dynamic principles, the external forces, muscle loads and joints, and contact loads equal to balance the entire body system. Since the number of muscle fibres is physiologically higher than the model's DOF, a muscle recruitment criterion is necessary to resolve the muscle redundancy and accurately determine which set of muscles balances the external loads. In skilled movements, the central nervous system recruits the muscle systematically, choosing the muscles to activate. Remembering that muscles are unilateral elements that can only pull and push, the mathematical formalization has to be constrained to have solutions with positive or zero muscle forces. Thus, the problem consists of finding the muscle force by minimizing the dynamic equation that equals all the muscle and joint forces $\boldsymbol{f}^{(M)}$ to the external and inertia forces ($\boldsymbol{r}$):

$$\begin{gathered}\min G\left(\boldsymbol{f}^{(M)}\right) \\ subject\ to: \quad \boldsymbol{C}\boldsymbol{f}^{(M)} = \boldsymbol{r}\,, \ \ f_i^{(M)} \geq 0, i = 1, \dots, n^{(M)}\end{gathered} \tag{8}$$

where $\boldsymbol{C}$ is the weight matrix of muscle activation that regulates how much a specific muscle is responsible of the total force, and $G\left(\boldsymbol{f}^{(M)}\right)$ is the function of muscle force recruitments, which varies accordingly to the strategy adopted. The simplest is linear muscle recruitment, where the cost function is the sum of each muscle force normalized by its maximal strength. This approach is not physiological because the minimization tends to activate muscles with higher strength and leave unused muscles with lower power values. It is more plausible that the nervous system actives the higher number of muscles to reduce the strength of each fiber. The polynomial muscle recruitment guarantees higher synergies between muscle activations:

$$G = \sum_{i=1}^{n^{(M)}} \left(\frac{f_i^{(M)}}{F_{0i}} \right)^p \tag{9}$$

where p indicates the exponents of the function, which is necessary to penalize larger terms in the sum and active muscle more uniformly. Usually, a muscle criterion of high polynomial order (p>2) guarantees a higher level of synergism to balance the external loads, thus having the maximum activity of any muscles as small as possible. This criterion physiologically means that the entire system tends to reduce the fatigue of the muscles, maximizing its endurance, and it is considered the most suited for ergonomics evaluation.

3.2.2 Force multiplier definition in Anybody

As mentioned in Section 3.1.1, ISO 11228 suggests using surface electromyography analysis for determining the force multiplier and the muscle overloads. The EMG signal is normalized to the muscle's maximum voluntary contraction (MVC) which is the maximum voluntary force possible under dynamic or isometric muscle action conditions, limited by muscle fiber recruitment and frequency of action potentials. It is measured with EMG sensors imposing a static pose with known loads on the muscles. Thus, the MVC is equivalent to the maximal isometric muscle force F_0 defined in AMS. For calculating the force multiplier for OCRA evaluation, it is admissible to substitute the %MVC, defined as the ratio between the EMG data and MVC, with the proportion of the AMS i-th muscle force ($f_i^{(M)}$) exerted in a specific task and the maximal isometric strength. This value, called muscle Activity (A), is automatically calculated within AMS. In this context, referring to the process of calculating the OCRA force multiplier F_M as per ISO 11228-3, the %MVC can be substituted by the worst muscles activity A_J of a specific joint calculated from AMS values as:

$$\overline{\%MVC} = \frac{1}{T}\sum_{j=1}^{n} \varDelta t_j \cdot \max(A_J) * 100 \tag{10}$$

where T is the cycle time and $\varDelta t_j$ is the duration of exposure to a specific technical action. Table 6 lists the corresponding force multiplier of specific values of $\%MVC$ and Borg scale.

The ergonomics assessment workflow proposed using AMS is simple and easily automatized. The worker motion can be captured by a MoCap system (optical or inertial) and imported into the simulation environment with a protocol specific to the technology. The forces exerted on the worker can be measured with force and torque sensors or simulated directly inside the modelling environment. Finally, AMS can resolve the kinematics and the dynamics obtaining the angle joint and the muscle effort for calculating the posture and force multiplier. Validated musculoskeletal models for studying the workers' safety is a valuable tool for designing a safer working environment, reducing muscle stress and overloads, and hopefully preventing work-related MSD. This tool can support ergonomists in methodical estimation and prevention of dangerous situations in the modern working industrial workflow.

Table 12 *Force multiplier* $\boldsymbol{F_M}$ *for awkward postures [29]*

Force level % of MVC, or F_B	5	10	20	30	40	≥ 50
CR-10 Borg score	0.5 very, very weak	1 very weak	2 weak	3 moderate	4 somewhat strong	≥ 5 strong/ very strong
Force multiplier, F_M	1	0.85	0.65	0.35	0.2	0.01
These values can be interpolated if intermediate results are obtained						

3.3 Study of the physical human-robot interaction with AMS

The study of the physical human-robot interaction is gaining increasing attention due to the widespread of the robotic system as assistive devices in machinery and highly industrial automation companies, rehabilitation sectors, and surgical applications. One of the protagonists of the industry 4.0 revolution is the collaborative robot, namely the cobot. There are many collaborative robot applications across all industries, including assembly, dispensing, finishing, machine tending, material handling, welding and removal, quality inspection, etc. In these scenarios, cobots work in conjunction with humans by releasing the worker of excessive loads or executing tasks that are too repetitive or energy dispendious. Even if the trend of using collaborative robotics in the industry is fast-growing, the number of systematic studies that estimate their beneficial effects on industries is few. Musculoskeletal modelling simulation can estimate the interaction forces between humans and robots and be a complete tool for designing and planning safer interaction activities. Several studies regard the physical interaction between humans and exoskeletons [60]–[64], but, as far as we know, no one simulated the physical interaction between humans and cobots during a working task.

Manual drilling still prevails in assembly, maintenance, repair, and surgical tasks. The operation parameters diversity, such as material, number of holes, distance, location, and hole orientations require a highly flexible robotic system, able to collaborate with the worker. Cobots represent a promising solution. Using collaborative robotics systems could help the workers by releasing the load, avoiding awkward postures, and reducing the overloads of the musculoskeletal system. Thus, in collaboration with the SAIMA laboratory of the University of Bologna, a cobot application is designed to help the workers in the drilling operation.

This work aims to estimate the beneficial effect of using a cobot as an assistance device for drilling operations by estimating the OCRA index. In particular, the physical human-robot interaction is simulated into AMS and used to verify the validity of different controlling strategies implemented.

3.3.1 Collaborative robotics scenario

The human-robot collaborative scenario consists of using a hand-guiding cobot for reducing the worker's effort on drilling operation. It consists of the Franka Emika Panda (FRANKA EMIKA GmbH, Munich, GER), a lightweight 7-DOF collaborative robot. It consists of seven brushless DC motor and harmonic drive gears equipped with torque and encoder sensors. The end-effector is customized with a commercial drill fixed with a plastic and metallic structure. The Schunk FT-AXIA 80 EtherCat sensor (SCHUNK GmbH & Co), mounted between the end-effector and the hand manoeuvre, measures the interaction forces. It is 6-axis sensors that estimate forces and torque on its sensible side plate thanks to internal strain gauges. The worker's motion is measured with the Shadow MoCap suit. Figure 2 is a schematic representation of the described collaborative scenario.

Similar to the approach in [65], the robot is hand-guided with the admittance control that smoothly regulates the robot's velocity in response to the force applied to the end-effector by the human. The human guides the end-effector to the hole location and performs the task in two different modalities: 1) in the first mode, defined w/o helping, the torque command in joint space compensates only the robot gravity and joint friction, thus the workers perform the drilling without sensing weight but has to push in the hole direction, whereas in 2), named w/helping, a velocity controller moves the end-effector in the hole direction and helps the worker performing the drilling operation. The velocity controller is

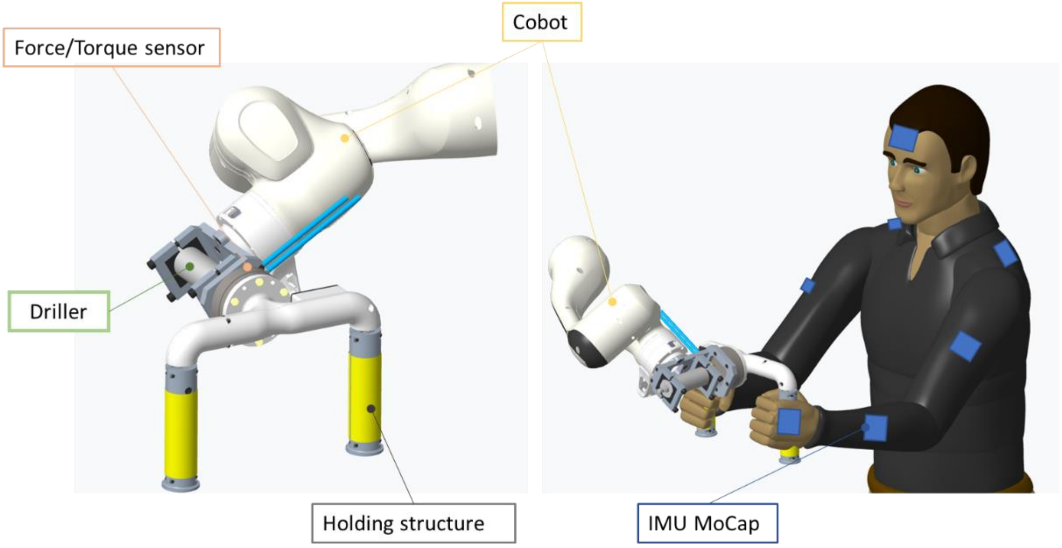

Figure 2 Representation of the collaborative robotics scenario set-up

activated manually when the driller is in the desired position. The worker directs the driller in the path of the drilling hole, which is saved to force the robot end effector to sweep in that direction with a specific velocity.

The two cobot modalities are tested with the same procedure consisting of performing four holes in precise locations of a piece of wood: the first one is on a plane perpendicular to the ground, while the last three are on a plane parallel to the ground, at the height of approximately 1 m. Different drilling positions simulate a real working scenario for testing a variety of configurations of the upper limbs. Table 7 shows the technical actions subdivision following the OCRA procedure for the left and right upper limbs. As mentioned in Section 3.1.1, the OCRA index depends on the duration and the number of repetitions of the same task, external factors such as noises or temperature, the number of breaks and recovery, and the posture and force multiplier. Supposing that the working operations in all the analysed cases, have to be finished at the same time, with the same cycle works and repetitions, and that the worker is subjected to the same external factors, the difference between the OCRA indexes in the two cases depends only on the value of the force and postures factors, which are the workers' postures and muscle efforts during the drilling task. Both these terms are estimated using AMS.

Table 13 *Technical actions subdivision of the drilling operation*

	Technical Actions	
	Left Upper Limb	**Right Upper Limb**
	Grasp drill	Grasp drill
	Place on 1st hole	Place on 1st hole
	-	Operate by pressing button
	Push to make 1st hole	Push to make 1st hole
	Place on 2nd hole	Place on 2nd hole
	-	Operate by pressing button
	Push to make 2nd hole	Push to make 2nd hole
	Place on 3rd hole	Place on 3rd hole
	-	Operate by pressing button
	Push to make 3rd hole	Push to make 3rd hole
	Place on 4th hole	Place on 4th hole
	-	Operate by pressing button
	Push to make 4th hole	Push to make 4th hole
Total number of technical actions, n_{TC}	9	13
Cycle time, t_C, s	40	40
Frequency, f, TA/min	13.5	19.5

3.3.2 Material and methods

The results of the collaborative tasks are compared with the ones obtained with a standard drilling process to estimate the beneficial effects of using cobots in manual industrial operations. A man subject (height = 1.72 m, weight = 62 Kg) wears the Shadow MoCap suit that records the motion during the three tests. The standard drilling operation is performed outdoors, and the kinematic is also measured by an optoelectronic Vicon system consisting of 6 Bonita and 2 Vero cameras, processing data within Nexus 2.5, and keeping all system settings at default values. 42 markers are fixed over the subject body following the Plug-in-Gait (PiG) protocol, fully described in Section 2.3.2. Figure 3 shows the setup of the two systems.

The MoCap algorithm presented in Chapter 2 traduces the information of each IMU into meaningful kinematic output. The subject performs three static poses and the functional movements of the elbow and wrist to calibrate the IMU MoCap system. Simultaneously, the motion tracked by the Vicon system scales the musculoskeletal model inside AMS. The first estimation of the length of the upper

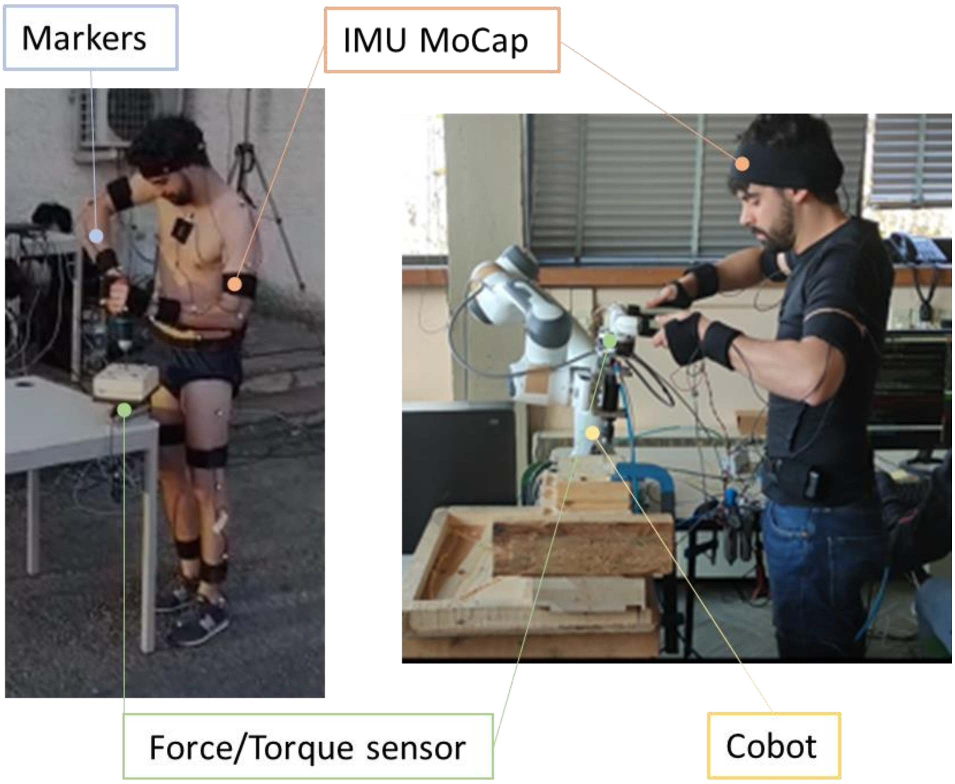

Figure 3 Experimental set-up. Left: standard drilling operation. Right: collaborative drilling task

and lower limbs and the pelvis obtained with the length mass scaling law is corrected by the position of the experimental markers. The muscle and tendon properties are scaled accordingly. The Vicon data are used uniquely for the calibration, while the IMU MoCap systems compute the subject's motion in all the experiments.

The motion tracking output determines the BVH file, which is necessary to implement the IMU signal in AMS, with an automatic code implemented in Matlab 2020a. The BVH (Biovision Hierarchy) format is an ASCII file with a hierarchical data structure representing the human skeleton, used as a standard format for biped character motion. The first part of the code contains the anthropometric length of the human body, and the second part gathers the position of the pelvis, which is set equal to the zero, and the 3 Euler angles for each joint, transformed from the correspondent joint quaternion with the ZYX convention. A custom-made protocol assigns the correspondence between the BVH and AMS musculoskeletal model, with 45 virtual markers attached to meaningful anatomical points of the two systems. Through a least-square optimization of the distance between the AMS model's virtual markers and the trajectory of the acquired data ones, the kinematics of the human model is computed, obtaining the human joint angles.

Figure 4 shows the two models and the marker's positions of the protocol implemented. The interaction forces between the human and the driller, measured in a coordinate system attached to the sensitive plate of the force/torque sensor, are imported into AMS in custom reference frames defined

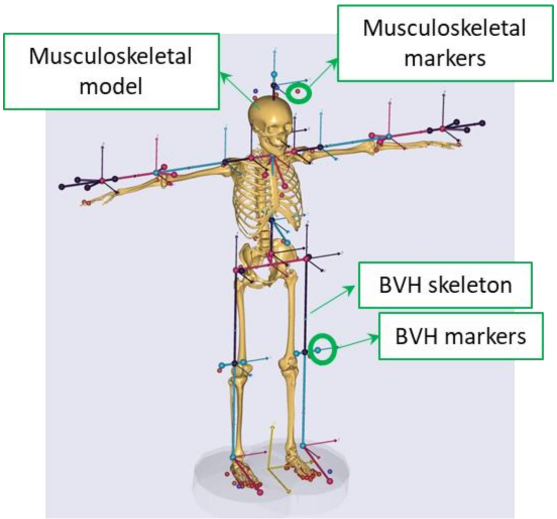

Figure 4 *IMU data implementation in AMS: BVH skeleton related to the musculoskeletal model*

in specific hand points of the AMS musculoskeletal model. The transformation matrix is easily identifiable by knowing the hand's orientation and position with respect to the sensor. In the standard drilling application, the force/torque sensor is stable in a fixed position, and its output is imported in AMS in a reference frame rigidly attached to the AMS global coordinate systems. The operator holds the driller with one hand; thus, the right arm supports the entire stress. On the contrary, during the collaborative drilling task, the torque sensor's attitude, and position change according to the end effector’s motion. The operator guides the driller with a bimanual structure that forces the hands to be symmetric to the tool. Then, the two upper arms balance and support together the interaction force. Supposing that the connection between the hand and the structure is rigid and unchanged during the experiment duration, the relative position and orientation are estimated by the structure's geometry. The corresponding transformation matrix converts the forces measured by the sensors in the hand coordinate systems, defined into AMS as a reference node in the palm hand oriented as the hand reference frame of the BVH model.

The ground reaction forces necessary to proceed with the dynamic analysis, are estimated by the GRF prediction tool of AMS, which relies on 25 conditional contacts added to the model feet that work as force actuators. They equal normal and frictional forces to balance the entire system. Mathematically, these terms are treated as muscles using muscle recruitment optimization, thus having the maximal permissible reaction values for minimizing muscle activity. For estimating muscle forces, static force optimization minimizes the polynomial muscle criterion of Eq.9 with p = 2. Despite its good prediction, the muscles sometimes present unphysiological and abrupt switch peaks when the joint moment passes from negative to positive. For this reason, a moving averaging filter (smooth(rloess), Matlab 2020a), which assigns zero weight to data outside six mean absolute deviations, is used to filter the AMS muscle activity data. To test different AMS configurations the muscles are modelled with AnyMuscleModel3E and AnyMuscleModel libraries.

The volume of the driller and the robotic system is simulated inside the AMS environments by adding the .stl files in specific locations. In the standard drilling operation, the .stl of the tool is attached to a node of the right hand, whereas the robot .stl is positioned with the base translated of a measured value from it to the human foot.

3.3.3 Results

The choice in defining the marker's position of the protocol that drives the musculoskeletal model from the BVH file is fundamental to performing a proper kinematic evaluation. The kinematic analysis of AMS may fail, usually for a worse definition of the position of the markers for resolving the global optimization process. A proprietary procedure adjusts the marker position by manually choosing their direction of movement to reduce the difference with the experimental data. Hoverer, the numbers of optimizable markers are restricted, and the procedure does not always converge to a solution. Moreover, this procedure is particularly truthful with marker-based input data because it changes the markers' position according to the position of experimental markers using several experimental data performing several movements. However, this procedure is less straightforward for the IMU MoCap system because the number of possible markers to move is doubled (both musculoskeletal and BVH ones) without target points to reach. The suggestion of the AMS developers is to modify, in a systematic and restrained way, the position of the musculoskeletal and BVH markers. However, the choice depends on the user's decision with a reiterative process that could be dispendious and ineffective. The implementation of IMU MoCap inside modelling software is a relatively new and unexplored topic. In the last years, several researchers have studied the feasibility of using IMUs data in AMS, comparing the kinematics and dynamics results with the ones obtained with the gold standard optoelectronic systems[66]–[69]. However, they all utilize the Xsens MVN Studio as IMU systems and a specific protocol for the XSens BVH output implemented inside the AMS library. They demonstrated that the prediction of joint angles and muscle activity with IMU sensors provide comparable performances of the optoelectronic system. However, that protocol is not feasible for our custom biomechanical IMU MoCap algorithms because of different anatomical reference system definitions than XSens BVH. Thus, the same approach is used but with modified marker positions, which are optimized manually with BVH files containing simple movements of upper limbs (abduction and flexion of the shoulder and elbow flexion). The markers' position is systematically changed thus to obtain a musculoskeletal model that accurately mimics the expected motion. Figure 5 shows a frame of the AMS models in the two different configurations. The overall kinematics is similar to the actual motion even if some errors are present: the hands, especially in the experiments with the

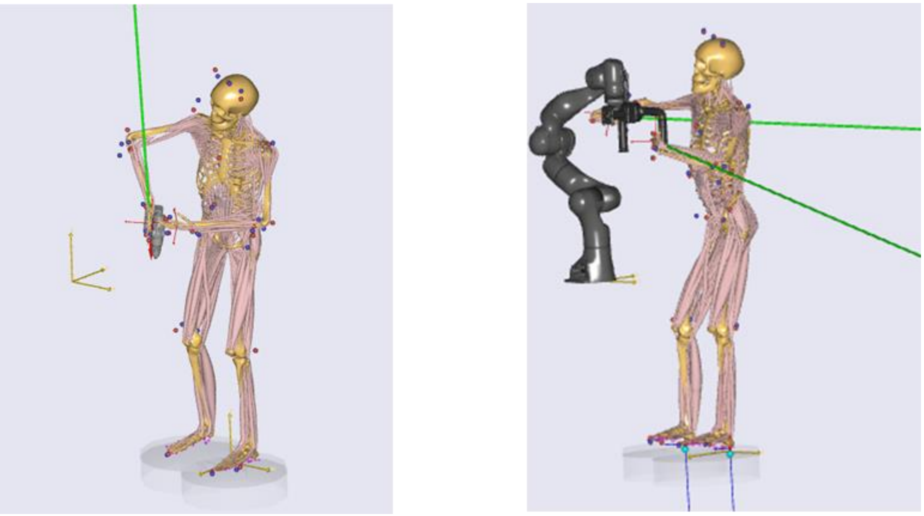

Figure 5 AMS frame of left: standard drilling, right: collaborative drilling task

robot, do not touch the driller holding structure during the complete phase of the experiments. The wrists are over-flexed, and this could be due to a lack of constraint in the wrist joints or some errors in positioning the markers over the hands. However, the overall kinematic is acceptable. During the task of standard drilling, the only joint that exceeds the limits reported in the normative is the shoulder abduction angles. Physiologically the shoulder abduction has a range of about 90°, and the imposed limit is 45°: positions higher than this value are potentially dangerous for the workers, especially if highly repeated. The latter angle remains under the limits of robotics-aided drilling operations. The operator's hands hold the handle, and no upper limbs' angles exceed the limits. In this specific scenario, the posture multiplier would assume a value within 0.7-0.6 for a standard drilling operation, whereas it is equal to 1 when the human collaborates with the robot.

It is noticeable mentioning that the subject conducting the experiments is not a manual worker nor an expert in drilling. It is not clear if a trained worker would assume the same position during standard drilling or would change its posture naturally thus reducing the load on the joints. However, cobots, specifically designed for a specific task and with an ergonomic handle structure, are helpful to conduct and force the workers' posture to maintain the correct position during repetitive tasks, especially at the end of the work shift when the fatigue advances.

The results of the dynamic studies confirm the advantages of using assistive cobot systems. Figure 6 shows the moments over the flexion axis of the right

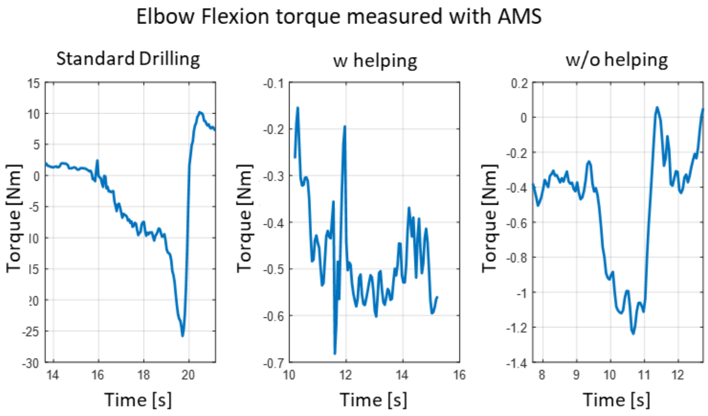

Figure 612 *Right flexion axis moments in the three cases analysed: standard drillin, w helping and w/o helping*

elbow for the three cases analyzed. For simplicity, only the phase of the actual perforation is analyzed. The elbow torque on the standard drilling reaches a peak of 25 Nm due to the load exertion necessary to make the hole. This absolute value depends on the material to proceed, the type of working equipment, and the posture of the upper limb. However, under the same working condition, this value has a maximal peak of 1.2 Nm for the collaborative task w/o helping and shows an almost constant value for the case w helping around 0.5 Nm. The results confirm what was expected: the cobot supports the workers' upper limbs by drastically reducing the load over the joints. Moreover, the w helping case smooths the torque outputs since the operator does not push because the velocity controller operates the drilling operation.

Figure 7 shows the activity of the supraspinatus 1, which is similar in terms of trends and absolute values to other muscles of the supraspinatus group. Following the procedure proposed in Section 3.2.2, the force multiplier calculation considers the maximum values of the most active muscles of each joint in a specific technical action and the ratio between the TA duration and the entire time cycle. In the standard operation, the supraspinatus is the more activated muscle for the shoulder. Figure 7 shows only the drilling technical action. The supraspinatus activity reaches 0.45 for the standard drilling, whereas it remains near zero for the two collaborative tasks. In those cases, the supraspinatus is not the most activated

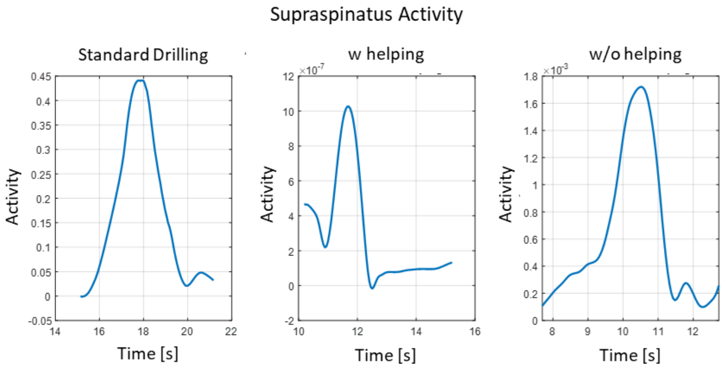

Figure 713 *Supraspinatus 1 activity estimated by AMS in three cases*

muscle, however, the other muscle activity remains under the 0.05 threshold. Supposing that the duration of the drilling task is 50% of the entire cycle time, the %MVC is equal to around 22.5 for the standard operation and less than 3 for the collaborative task. Thus, the force multiplier is respectively 0.65 and 1 for the two different cases. The cobot solution for manual handling of low loads at high frequencies considerably reduces the force multiplier and the OCRA index.

3.3.4 Sensibility analysis

Musculoskeletal simulations' results depend on multiple factors: goodness of the input data, the definition of the markers protocol, calibration of the musculoskeletal model, precision of the muscle parameters, and so on. How much these factors impact the final results is resolved by the sensitivity analysis, which determines how different values of an independent variable affect particular estimated variables, such as joint angles or muscle and joint load. Several researchers performed extended sensitivity analysis on musculoskeletal modeling. For example, [70] demonstrated that using a subject-specific scaling model in OpenSim, such as the one proposed by [71], estimates better loads of glenohumeral muscles in simple motions than the generic model. In general, model prediction accuracy is sensitive to the properties of the muscle-tendon units and model geometry. [72] proved that the upper limbs' force estimation depends on the muscle path, moment arm, and the number of lines of action. In Opensim, a complete sensitivity analysis for upper limbs studied how much joint and muscle loads are influenced by different types of kinematic input data [73], and by changing tendon and muscle length, maximal isometric force, and pennation angle [74]. The results indicate that OpenSim upper limb musculoskeletal model is more sensitive to variation in the maximal force and muscle length. On the contrary, [75] performed a sensitivity analysis on Anybody studying the variability of the lower limb muscle activity in gait simulation by changing the same muscle-tendon parameters, founding that the tendon length is the most influential term, followed by the maximal force and muscle length. Both the two papers mentioned above calculate the Local Sensitive Index (LSI), necessary to address the influence of the muscle variation on the output of the same muscle, and the Overall Sensitivity Index (OSI) that, conversely, indicates how much a variation of the parameters of one muscle influence all the other muscle activity.

Since there are no studies regarding the sensitivity of shoulder musculoskeletal model prediction to muscle-tendon properties using AMS, we perform a preliminary study. We calculate the LSI and OSI of 11 muscle bundles of upper limbs: infraspinatus, deltoideus anterior, deltoideus lateral, pectoralis major clavicular, biceps brachii caput breve, biceps brachii caput longum, trapezius scapular, supraspinatus, deltoideus posterior, trapezius clavicular, and pectoralis major thoracic. Starting from the muscle-tendon parameters estimated by the calibration on the subject and listed in Table 4, we vary the maximal isometric force and muscle fibre length from their nominal value. In line with the anatomical variability observed in literature for each muscle-tendon unit [76], [77], the nominal values are perturbated from -10% to +10% with a step of 2.5%, modifying one by one each parameter. Thus, 176 simulations estimate the muscle activity and the joint moments for each perturbation, and the corresponding value of LSI and OSI is calculated. Results show that the moments are not affected by changing the muscle parameters: the correspondent mean OSI values are, in fact, lower than 0.05. Conversely, both LSI and OSI for the muscle activity show unexpected results compared to the values obtained in the work of Carbone et all. [75], which reach an average LSI value of 13.93% in varying fiber length and 23.08% for maximal isometric force. On the contrary, the results obtained by our study of upper limb sensitivity have an average LSI of almost 144% and 178% for OSI. Comparing the activity trend, it seems that a modest variation of muscle parameters makes the dynamics algorithm unstable such that only one muscle of each bundle is activated reaching high activity values, while the others are not activated at all, decreasing sensibly their activity with values near zero. It is fundamental to mention that in the set-up of our simulations, we force the tendon length to maintain constant values. Conversely, Carbone et all. includes muscle-tendon length equilibrium in their sensitivity study. According to the AMS developers, the stability of the tendon length values is necessary to resolve the dynamics algorithm successfully. It seems that if this value is not maintained constant, the dynamic algorithm will converge to a solution trying to change the tendon length, following the perturbations of the muscle length, thus preserving an equilibrium of the total length of the muscle-tendon unit. However, this is only a supposition, and more investigations on the dynamic's resolution and muscle recruitments in AMS are necessary for a complete dissertation. For the same reason, the obtained LSI and OSI estimates are not listed here because it is not clear how to interpret the results and the goodness of the sensitivity analysis we performed.

We also performed the sensibility of the OCRA index evaluation to IMU MoCap calibration procedures. In particular, we compared the angle joints of the upper limbs obtained by importing inside the software the kinematic data provided by the BVH data calibrated with static and dynamics poses listed in Chapter 2.3.2. Figure 8 shows the upper limb joint angles during the standard drilling test. The shaded area corresponds to the differences between the minimum and maximum value obtained by calibrating the IMU MoCap algorithm with T-pose, N-pose, C-pose, Mean Static, Elbow movement, Wrist-movements, and Functional 1. The red dot lines correspond to the OCRA joint limits that define the posture multipliers.

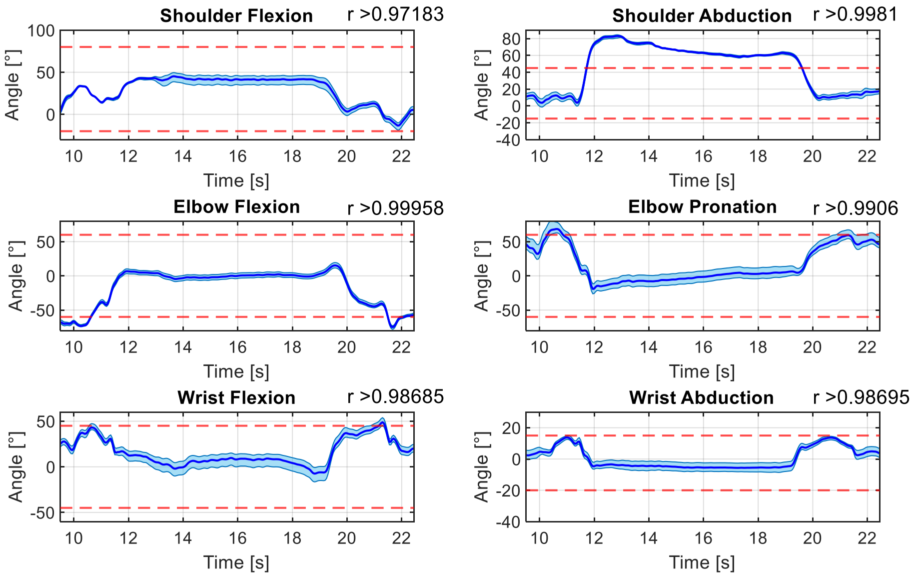

Figure 8 Upper-limb joint angles estimated by AMS with different IMU MoCap sensor-to-segment calibration

The trends between the calibration are similar, confirmed by a Pearson correlation coefficient (r) higher than 0.97 for all the angles considered. Thus, the results present an offset of the absolute values: elbow pronation angles show the higher difference (max=18°), followed by wrist flexion (max = 15°), shoulder flexion (max = 10°), elbow flexion (max = 8°), wrist deviation (max= 6°) and shoulder abduction (max = 3°). Even if these differences, the only angle that exceeds the limit is the shoulder abduction, which confirms that the posture multiplier is within the 0.7-0.6 range. Similarly, the muscle activities are not strongly affected by different calibration methods, producing a force multiplier equal to the one obtained with the functional 1 calibration method. Thus, the OCRA computed with AMS is not highly sensible to the choice of IMU MoCap calibration method.

3.4 Online Joint wrench and force multiplier estimation

The previous section has demonstrated the validity and the advantages of using musculoskeletal modelling for ergonomic evaluation. AMS can estimate the posture and force multiplier necessary to compute the OCRA. However, this process consists of several steps, is dispendious and time-consuming, and is impossible to use in real-time or directly in the working environment when the ergonomic expert performs the study. However, a peculiarity of IMU MoCap systems is their feasibility of real-time motion detection with acceptable accuracy. This characteristic makes the system able to be used as a prevention tool for online assessment of the posture multiplier. For example, in case of performing awkward positions, an external alarm or visual feedback can warn the workers, who correct their posture. However, to have a complete ergonomic analysis, also the force multiplier has to be defined. This paragraph describes the assumptions and simplifications, the algorithm, and the experimental test of an online wrench estimation of upper limb joints by knowing the force exerted on the hands. The computation of human body dynamics is an interesting topic for the study of the physical human-robot interaction [78], [79], rehabilitation [80] and ergonomics [47]. The company Scalefit (https://www.scalefit.de/home.html) claims to perform ergonomics analysis online by estimating both the awkward posture and joint load. They use the IMU MoCap suit of XSens consisting of 17 IMUs, but it is unclear if they integrated additional force sensors over the hands or foot or if they estimate the joint load only considering the human body weights and positions.

In this study, we perform an ergonomics analysis on a robot-collaborative drilling task by knowing the forces exerted on the hands and estimating the joint moment with a Newton-Euler approach. The test is like the collaborative w/o helping drilling operation described previously, and the results obtained are compared with the AMS results.

3.4.1 Definition of maximal joint torque by EN 1005-3

For EN 1005-3, the force multiplier depends on the ratio between the measured force exerted and the maximal limits reported by normative. In the same way, the force multiplier is dependent on the proportion between the estimated joint torque and a limit value not defined yet in any standard. However, those values can be derived by the force limits listed in Table 3, which allow up to 85% of the adult European working population to execute the task without exceeding their physical capacity. They are specific to common simple positions that could occur in working environments. Thus, the lengths of the body segments are estimated with the Drillis & Contini model and are necessary to calculate the torque that loads the joints, considering the F in that specific position.

The simplest human upper limb model consists of 7-DoF. The humerus is linked to the chest by the shoulder and composed of 3 revolute joints that permit three movements: shoulder abduction/adduction, internal rotation, and flexion/extension. The elbow is modelled with two rotational DoF: elbow flexion/extension and forearm pronation/supination. Finally, the hand is linked to the forearm by two revolute joints, which define palmar flexion/extension and ulnar/radial deviation. Figure 9 shows a graphic representation of the model proposed.

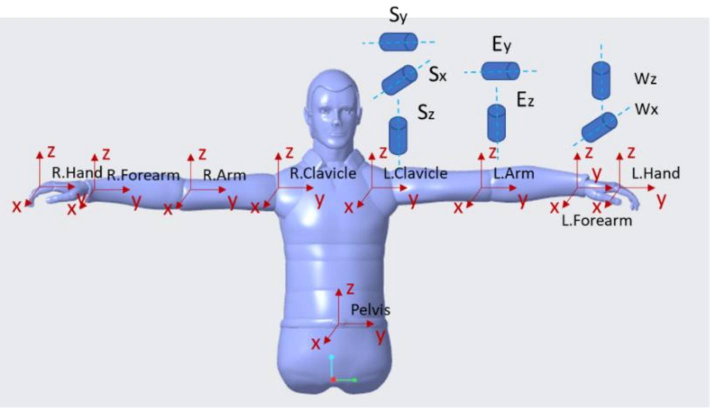

Figure 9 *Schematic representation of the 7-DoF upper limbs model*

***Table 14** Upper-limb maximal joint torque*

Activity		Shoulder [Nm]			Elbow [Nm]		Wrist [Nm]	
Arm work: sitting posture		T^{Sx}	T^{Sy}	T^{Sz}	T^{Ey}	T^{Ez}	T^{Wx}	T^{Wz}
	Upwards			22		22		9
	Downwards			-33		-33		-14
	Outwards	-18	21				-10	
	Inwards	24	-33				14	
	Pushing W trunk support							
	Pushing W/O trunk support			20				
	Pulling W trunk support							
	Pulling W/O trunk support			-18				

Thus, by multiplying the force by its lever arm vector, the maximal joint torque on each joint is estimated for each arm work in sitting positions, and the results are listed in Table 8. The distinction between different types of movements is difficult to assess, especially when computing the kinematic in real time. Thus, maintaining a high coefficient of security, the lower value in absolute values is chosen as torque limits for the 7 DoF of upper limbs. Thus, the $\overline{\%MVC}$ for determining the force factor is calculated considering the worst case among the seven upper limbs axis considered and equal to:

$$\overline{\%MVC} = \frac{1}{T}\sum_{j=1}^{n} \Delta t_j \cdot \frac{\tau_j}{T_j^L} \tag{11}$$

where τ_j is the torque computed in real-time in each axis and the T_j^L is the correspondent joint torque limit. Then, the force multiplier is determined by Table 6.

3.4.2 Joint wrench estimation algorithm

Through the IMU motion algorithm and calibration presented in Chapter 2, the quaternion $\boldsymbol{q}_{VCS_i}^{BCS}$ indicates the orientation of each i-th body coordinate system (BCS) expressed in the virtual coordinate system (VCS). The estimation of the wrenches in each joint is performed with the Newton-Euler equations, similar to the approach of [78] because they are easily implementable recursive approaches in real-time. The human body's inertial parameters derive from validated anthropometric models. The Drillis & Contini model [81] estimates the segments masses m_i with the human weight as input, while inertia $\vec{\boldsymbol{I}}_i$ is determined by the radius of gyration listed in [82] with both weight and high as input . Similarly, the position of the segment's center of mass $\boldsymbol{c}$ in the BCS depends on the height of the subject analysed. The i-th body's forces $\boldsymbol{f}_{p,i}$ and moments $\boldsymbol{\tau}_{p,i}$ in the proximal joints are a function of the respective wrench ($\boldsymbol{f}_{d,i}$, $\boldsymbol{\tau}_{d,i}$) in the i-th body's distal point. The $\sim$ symbol represents the skew-matrix, whereas the $\boldsymbol{\omega}_i$ and the $\dot{\boldsymbol{\omega}}_i$ are the angular velocities and accelerations derived from the IMU's gyroscope signal in the correspondent BCS. Thus, the resolution equation is:

$$\begin{cases} \boldsymbol{f}_{p,i} = -\boldsymbol{f}_{d,i} - m_i(\boldsymbol{g}_i + \ddot{\boldsymbol{c}}_i) \\ \boldsymbol{\tau}_{p,i} = -\boldsymbol{\tau}_{d,i} - \widetilde{\boldsymbol{l}_{d,i}}\boldsymbol{f}_{d,i} - m_i\widetilde{\boldsymbol{c}_i}(\boldsymbol{g}_i + \ddot{\boldsymbol{c}}_i) - \vec{\boldsymbol{I}}_i\dot{\boldsymbol{\omega}}_i - \widetilde{\boldsymbol{\omega}_i}(\vec{\boldsymbol{I}}_i\boldsymbol{\omega}_i) \end{cases} \tag{12}$$

where $\boldsymbol{g}_i$ and $\ddot{\boldsymbol{c}}_i$ represent the gravity acceleration and the linear acceleration of the center of mass in the i-th body reference system respectively, and $\boldsymbol{l}_{d,i}$ the distance between the proximal and distal points of the segment. The wrench applied by the j-th (distal) body to the body i is determined in the previous iterations i+1 and expressed in the body coordinates system by the joint quaternion $\boldsymbol{q}_{i,j}^{Joint}$, which defines the joint angles between two successive BCS. The wrench estimation starts from the distal segment point, where the force exerted by external machinery or loads is known. This method is simple and fast and can be easily implemented in real-time.

3.4.3 Material and Methods

The same experimental collaborative robotic scenario, described in Section 3.3.1, is used to validate the proposed methodology. A man subject (height = 1.78 m, weight = 70 Kg) wears the Shadow MoCap suit and drills holes at four different locations: the first one is on a plane perpendicular to the ground, while the last three are on a plane parallel to the ground, at the height of approximately 1 m. The cobot supports the total weight of the drills by gravity compensation strategy. Unlike the previous case, the admittance control is not activated, and the subject pushes with more force, thus stimulating variations in the force multiplier value. The sensor positioned in the cobot EE, as shown in Figure 2, records the force and torque exerted on the hands. The IMU MoCap and the joint wrench estimation algorithms are implemented into a ROS package with a methodology that will be fully described in the next chapter. After a complete calibration of the IMU MoCap system performing the Functional1 pipeline, the evaluation is performed in real-time (100 Hz) and then saved in a .csv file. To test the validity of the method, the angle and joint wrenches estimated are compared with the results obtained in AMS. In particular, the IMU kinematic data are firstly transformed into a BVH file, with a frequency downsampling to 20 Hz, and imported into AMS. Similarly, the physical human-robot interaction forces are first referred to in the hand coordinate system and imported into the AMS model.

3.4.4 Results

The results of joint angles and moments of the proposed algorithm for estimating OCRA ergonomics posture and force multipliers are shown in the figure below. In particular, Figure 10 compares the angle computed in real-time (blue line) with the one obtained with AMS, both correlated to the angle limits set in the normative (red dot line). The results show a good correlation except for the wrist angles, probably due to some error in the AMS computation: visually is possible to notice that the hand assumes an unreal and unexpected position, probably for lack of constraints due to the protocol used. Figure 11 shows the comparison between the joints' moments. Those values show similarities in values and trends, especially in the elbow joint. Differences in the kinematics angles and the definition of the inertial parameters of the upper limbs of the two systems can cause discrepancies in the results. The scaling law of AMS for inertial parameters differs from the one used in our definition, resulting in different values of inertial matrices. Although the biomechanical human model definition is upgradeable and

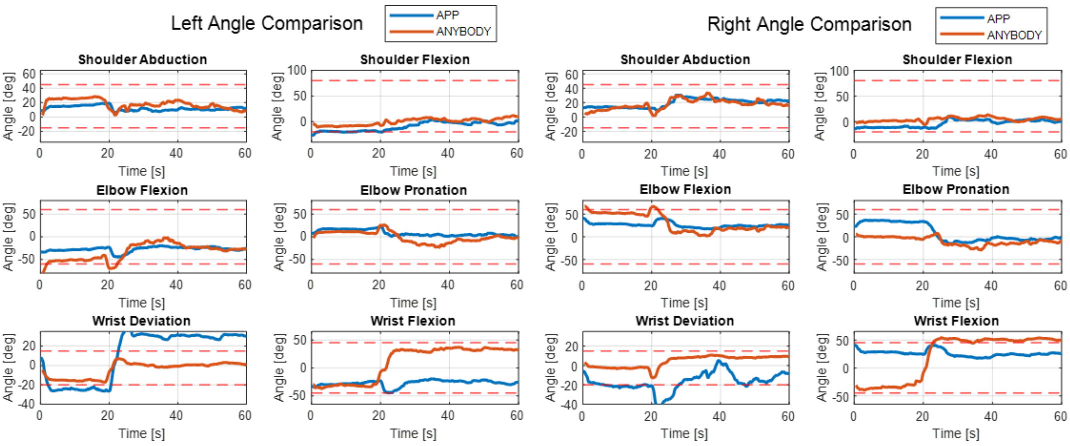

Figure 14 Upper-limbs joints moments comparison between AMS and the proposed method

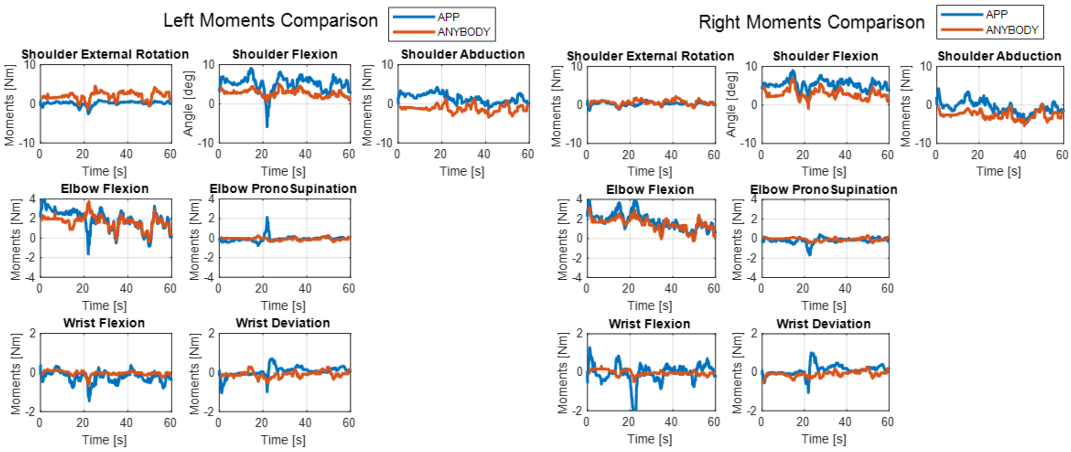

Figure 11 Upper-limbs joints moments comparison between AMS and the proposed method

better definable, the real-time dynamic estimation shows acceptable and promising results.

From these moments data, the algorithm computes the force multiplier dividing the obtained value, for each technical action, with the maximal joint admissible torque, listed in Table 8. The force multiplier estimated with Eq.11, and interpolated following the suggestion of the Standard, is 0.6368. The AMS muscle activity analysis shows that among all the muscles, the most stressed muscle group is the shoulder one. The %MVC of the left and right shoulder is equal to 10.04 and 11.79 respectively; for the elbow is 6.21 and 6.06, and for the wrist is equal to 6.21 and 5.88. The maximal value is of the right shoulder, where the deltoideus anterior muscle reaches the maximal value. The corresponding force multiplier equals 0.5861, and it is comparable to the one obtained by the proposed procedure.

In conclusion, IMU MoCap systems integrated with external force and torque sensors are a promising tool to assess ergonomics analysis in real-time, thus, reducing the workers' musculoskeletal disorders. The algorithm proposed for tracking the workers' motion and joint loads returns results comparable to the one simulated with AMS. The procedure and the definition of maximal joint torques using EN 1005-3 permit estimating the force multiplier by joint torque online evaluation and monitoring the workers' musculoskeletal overloads in real-time. This approach is highly usable in a contest where the workers must perform repetitive tasks for several hours. In a safer working environment, if an excessive joint load or a prolonged awkward posture is detected, an alarm signal or visual feedback would warn the workers to be in potentially dangerous situations for their musculoskeletal health.

3.5 Towards reduced and subject-specific biomechanical models

It is evident that the value of motion tracking systems and ergonomics assessments depends on the choice of the sensor system and the biomechanical models that perform the analysis. The more the models can reproduce the actual behaviour of the human, the more the calculation of kinematic, dynamics and ergonomic parameters reflect reality. One of the main objectives of biomechanics is to define subject-specific human models. While the determination of muscle and tendon parameters is difficult because invasive sensors are needed, the joints' axis of rotation and kinematic constraints are identifiable with less invasive detectors. As mentioned in Chapter 2, it is common to perform functional movements to assess the joint axis of rotation with marker-base and marker-less MoCap systems. The constraints imposed by reduced biomechanical models could reduce the noises and intrinsic errors of the instrumentation and increase the overall accuracy of kinematic analysis. In this direction, we reduced the upper limb DoF from 9 to 7: elbow and wrist's spherical joints are substituted with two revolute joints with non-orthogonal axes. Moreover, the axis directions of the revolute joints are obtained by functional movements captured by the IMU MoCap system to develop a subject-specific model. Specifically, with the same approach used to perform the dynamic sensor-to-segment calibration proposed in Chapter 2, the quaternions of the body coordinate system $\boldsymbol{q}_{VCS_i}^{BCS}$ determine the direction vector of elbow and wrist axes in the virtual coordinate frame. With the flexion extension and pronation-supination of the elbow, the non-orthogonal axes are defined by the quaternion of the arm's body coordinate system. Similarly, the elbow axes in VCS are identified with the hand-body coordinate system during flexion-extension and abduction-adduction activities. The kinematic is definable with successive elementary rotation matrices misaligned according to the angle computed by the joint movements in VCS. The Drillis & Contini model defines the distances between the joints. Attached to each body segment 3 virtual markers in specific positions are defined. The kinematic is resolved like the approach of AMS. The IMU outputs move the 9-DoF upper limbs skeleton, modeled with only spherical joints, by the MoCap algorithm described in Chapter 2. That skeleton has

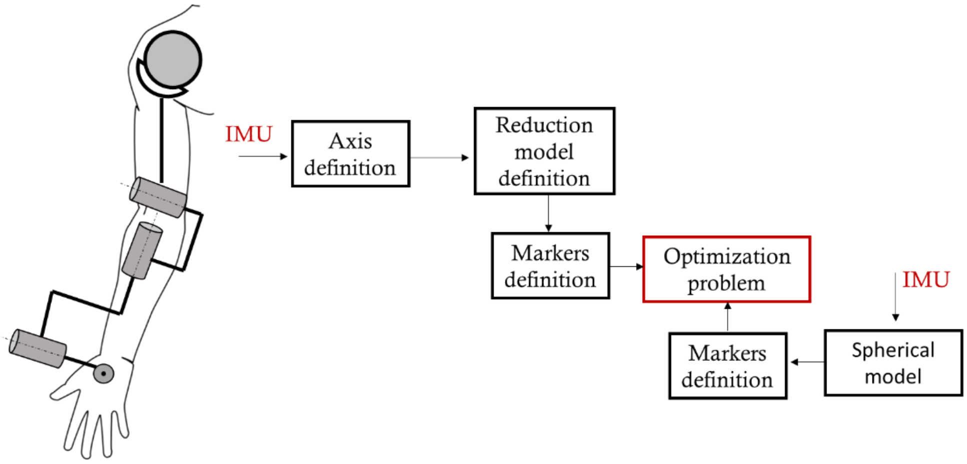

***Figure 12**15 Left: schematic representation reduce model, right: scheme of the proposed procedure*

attached the same number of markers of the reduced biomechanical model in the exact positions.

With a global optimization that minimizes the distance between the markers of the two models, the joint angle values are estimated offline. This minimization problem is constrained to resolve the kinematic with joints angle inside a range of feasible and possible configurations. Those values of motions are detailed in [82]. Figure 12 shows a scheme of the procedure described above and a schematic representation of the reduced and subject-specific biomechanical models.

A preliminary model is developed offline in Matlab 2020a, showing promising results. The global optimization filters out some IMU noise and constrains the motion into physiological ranges of motion.

References

[1] European Agency for Safety and Health at Work., IKEI., e Panteia., *Work-related musculoskeletal disorders: prevalence, costs and demographics in the EU.* LU: Publications Office, 2019. Consultato: 22 ottobre 2022. [Online]. Disponibile su: https://data.europa.eu/doi/10.2802/66947

[2] S. L. Delp *et al.*, «OpenSim: Open-Source Software to Create and Analyze Dynamic Simulations of Movement», *IEEE Trans. Biomed. Eng.*, vol. 54, fasc. 11, pp. 1940–1950, nov. 2007, doi: 10.1109/TBME.2007.901024.

[3] M. Damsgaard, J. Rasmussen, S. T. Christensen, E. Surma, e M. de Zee, «Analysis of musculoskeletal systems in the AnyBody Modeling System»,

Simulation Modelling Practice and Theory, vol. 14, fasc. 8, pp. 1100–1111, nov. 2006, doi: 10.1016/j.simpat.2006.09.001.

[4] S. Skals, R. Bláfoss, L. L. Andersen, M. S. Andersen, e M. de Zee, «Manual material handling in the supermarket sector. Part 2: Knee, spine and shoulder joint reaction forces», *Applied Ergonomics*, vol. 92, p. 103345, apr. 2021, doi: 10.1016/j.apergo.2020.103345.

[5] X. Li, A. Komeili, M. Gül, e M. El-Rich, «A framework for evaluating muscle activity during repetitive manual material handling in construction manufacturing», *Automation in Construction*, vol. 79, pp. 39–48, lug. 2017, doi: 10.1016/j.autcon.2017.01.005.

[6] M. Bahramian, M. A. Shayestehpour, M. Yavari, H. Mehrabi, e N. Arjmand, «Musculoskeletal injury risk assessment in a car dashboard assembly line using various quantitative and qualitative tools», in *2021 28th National and 6th International Iranian Conference on Biomedical Engineering (ICBME)*, Tehran, Iran, Islamic Republic of, nov. 2021, pp. 310–316. doi: 10.1109/ICBME54433.2021.9750385.

[7] H. Atici, D. Gonen, A. Oral, e B. Kaya, «Ergonomic Analysis of an Assembly Line Using the AnyBody Modeling System», presentato al The 3rd World Congress on Mechanical, Chemical, and Material Engineering, giu. 2017. doi: 10.11159/icmie17.125.

[8] G. C. David, «Ergonomic methods for assessing exposure to risk factors for work-related musculoskeletal disorders», *Occupational Medicine*, vol. 55, fasc. 3, pp. 190–199, mag. 2005, doi: 10.1093/occmed/kqi082.

[9] C. Wiktorin, L. Karlqvist, e J. Winkel, «Validity of self-reported exposures to work postures and manual materials handling. Stockholm MUSIC I Study Group.», *Scand J Work Environ Health*, vol. 19, fasc. 3, pp. 208–214, giu. 1993, doi: 10.5271/sjweh.1481.

[10] A. Burdorf e J. Laan, «Comparison of methods for the assessment of postural load on the back.», *Scand J Work Environ Health*, vol. 17, fasc. 6, pp. 425–429, dic. 1991, doi: 10.5271/sjweh.1679.

[11] D. Dane, M. Feuerstein, G. D. Huang, L. Dimberg, D. Ali, e A. Lincoln, «Measurement Properties of a Self-Report Index of Ergonomic Exposures for Use in an Office Work Environment», vol. 44, fasc. 1, p. 9, 2002.

[12] G. Li e P. Buckle, «Current techniques for assessing physical exposure to work-related musculoskeletal risks, with emphasis on posture-based methods», *Ergonomics*, vol. 42, fasc. 5, pp. 674–695, mag. 1999, doi: 10.1080/001401399185388.

[13] C. Fransson-Hall, R. Gloria, Å. Kilbom, J. Winkel, L. Karlqvist, e C. Wiktorin, «A portable ergonomic observation method (PEO) for computerized on-line recording of postures and manual handling», *Applied Ergonomics*, vol. 26, fasc. 2, pp. 93–100, apr. 1995, doi: 10.1016/0003-6870(95)00003-U.

[14] R. Ketola *et al.*, «Effects of ergonomic intervention in work with video display units», *Scand J Work Environ Health*, vol. 28, fasc. 1, pp. 18–24, feb. 2002, doi: 10.5271/sjweh.642.

[15] C.-H. Chen, Y. H. Hu, T. Y. Yen, e R. G. Radwin, «Automated Video Exposure Assessment of Repetitive Hand Activity Level for a Load Transfer Task», *Hum Factors*, vol. 55, fasc. 2, pp. 298–308, apr. 2013, doi: 10.1177/0018720812458121.

[16] R. G. Radwin, «Automated Video Exposure Assessment of Repetitive Motion», *Proceedings of the Human Factors and Ergonomics Society Annual Meeting*, vol. 55, fasc. 1, pp. 995–996, set. 2011, doi: 10.1177/1071181311551207.

[17] M. Bortolini, M. Gamberi, F. Pilati, e A. Regattieri, «Automatic assessment of the ergonomic risk for manual manufacturing and assembly activities through optical motion capture technology», *Procedia CIRP*, vol. 72, pp. 81–86, 2018, doi: 10.1016/j.procir.2018.03.198.

[18] M. Bortolini, M. Faccio, M. Gamberi, e F. Pilati, «Motion Analysis System (MAS) for production and ergonomics assessment in the manufacturing processes», *Computers & Industrial Engineering*, vol. 139, p. 105485, gen. 2020, doi: 10.1016/j.cie.2018.10.046.

[19] R. Tian e V. G. Duffy, «Computerized task risk assessment using digital human modeling based Job Risk Classification Model», *Computers & Industrial Engineering*, vol. 61, fasc. 4, pp. 1044–1052, nov. 2011, doi: 10.1016/j.cie.2011.06.018.

[20] G. Hansson, P. Asterland, N.-G. Holmer, e S. Skerfving, «Validity and reliability of triaxial accelerometers for inclinometry in posture analysis», *Med. Biol. Eng. Comput.*, vol. 39, fasc. 4, pp. 405–413, lug. 2001, doi: 10.1007/BF02345361.

[21] A. Rezende, C. Alves, I. Marques, M. Silva, e E. Naves, «Polymer Optical Fiber Goniometer: A New Portable, Low Cost and Reliable Sensor for Joint Analysis», *Sensors*, vol. 18, fasc. 12, p. 4293, dic. 2018, doi: 10.3390/s18124293.

[22] J. A. Bell e M. Stigant, «Development of a fibre optic goniometer system to measure lumbar and hip movement to detect activities and their lumbar

postures», *Journal of Medical Engineering & Technology*, vol. 31, fasc. 5, pp. 361–366, gen. 2007, doi: 10.1080/03091900600996735.

[23] S. E. Mathiassen e A. Burdorf, «Statistical power and measurement allocation in ergonomic intervention studies assessing upper trapezius EMG amplitude A case study of assembly work», *Journal of Electromyography and Kinesiology*, p. 13, 2002.

[24] M. Forsman, G.-Å. Hansson, L. Medbo, P. Asterland, e T. Engström, «A method for evaluation of manual work using synchronised video recordings and physiological measurements», *Applied Ergonomics*, vol. 33, fasc. 6, pp. 533–540, nov. 2002, doi: 10.1016/S0003-6870(02)00070-4.

[25] L. Tsao, L. Li, e L. Ma, «Human Work and Status Evaluation Based on Wearable Sensors in Human Factors and Ergonomics: A Review», *IEEE Trans. Human-Mach. Syst.*, vol. 49, fasc. 1, pp. 72–84, feb. 2019, doi: 10.1109/THMS.2018.2878824.

[26] E. Stefana, F. Marciano, D. Rossi, P. Cocca, e G. Tomasoni, «Wearable Devices for Ergonomics: A Systematic Literature Review», *Sensors*, vol. 21, fasc. 3, p. 777, gen. 2021, doi: 10.3390/s21030777.

[27] *Ergonomics. Manual handling Pushing and pulling*, Withdrawn. 2007.

[28] *Ergonomics. Manual handling Lifting and carrying*, Withdrawn. 2012.

[29] *Ergonomics. Manual handling Handling of low loads at high frequency*, Under Review. 2015.

[30] «Applications manual for the revised NIOSH lifting equation.», U.S. Department of Health and Human Services, Public Health Service, Centers for Disease Control and Prevention, National Institute for Occupational Safety and Health, set. 2021. doi: 10.26616/NIOSHPUB94110revised092021.

[31] S. H. Snook e V. M. Ciriello, «The design of manual handling tasks: revised tables of maximum acceptable weights and forces», *Ergonomics*, vol. 34, fasc. 9, pp. 1197–1213, set. 1991, doi: 10.1080/00140139108964855.

[32] O. Karhu, P. Kansi, e I. Kuorinka, «Correcting working postures in industry: A practical method for analysis», *Applied Ergonomics*, vol. 8, fasc. 4, pp. 199–201, dic. 1977, doi: 10.1016/0003-6870(77)90164-8.

[33] L. McAtamney e E. Nigel Corlett, «RULA: a survey method for the investigation of work-related upper limb disorders», *Applied Ergonomics*, vol. 24, fasc. 2, pp. 91–99, apr. 1993, doi: 10.1016/0003-6870(93)90080-S.

[34] S. Hignett e L. McAtamney, «Rapid Entire Body Assessment (REBA)», *Applied Ergonomics*, vol. 31, fasc. 2, pp. 201–205, apr. 2000, doi: 10.1016/S0003-6870(99)00039-3.

[35] J. Steven Moore e A. Garg, «The Strain Index: A Proposed Method to Analyze Jobs For Risk of Distal Upper Extremity Disorders», *American Industrial Hygiene Association Journal*, vol. 56, fasc. 5, pp. 443–458, mag. 1995, doi: 10.1080/15428119591016863.

[36] G. David, V. Woods, G. Li, e P. Buckle, «The development of the Quick Exposure Check (QEC) for assessing exposure to risk factors for work-related musculoskeletal disorders», *Applied Ergonomics*, vol. 39, fasc. 1, pp. 57–69, gen. 2008, doi: 10.1016/j.apergo.2007.03.002.

[37] E. Occhipinti, «OCRA: a concise index for the assessment of exposure to repetitive movements of the upper limbs», *Ergonomics*, vol. 41, fasc. 9, pp. 1290–1311, set. 1998, doi: 10.1080/001401398186315.

[38] F. Caputo, A. Greco, E. D'Amato, I. Notaro, e S. Spada, «IMU-Based Motion Capture Wearable System for Ergonomic Assessment in Industrial Environment», in *Advances in Human Factors in Wearable Technologies and Game Design*, vol. 795, T. Z. Ahram, A c. di Cham: Springer International Publishing, 2019, pp. 215–225. doi: 10.1007/978-3-319-94619-1_21.

[39] K. G. Schaub *et al.*, «Ergonomic assessment of automotive assembly tasks with digital human modelling and the "ergonomics assessment worksheet" (EAWS)», *IJHFMS*, vol. 3, fasc. 3/4, p. 398, 2012, doi: 10.1504/IJHFMS.2012.051581.

[40] I. Conforti, I. Mileti, Z. Del Prete, e E. Palermo, «Assessing ergonomics and biomechanical risk in manual handling of loads through a wearable system», in *2019 II Workshop on Metrology for Industry 4.0 and IoT (MetroInd4.0&IoT)*, Naples, Italy, giu. 2019, pp. 388–393. doi: 10.1109/METROI4.2019.8792843.

[41] I. Conforti, I. Mileti, Z. Del Prete, e E. Palermo, «Measuring Biomechanical Risk in Lifting Load Tasks Through Wearable System and Machine-Learning Approach», *Sensors*, vol. 20, fasc. 6, p. 1557, mar. 2020, doi: 10.3390/s20061557.

[42] P. Giannini, G. Bassani, C. A. Avizzano, e A. Filippeschi, «Wearable Sensor Network for Biomechanical Overload Assessment in Manual Material Handling», *Sensors*, vol. 20, fasc. 14, p. 3877, lug. 2020, doi: 10.3390/s20143877.

[43] S. E. Lenzi, C. E. Standoli, G. Andreoni, P. Perego, e N. F. Lopomo, «Comparison Among Standard Method, Dedicated Toolbox and Kinematic-Based Approach in Assessing Risk of Developing Upper Limb Musculoskeletal Disorders», in *Advances in Human Factors in Wearable Technologies and Game Design*, vol. 795, T. Z. Ahram, A c. di Cham: Springer International Publishing, 2019, pp. 135–145. doi: 10.1007/978-3-319-94619-1_13.

[44] C. Lins, S. Fudickar, A. Gerka, e A. Hein, «A Wearable Vibrotactile Interface for Unfavorable Posture Awareness Warning»:, in *Proceedings of the 4th International Conference on Information and Communication Technologies for Ageing Well and e-Health*, Funchal, Madeira, Portugal, 2018, pp. 178–183. doi: 10.5220/0006734901780183.

[45] A. J. Meltzer *et al.*, «Measuring Ergonomic Risk in Operating Surgeons by Using Wearable Technology», *JAMA Surg*, vol. 155, fasc. 5, p. 444, mag. 2020, doi: 10.1001/jamasurg.2019.6384.

[46] L. Peppoloni, A. Filippeschi, e E. Ruffaldi, «Assessment of task ergonomics with an upper limb wearable device», in *22nd Mediterranean Conference on Control and Automation*, Palermo, Italy, giu. 2014, pp. 340–345. doi: 10.1109/MED.2014.6961394.

[47] L. Peppoloni, A. Filippeschi, E. Ruffaldi, e C. A. Avizzano, «A novel wearable system for the online assessment of risk for biomechanical load in repetitive efforts», *International Journal of Industrial Ergonomics*, vol. 52, pp. 1–11, mar. 2016, doi: 10.1016/j.ergon.2015.07.002.

[48] Z. Sedighi Maman, M. A. Alamdar Yazdi, L. A. Cavuoto, e F. M. Megahed, «A data-driven approach to modeling physical fatigue in the workplace using wearable sensors», *Applied Ergonomics*, vol. 65, pp. 515–529, nov. 2017, doi: 10.1016/j.apergo.2017.02.001.

[49] E. Valero, A. Sivanathan, F. Bosché, e M. Abdel-Wahab, «Analysis of construction trade worker body motions using a wearable and wireless motion sensor network», *Automation in Construction*, vol. 83, pp. 48–55, nov. 2017, doi: 10.1016/j.autcon.2017.08.001.

[50] X. Yan, H. Li, A. R. Li, e H. Zhang, «Wearable IMU-based real-time motion warning system for construction workers' musculoskeletal disorders prevention», *Automation in Construction*, vol. 74, pp. 2–11, feb. 2017, doi: 10.1016/j.autcon.2016.11.007.

[51] M.-L. Lu, M. S. Barim, S. Feng, G. Hughes, M. Hayden, e D. Werren, «Development of a Wearable IMU System for Automatically Assessing Lifting Risk Factors», in *Digital Human Modeling and Applications in Health, Safety, Ergonomics and Risk Management. Posture, Motion and Health*, vol. 12198, V. G. Duffy, A c. di Cham: Springer International Publishing, 2020, pp. 194–213. doi: 10.1007/978-3-030-49904-4_15.

[52] S. Kim e M. A. Nussbaum, «An evaluation of classification algorithms for manual material handling tasks based on data obtained using wearable technologies», *Ergonomics*, vol. 57, fasc. 7, pp. 1040–1051, lug. 2014, doi: 10.1080/00140139.2014.907450.

[53] *Safety of machinery. Human physical performance Recommended force limits for machinery operation*, Under Review. 2009.

[54] M. I. Griep, E. Borg, K. Collys, e D. L. Massart, «Category ratio scale as an alternative to magnitude matching for age-related taste and odour perception», *Food Quality and Preference*, vol. 9, fasc. 1–2, pp. 67–72, gen. 1998, doi: 10.1016/S0950-3293(97)00030-X.

[55] U. Trinler, H. Schwameder, R. Baker, e N. Alexander, «Muscle force estimation in clinical gait analysis using AnyBody and OpenSim», *Journal of Biomechanics*, vol. 86, pp. 55–63, mar. 2019, doi: 10.1016/j.jbiomech.2019.01.045.

[56] N. Alexander, H. Schwameder, R. Baker, e U. Trinler, «Effect of different walking speeds on joint and muscle force estimation using AnyBody and OpenSim», *Gait & Posture*, vol. 90, pp. 197–203, ott. 2021, doi: 10.1016/j.gaitpost.2021.08.026.

[57] Y. Kim, Y. Jung, W. Choi, K. Lee, e S. Koo, «Similarities and differences between musculoskeletal simulations of OpenSim and AnyBody modeling system», *J Mech Sci Technol*, vol. 32, fasc. 12, pp. 6037–6044, dic. 2018, doi: 10.1007/s12206-018-1154-0.

[58] M. Al Borno *et al.*, «OpenSense: An open-source toolbox for inertial-measurement-unit-based measurement of lower extremity kinematics over long durations», *J NeuroEngineering Rehabil*, vol. 19, fasc. 1, p. 22, dic. 2022, doi: 10.1186/s12984-022-01001-x.

[59] F. E. Zajac, «Muscle and tendon: properties, models, scaling, and application to biomechanics and motor control», *Crit Rev Biomed Eng*, vol. 17, fasc. 4, pp. 359–411, 1989.

[60] L. Zhang, Y. Liu, R. Wang, C. Smith, e E. M. Gutierrez-Farewik, «Modeling and Simulation of a Human Knee Exoskeleton's Assistive Strategies and Interaction», *Front. Neurorobot.*, vol. 15, p. 620928, mar. 2021, doi: 10.3389/fnbot.2021.620928.

[61] L. Fritzsche *et al.*, «Assessing the efficiency of exoskeletons in physical strain reduction by biomechanical simulation with AnyBody Modeling System», *Wearable Technol.*, vol. 2, p. e6, 2021, doi: 10.1017/wtc.2021.5.

[62] J. Z. Wu, S. S. Chiou, e C. S. Pan, «Analysis of Musculoskeletal Loadings in Lower Limbs During Stilts Walking in Occupational Activity», *Ann Biomed Eng*, vol. 37, fasc. 6, pp. 1177–1189, giu. 2009, doi: 10.1007/s10439-009-9674-5.

[63] H. Baskar e S. M. R. Nadaradjane, «Minimization of Metabolic Cost of Muscles Based on Human Exoskeleton Modeling : A Simulation», *IJBES*, vol. 3, fasc. 4, pp. 01–09, ott. 2016, doi: 10.5121/ijbes.2016.3401.

[64] A. Gonzalez-Mendoza *et al.*, «Upper Limb Musculoskeletal Modeling for Human-Exoskeleton Interaction», in *2019 16th International Conference on Electrical Engineering, Computing Science and Automatic Control (CCE)*, Mexico City, Mexico, set. 2019, pp. 1–5. doi: 10.1109/ICEEE.2019.8884537.

[65] Y. Aydin, D. Sirintuna, e C. Basdogan, «Towards Collaborative Drilling with a Cobot Using Admittance Controller», *Transactions of the Institute of Measurement and Control*, vol. 43, fasc. 8, pp. 1760–1773, mag. 2021, doi: 10.1177/0142331220934643.

[66] A. Karatsidis, «Musculoskeletal model-based inverse dynamic analysis under ambulatory conditions using inertial motion capture», *Medical Engineering and Physics*, p. 10, 2019.

[67] A. Karatsidis *et al.*, «Predicting kinetics using musculoskeletal modeling and inertial motion capture». arXiv, 5 gennaio 2018. Consultato: 27 ottobre 2022. [Online]. Disponibile su: http://arxiv.org/abs/1801.01668

[68] F. G. Larsen, «Estimation of Spinal Loading During Manual Materials Handling Using Inertial Motion Capture», p. 17.

[69] M. Hedegaard, A. Anvari-Moghaddam, B. K. Jensen, C. B. Jensen, M. K. Pedersen, e A. Samani, «Prediction of energy expenditure during activities of daily living by a wearable set of inertial sensors», *Medical Engineering & Physics*, vol. 75, pp. 13–22, gen. 2020, doi: 10.1016/j.medengphy.2019.10.006.

[70] W. Wu, P. V. S. Lee, A. L. Bryant, M. Galea, e D. C. Ackland, «Subject-specific musculoskeletal modeling in the evaluation of shoulder muscle and joint function», *Journal of Biomechanics*, vol. 49, fasc. 15, pp. 3626–3634, nov. 2016, doi: 10.1016/j.jbiomech.2016.09.025.

[71] L. Modenese, E. Ceseracciu, M. Reggiani, e D. G. Lloyd, «Estimation of musculotendon parameters for scaled and subject specific musculoskeletal models using an optimization technique», *Journal of Biomechanics*, vol. 49, fasc. 2, pp. 141–148, gen. 2016, doi: 10.1016/j.jbiomech.2015.11.006.

[72] D. C. Ackland, Y.-C. Lin, e M. G. Pandy, «Sensitivity of model predictions of muscle function to changes in moment arms and muscle–tendon properties: A Monte-Carlo analysis», *Journal of Biomechanics*, vol. 45, fasc. 8, pp. 1463–1471, mag. 2012, doi: 10.1016/j.jbiomech.2012.02.023.

[73] Y. Blache e M. Begon, «Influence of Shoulder Kinematic Estimate on Joint and Muscle Mechanics Predicted by Musculoskeletal Model», *IEEE Trans.*

Biomed. Eng., vol. 65, fasc. 4, pp. 715–722, apr. 2018, doi: 10.1109/TBME.2017.2716186.

[74] Y. Blache, B. Michaud, I. Rogowski, K. Monteil, e M. Begon, «Sensitivity of Shoulder Musculoskeletal Model Predictions to Muscle–Tendon Properties», *IEEE Trans. Biomed. Eng.*, vol. 66, fasc. 5, pp. 1309–1317, mag. 2019, doi: 10.1109/TBME.2018.2872833.

[75] V. Carbone, M. M. van der Krogt, H. F. J. M. Koopman, e N. Verdonschot, «Sensitivity of subject-specific models to Hill muscle–tendon model parameters in simulations of gait», *Journal of Biomechanics*, vol. 49, fasc. 9, pp. 1953–1960, giu. 2016, doi: 10.1016/j.jbiomech.2016.04.008.

[76] H. E. J. Veeger, F. C. T. Van Der Helm, L. H. V. Van Der Woude, G. M. Pronk, e R. H. Rozendal, «Inertia and muscle contraction parameters for musculoskeletal modelling of the shoulder mechanism», *Journal of Biomechanics*, vol. 24, fasc. 7, pp. 615–629, gen. 1991, doi: 10.1016/0021-9290(91)90294-W.

[77] J. Langenderfer, S. A. Jerabek, V. B. Thangamani, J. E. Kuhn, e R. E. Hughes, «Musculoskeletal parameters of muscles crossing the shoulder and elbow and the effect of sarcomere length sample size on estimation of optimal muscle length», *Clinical Biomechanics*, vol. 19, fasc. 7, pp. 664–670, ago. 2004, doi: 10.1016/j.clinbiomech.2004.04.009.

[78] C. Latella *et al.*, «Towards real-time whole-body human dynamics estimation through probabilistic sensor fusion algorithms: A physical human–robot interaction case study», *Auton Robot*, vol. 43, fasc. 6, pp. 1591–1603, ago. 2019, doi: 10.1007/s10514-018-9808-4.

[79] W. Kim, J. Lee, N. Tsagarakis, e A. Ajoudani, «A real-time and reduced-complexity approach to the detection and monitoring of static joint overloading in humans», in *2017 International Conference on Rehabilitation Robotics (ICORR)*, London, lug. 2017, pp. 828–834. doi: 10.1109/ICORR.2017.8009351.

[80] D. Stanev *et al.*, «Real-Time Musculoskeletal Kinematics and Dynamics Analysis Using Marker- and IMU-Based Solutions in Rehabilitation», *Sensors*, vol. 21, fasc. 5, p. 1804, mar. 2021, doi: 10.3390/s21051804.

[81] R. Contini, R. J. Drillis, e M. Bluestein, «Determination of Body Segment Parameters», *Hum Factors*, vol. 5, fasc. 5, pp. 493–504, ott. 1963, doi: 10.1177/001872086300500508.

[82] D. A. Winter, *Biomechanics and motor control of human movement*, 4th ed. Hoboken, N.J: Wiley, 2009.

Chapter 4

Cobot-IMU hand guiding system with online collision avoidance

With the growing interest of the manufacturing industry in systems able to reach higher productivity while maintaining at the same time high flexibility and efficiency, one of the main goals of Industry 4.0 is to take advantage of the enormous potentiality of collaborative robotics. During the last decade, cobots were widespread in the automotive industry, which requires increasing customization and product flexibility. It is estimated that the number of cobots sold to electronic and automotive in 2020 was 22,000 units, with a positive trend for the next decade. Thanks to their high flexibility, cobots are recently introduced in surgery applications: for example, for brain and spinal surgery, the cobot automatically moves its high-powered microscope and provides high-resolution images of the surgical area, or in total knee arthroplasty operation, the cobot moves for better define the cutting plane and reducing bones axes misalignments. Moreover, cobots have been introduced in rehabilitation for training the upper limbs in neurologically impaired individuals. In general, cobots can increase productivity and improve product and life quality. In industrial applications, the cobot also releases human workers from strenuous and health-damaging activities. However, effective collaboration requires physical contact between the robot and the human in a common workspace where human safety is guaranteed.

Among all the collaborative solutions, redundant cobots can achieve more dexterous robot motion and increase the flexibility of the collaboration. The manipulators are kinematically redundant when more DoF than needed to execute a given task. For example, it is possible to command the auxiliary joints space to avoid joint limits and singularities or avert obstacles [1].

Hand-guiding operation is a task in which the operator manually guides the collaborative robot to follow an arbitrary desired trajectory. A redundant cobot under hand-guiding motion can force the redundant chain to assume configurations that ensure safety or facilitate the human to perform a specific task. In general, a practical collision avoidance strategy requires the accurate instantaneous posture knowledge of the human operator. In robotics, the most used MoCap systems are vision sensors, such as stereophotogrammetric cameras, depth cameras, RGB cameras, and lasers [2]–[6]. Nevertheless, a vision system suffers from occlusion problems in cluttered environments with varying light conditions [7].

As an alternative, a new research area considers collaborative solutions based on IMU MoCap systems that are free of occlusion problems and represent a possible solution for their compactness, low cost, and fast response. However, IMUs are prone to drifting errors, and their integration with robotic systems needs more investigation. To the authors' knowledge, the only studies which dealt with this integration are those from [8], [9], in which the position of a free-walking human in space is tracked by IMUs and lasers in a collaborative scenario.

In this chapter, we study a collaborative hand-guiding task in which a safe human-robot interaction (HRI) is ensured by performing the collision avoidance strategy in null space and tracking the human position with IMU MoCap systems. This HRI scenario consists of an operator wearing the Shadow MoCap systems, who guides the cobot by a handle mounted to its EE. During the operation, the cobot control command allows smooth EE manual guidance and a safety control strategy, which maximizes the distance between the redundant links and the operator to avoid unexpected collisions. In the proposed setup, the control strategy needs to acquire the positions of operator body segments from the MoCap system and calculate the distance between the human and the cobot to command the control strategy. Differently from previous works, the IMUs 3D position drifting error is inhibited by making the operator stand in a fixed location with a hand firmly attached to the EE and continuously syncing the hand with the EE position. The HRI control command is computed in real-time under the ros_control framework. The proposed setup is tested with a simple experiment to evaluate the capability of the integration of IMUs system for online collision avoidance in null space during hand-guiding tasks. Redundant cobots are promising for their flexibility in chain configuration: without changing EE positioning, the auxiliary motion can relocate the robot far enough from the operator, thus preventing the assumption of awkward postures, which could lead to injuries.

In the following pages, section 1 describes the experimental setup implemented in real-time; section 2 defines the calibration of the IMU MoCap system with the robot, and section 3 describes the robot control strategy. Finally, section 4 reports the results of the tests performed.

4.1 IMU MoCap system integration in cobot controller

The Franka Emika Panda redundant serial robot and the Shadow MoCap system are the hardware integrated for hand-guiding collaborative applications. Franka Emika provides *libfranka*, an open-source C++ interface for sending real-time control commands to the robot. It further integrates this library into the *ros_control* framework (*FrankaROS*) to be compatible with ROS ecosystem while maintaining real-time capability (1kHz). Motion Shadow suit provides an open-source C++ SDK that programmatically handles the real-time (100Hz) data streams coming from each IMU. Each IMU is connected to a wireless hub, that gathers the data and estimates the attitudes through sensor fusion algorithms. The raw data of the sensors and the estimated attitudes are transmitted via Wi-Fi to the workstation PC which runs the robot controller. The sensor data are integrated into the robot control protocol for calculating new control commands in real-time (i.e., sensor integration layer). For this purpose, we extended *FrankaHW*, the hardware interface defined in *FrankaROS,* to simultaneously send and receive signals from the robot and perform the IMU MoCap algorithm. In the sensor integration layer, the corresponding interfaces of the sensor hardware resources are made available to the controller for using the sensor signals. The C++ SDK of Motion Shadow suit is customized in a ROS package to be compatible with the

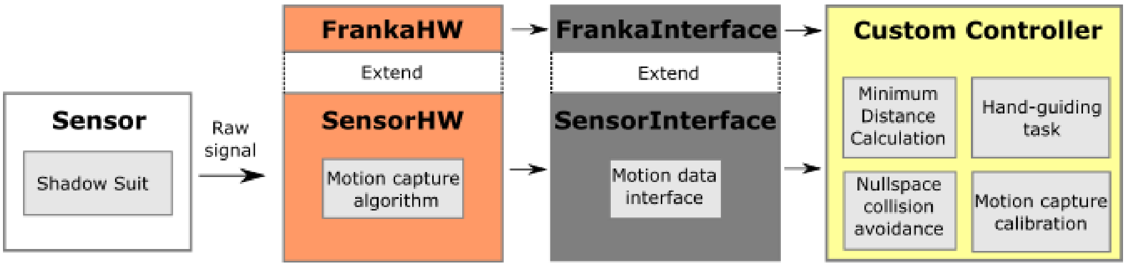

Figure 1 *Ros_control framework integration for peripheral sensors*

ros_control framework. These data are shared with an additional controller which provides a user interface for executing the MoCap sensor-to-segment calibration and the integration with the robot coordinate system. The system integration structure is shown in Figure 1 .

4.2 Calibration of IMU MoCap system in robot frame

The IMU MoCap algorithm, described in Chapter 2, returns the position of each body coordinate system (BCS) into the virtual coordinate frame (VCS). The IMU MoCap position estimations need to be referenced to the robot coordinate system (RCS) to implement the collision avoidance strategy. The robot mounts on a flat surface parallel to the human standing ground, and the RCS has the z-axis pointing up. For a simple calibration set-up, we chose the T pose as the reference pose for both the sensor-to-segment calibration and for defining the relative rotation and translation between the human and the robot. In this position, all BCSs and VCS have identical orientations and different origins located at the distal end of each body segment, the z-axis pointing against gravity, the x-axis to the anterior direction, and the y-axis defined according to the right-hand convention. To align VCS and RCS, the human positions the left hand attached to the handle without grabbing it during the T-pose calibration. The operator faces along the RCS x-axis with the help of markers on the floor. Thus, the relative orientation between the human and the robot, $\boldsymbol{q}_{RCS}^{VCS}$, is a known rotation of 180 degrees along the z-axis. Figure 2 shows the calibration position above-mentioned.

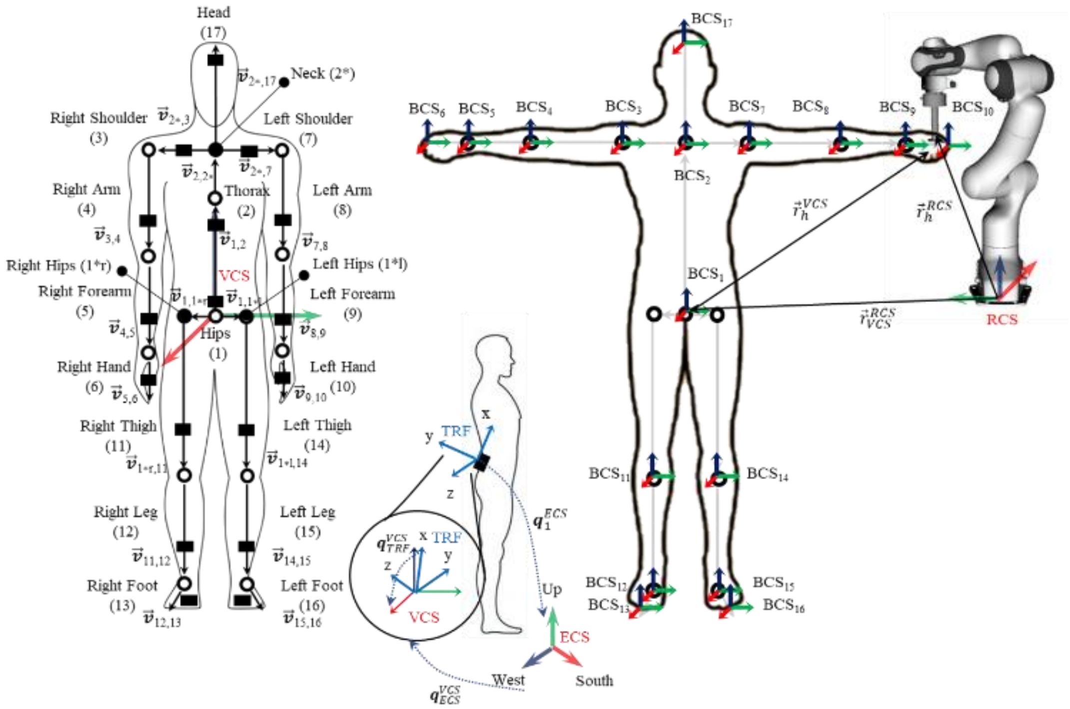

Figure 2 Left: Biomechanical model and coordinate system definition for the IMU MoCap algorithm, right: schematical representation of the human position and robot during the calibration phase

Thus, the displacement between VCS and RCS, $\vec{\boldsymbol{r}}_{RCS}^{VCS}(t)$, is the difference between the guiding hand position $\vec{\boldsymbol{p}}_{hand}(t)$ and robot EE position. Based on $\boldsymbol{q}_{RCS}^{VCS}$ and $\vec{\boldsymbol{r}}_{RCS}^{VCS}(t)$, a homogeneous transformation matrix $\boldsymbol{T}_{RCS}^{VCS}(t)$ is constructed. The body position with respect to RCS, $\vec{\boldsymbol{p}}_{RCS_i}(t)$ is obtained as:

$$[\vec{\boldsymbol{p}}_{RCS_i}(t)] = \boldsymbol{T}_{RCS}^{VCS}(t)\,[\vec{\boldsymbol{p}}_i(t)] \quad (1)$$

where $[\cdot]$ is the homogeneous representation of the 3D vector $\vec{\boldsymbol{p}}_i(t)$, which defines the position of the human segment in the VCS.

4.3 Robot Control Strategy

The Franka robot was controlled in torque mode, assigning the following commands to the joints:

$$\boldsymbol{\tau}_c = \boldsymbol{\tau}_{task} + \boldsymbol{\tau}_{nullspace} \quad (2)$$

$\boldsymbol{\tau}_{task}$ is the torque command in the joint space, to compensate robot gravity and joint friction, thus assuring an effortless manual guidance. $\boldsymbol{\tau}_{nullspace}$ is the command in the null space maximizing the distance between the robot and the human body without causing any wrench on the EE. Then, the corresponding velocities are sent, which are then converted to torques by the inner control loop of the robot controller.

Following the approach presented in Khatib [10] and Ficuciello et al. [11], $\boldsymbol{\tau}_{nullspace}$ is determined as:

$$\boldsymbol{\tau}_{nullspace} = k(\boldsymbol{I} - \boldsymbol{J}^T \boldsymbol{J}^{T\dagger}) \frac{\partial w}{\partial \boldsymbol{q}} \tag{3}$$

where w is the distance cost function, containing the distance between the robot and the human body estimated based on the data from the MoCap system, $\boldsymbol{q}$ is the vector of joint variables, $\boldsymbol{I}$ is the identity matrix of dimension 7 (number of links of the robot), $\boldsymbol{J}$ is the Jacobian of the robotic arm, † is the pseudo-inverse operator and k is a user-defined gain, needed to regulate the magnitude of $\boldsymbol{\tau}_{nullspace}$. In this work, k is extended as a sigmoidal function on the distance to have a smooth activation of the null-space collision avoidance:

$$k = h\left(1 + e^{s(w - w_{middle})}\right)^{-1} \tag{4}$$

where h is a gain constant, s is the steepness, and w_{middle} is the middle point of the sigmoidal (i.e., the point in which the value of the sigmoidal is 0.5). The values for h, s and w_{middle} were empirically set as 3 N, 30 m^{-1} and 0.6 m by trial-and-error tuning. To decrease the computational burden in calculating w, the following approximations are made: the robot is schematized as two main segments, one from the origin of the reference frame of the second joint to the origin of the reference frame of the fourth joint and the other one from the origin of the reference frame of the fourth joint to the origin of the reference frame of the sixth joint. The reference frames are defined according to the Denavit-Hartenberg convention, as shown in Figure 3. In addition, for the human body, only the right arm is considered, because in the hand-guiding application under consideration, it is most likely that collisions may happen with the right arm, considering the structure of the robot and the fact that the end-effector is grabbed with the left hand. Consequently, three segments are considered for the right arm, namely those connecting the right shoulder, elbow, wrist and terminal hand points, whose positions by the IMU MoCap system.

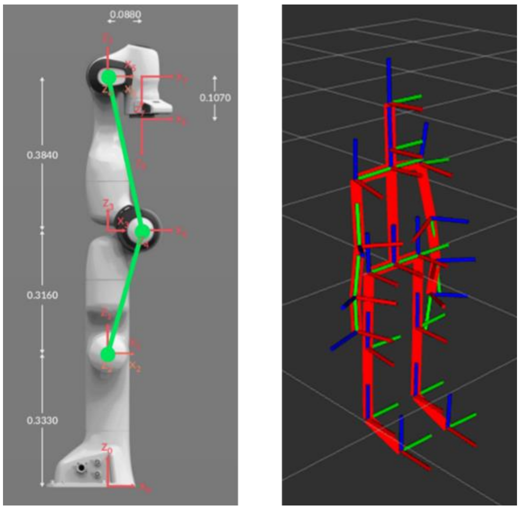

Figure 3 *Left: Schematic representation of the three robot segments, right: visualization of the human model in RViz*

The minimum distance between the human right arm and robot is obtained by calculating the minimum distance between pairs of segments based on the method introduced in [12].

4.4 Results

A simple test was performed to validate the approach described in this work. After the calibration phase, the operator grasps the guiding handle with the left hand and approaches with the right hand the robot elbow point. The null-space command drives the robot to avoid contact with the human right arm without affecting the EE. **Errore. L'origine riferimento non è stata trovata.** presents these

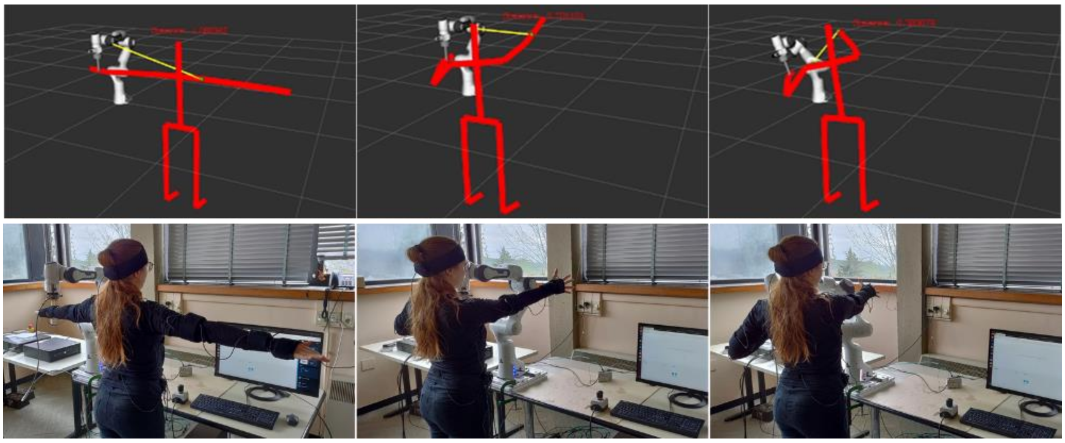

Figure 4 *Pictures of the real world and RVIZ scene for the three phases of the test*

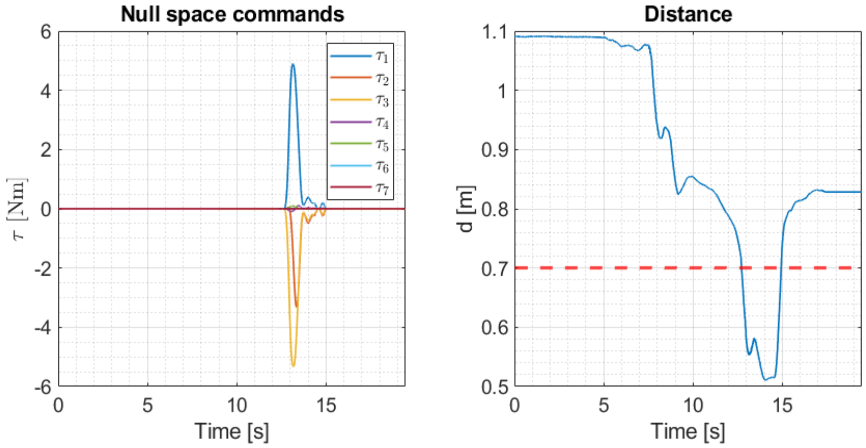

__Figure 5__ Plots of the null space commands of the joints and of the estimated distance between the robot and the operator during the test

test phases both in the real-world scene and in the corresponding RViz (a 3D visualization tool in ROS) virtual scene. In the RViz scene, a simple human skeleton (red segments) was visualized based on the joints/extremes position of MoCap results, while the minimum distance between robot structure and human right arm is highlighted as a yellow segment. Figure 5 presents the recorded null-space commands and the distance between the robot and the arm. At the beginning of the test, $\boldsymbol{\tau}_{nullspace}$ is not active since Equation 11 has a value close to 0 with a large distance. When the distance decreases below 0.7 m as the human operator approaches the robot with her right arm, $\boldsymbol{\tau}_{nullspace}$ starts to increase significantly, since the sigmoidal function rises from near zero. In this test, this activated $\boldsymbol{\tau}_{nullspace}$ had command values mainly on the first, second and third joints to generate a motion in the joint space that drove the robot's links away from the right arm with minimal effect on the end effector.

In conclusion, this work shows that the proposed system integration and IMU MoCap algorithm are effective in collision avoidance scenarios for hand-guided redundant cobots. Moreover, the integration scheme allows the entire system to work under relatively high frequencies (1kHz for robot control and 100Hz for motion capture) with peripheral sensors. The proposed MoCap algorithm, although involving several degrees of simplifications, is easy to implement and can be extended by using more sophisticated calibration methods, or even including additional sensors to correct the pose estimation error. The suggested control strategy that resolves collision avoidance in the null space, can also be used to avoid joint limits and singularities. In addition, the redundancy of cobot is particularly useful not only for collision avoidance but, more generally, for hand-guiding HRI applications to improve the user effectiveness and experience. More redundant degrees of freedom can be introduced to allow more complicated control strategies in the null space.

References

[1] F. Ficuciello, A. Romano, V. Lippiello, L. Villani, e B. Siciliano, «Human Motion Mapping to a Robot Arm with Redundancy Resolution», in *Advances in Robot Kinematics*, J. Lenarčič e O. Khatib, A c. di Cham: Springer International Publishing, 2014, pp. 193–201. doi: 10.1007/978-3-319-06698-1_21.

[2] L. Sabatino Scimmi, M. Melchiorre, S. Mauro, e S. Pastorelli, «Multiple Collision Avoidance between Human Limbs and Robot Links Algorithm in Collaborative Tasks»:, in *Proceedings of the 15th International Conference on Informatics in Control, Automation and Robotics*, Porto, Portugal, 2018, pp. 291–298. doi: 10.5220/0006852202910298.

[3] C. Byner, B. Matthias, e H. Ding, «Dynamic speed and separation monitoring for collaborative robot applications – Concepts and performance», *Robotics and Computer-Integrated Manufacturing*, vol. 58, pp. 239–252, ago. 2019, doi: 10.1016/j.rcim.2018.11.002.

[4] D. Mronga, T. Knobloch, J. de Gea Fernández, e F. Kirchner, «A constraint-based approach for human–robot collision avoidance», *Advanced Robotics*, vol. 34, fasc. 5, pp. 265–281, mar. 2020, doi: 10.1080/01691864.2020.1721322.

[5] F. Flacco, T. Kroger, A. De Luca, e O. Khatib, «A depth space approach to human-robot collision avoidance», in *2012 IEEE International Conference on Robotics and Automation*, Saint Paul, MN, mag. 2012, pp. 338–345. doi: 10.1109/ICRA.2012.6225245.

[6] L. S. Scimmi, M. Melchiorre, S. Mauro, e S. P. Pastorelli, «Implementing a Vision-Based Collision Avoidance Algorithm on a UR3 Robot», in *2019 23rd International Conference on Mechatronics Technology (ICMT)*, SALERNO, Italy, ott. 2019, pp. 1–6. doi: 10.1109/ICMECT.2019.8932105.

[7] L. Pérez, Í. Rodríguez, N. Rodríguez, R. Usamentiaga, e D. García, «Robot Guidance Using Machine Vision Techniques in Industrial Environments: A Comparative Review», *Sensors*, vol. 16, fasc. 3, p. 335, mar. 2016, doi: 10.3390/s16030335.

[8] A. Amorim, «Robust human position estimation in cooperative robotic cells», *Robotics and Computer Integrated Manufacturing*, p. 10, 2021.

[9] M. Safeea, «Minimum distance calculation using laser scanner and IMUs for safe human-robot interaction», *Robotics and Computer Integrated Manufacturing*, p. 10, 2019.

[10] O. Khatib, «Real-time obstacle avoidance for manipulators and mobile robots», in *Proceedings. 1985 IEEE International Conference on Robotics and Automation*, St. Louis, MO, USA, 1985, vol. 2, pp. 500–505. doi: 10.1109/ROBOT.1985.1087247.

[11] F. Ficuciello, L. Villani, e B. Siciliano, «Variable Impedance Control of Redundant Manipulators for Intuitive Human–Robot Physical Interaction», *IEEE Trans. Robot.*, vol. 31, fasc. 4, pp. 850–863, ago. 2015, doi: 10.1109/TRO.2015.2430053.

[12] M. Safeea, N. Mendes, e P. Neto, «Minimum Distance Calculation for Safe Human Robot Interaction», *Procedia Manufacturing*, vol. 11, pp. 99–106, 2017, doi: 10.1016/j.promfg.2017.07.157.

Chapter 5

Method for automatic scaling knee joint models from optical markers using PCA

Musculoskeletal modelling is a powerful technique for investigating the complexity of human movements through computer simulation. As shown in the previous Chapters, these models are not only purely theoretical tools, but have both clinical and industrial applications. This wide field also justifies the different types of models proposed: from general to specific ones, from very accurate for the best results to more simplified for the lower computational time, as also discussed previously in this Thesis.

Considering general models, the most used multibody software for musculoskeletal simulations are OpenSim and AnyBody Modelling System. Subject-specific variables, such as joint surfaces or muscle parameters, can be modified easily to explore both healthy and pathological movement patterns [1], [2], determine muscle force contribution [3], and define neuromusculoskeletal cause-and-effect relationships [4]. Also in this context, the literature gathers various musculoskeletal models characterized by different joint kinematics, muscle reduction and direction of force, resolution strategies, and more in general, different levels of details. For example, among other aspects, knee models vary for DoF number, geometries, and the presence of cartilage and ligaments. The simplest OpenSim knee model is a hinge joint with 1 DoF [5], where the flexion rotation is the independent variable, and the additional two rotations and three translations of the tibia relative to the femur are coupled to it. However, hinge-based knee models cannot correctly estimate motion of secondary DoFs. To improve the accuracy of the simulation, knee models can be extended to more complex planar and spatial parallel mechanisms [6]–[8], constrained by the ligaments' length and articular contacts.

The ideal approach is to use CT or MR images to create patient-specific geometries and identify menisci, cartilage, and ligament geometries [9]. The effect of including patient-specific images in the simulation workflow has received growing attention among researchers [10]–[12], who claim that MRI-based models produce more physiological kinematic solutions, reducing the impact of anatomically inaccurate joints and soft-tissue artifacts. MRI can be considered non or minimally invasive with respect to other imaging techniques, which require radiation exposure or more invasive procedures. Moreover, it may allow good imaging of soft tissues too. Nevertheless, it is a long and expensive analysis and its postprocessing is laborious and time-consuming. Moreover, MRI scanners are not always accessible in clinical scenarios and have limitations on a global scale. That is why the development of generic knee model scaling strategies based on patient-specific anthropometric measurements or more inexpensive experimental data might provide a more translatable clinical tool, in particular for the analysis of large cohorts [9].

The scaling strategy of OpenSim and Anybody combines measured distances between the 3D coordinates of markers' location and manually specified scale factors, such as subject height and weights. The dimension of each human segment is corrected with a set of virtual markers placed in the unscaled model in the same anatomical locations as the experimental markers. Masses and inertia tensor of each segment depends on mass-fat scaling factors different for each software. This scaling strategies are optimized for the joint models used in this general software.

Our objective is to develop a method that scales the parameters of a knee model based on the envelope of tibiofemoral configurations that minimize the peak contact pressure [13], [14]. The model has been already applied in musculoskeletal models with very good results [13]. In that previous study the patient MR images were used to obtain the model geometry, and the corresponding model based on the congruency of the articular surfaces. The idea in this case is trying to obtain sophisticated knee model's results without MRI, thus defining the model parameters only from experimental marker data and anthropometric measurements. If the technique proves successful, it can be extended to obtain a more accurate full-body model also for the applications described previously in this Thesis, where it has already been shown the importance of having fast and accurate procedures for a practical industrial use.

This work is in collaboration with Prof. Daniel Benoit of the University of Ottawa and the Children's Hospital of Eastern Ontario (CHEO), which provides us with eleven MRI images and experimental markers set of adolescent patients with a primary ACL injury. Additional MRI images will be processed and segmented by Prof. Benoit group, but they were not available for the time frame of the project and are not used here. The MRI images include only the knee joints, with a span of about 200 mm centred in the middle of the knee, with a section of the distal femur, proximal tibia and fibula bones. This group of images is used to define the scaling model which will be used to scale the knee model on other patients. Seeing the limited number of patients available now, the scaling model study is preliminary, but the technique can be informed with any number of additional MRI data.

To build the scaling model, an automatic procedure is devised for determining the anatomical coordinate system of the partial femur and tibia from MRI, correlated to the coordinate system of the full bones. This is also necessary for the knee model definition and for correlating the MRI images with the marker set. Since the two anatomical coordinate systems, i.e. the one from MRI images and the one from the markers, are not perfectly consistent, due to the different information associated to MRI and markers, the misalignment between each pair of coordinate systems are determined using full-leg images from a different study. The misalignment is a correcting factor for properly positioning the partial knee bones and the corresponding knee model into the marker data set.

The knee model features a simplified representations of knee articular contact from adolescent MRIs for the medial/lateral components of the femur and tibia. The knee model parameters, expressed in the marker coordinates systems, the marker coordinates and anthropometric measurements, defined on the eleven patients, feed a Principal Component Analysis (PCA) method. The scope of the PCA is to predict outcomes from sparse datasets, and its performance is estimated by considering different combination of geometrical features and anthropometric data. Details of the method and results are presented and discussed in this Chapter.

5.1 Automatic Reference Frame definition

The automatization of coordinate system definition from anatomical images is a powerful strategy to drastically reduce the process-time for each subject. For the present study, this automatization is useful to create the scaling model from a large cohort. However, it is worth noting that the same procedure can be used to simplify the implementation and use of the knee model for those patients who must undergo an MRI. For these patients, no scaling is required but the model still needs to be identified from MRI images and aligned on marker data.

One easy implementation to define the axis of long bones is to calculate the line passing through the centroids of small slices of bones. The long-bone axis (L') is thus obtained by computing the centroids of 40 slices of 2 mm, starting from approximately 100 mm from the distal condyle surface. The choice of these parameters will be motivated lately. The coordinates of the best-fit line through slices' centroids are identified using singular-value decomposition, and named as L' which points proximally. Moreover, a common approach uses two spheres to approximate the femoral condyle surface, and this has also been used in some knee models [6]. Similar to other methods described in the literature [15], [16], the femur Z_f axis, defined usually as cylindrical axis, is chosen as the line connecting the centre points of the sphere pointing laterally both for the right and left knee, thus normalizing the difference between right and left knee. The automatic coordinate system of the femur, calculated using custom-MATLAB script (R2020a, MathWorks, Natick, MA), is reported in Table 1.

Table 1 *Femur MRI coordinate system definition*

Automatic definition of femur coordinate system	
Z_f	Vector through centre points of the 2 spheres, pointing laterally
X_f	$X_f = L' \wedge Z_f$ for right legs, $X_f = Z_f \wedge L'$ for left legs
Y_f	$Y_f = L' \wedge X_f$ for right legs, $Y_f = X_f \wedge L'$ for left legs
O_f	Midpoint between the spheres' centre points

Table 2 *Tibia MRI coordinate system definition*

Automatic definition of tibia coordinate system	
Y_t	$Y_t = L''$
X_t	$X_t = Y_t \wedge B'$for right legs, $X_t = B' \wedge Y_t$ for left legs
Z_t	$Z_t = X_t \wedge Y_t$ for right legs,$Z_t = Y_t \wedge X_t$ for left legs
O_t	Projection of O_f on Y_t

Similarly, for the tibia, the vector pointing laterally between the centroids of the tibia plateau points (B'), and the long bones axis (L'') defined like in the femur, are used to define the tibia coordinates system (Table 2).

5.2 Standard Reference Frame definition

The International Society of Biomechanics (ISB) proposes guidelines to define the coordinate systems of bones and joints. Specific body coordinate systems, identified by markers' positions and manual palpation, describe the bone motion. Specifically for the tibia-femoral joints, the femoral and tibial coordinate systems are listed in [20]. The orientation definition of the tibia with respect to the femur follows the ZXY Euler angle sequence, as reported in [18].

According to the ISB recommendation, the femoral coordinates system depends on the Hip Joint Centre of rotation (HJC). Since its localization through direct markers is not feasible, empiric approaches have been widely tested and studied. ISB recommends using a "functional" approach, where the subject performs several leg movements [19] and the HJC is defined as the centre of the best-fit sphere described by the trajectories of the thigh's markers cluster. However, if the patient cannot perform any movement, the HJC is estimated thanks to “prediction” methods that use regression equations and anthropometric measurements. Several researchers evaluated the accuracy of different algorithms. They compared the prediction values with measurements obtained by roentgen stereophotogrammetric analysis [20], or with medical imaging techniques, such as X-ray images [21] and MRI [22], which are considered the gold standard with errors as small as 2 mm. A recent systematic review [23] identified a total of 11 “predictive” methods and 13 different “functional” procedures and claims that among the predictive ones, the Harrington equation [22] shows the best accuracy under ideal conditions. However, the error in using this equation is still 3-6 mm higher than the functional approach. Thus, it is convenient to define a reference system with all the anatomical points palpable.

The objective is to correctly refer to the anatomical reference system defined by the experimental skin markers in the MRI images. Thus, the aim is to study the average misalignment between the three axes of the automatic reference frame and an anatomical coordinate system identified with the experimental markers set. It is convenient to define a reference system using anatomical points that are palpable and easily identifiable, like those used with skin markers, and similar to standard anatomical reference systems. For example, the greater trochanter of the femur is easily perceptible and addressed with a marker during experimental data. The custom anatomical reference system for the femur is reported in Table 3. Regarding the tibia reference system, it is defined following the ISB guidelines:

Table 3 *Femur coordinates system definition*

Custom femur coordinate system	
X_{Cf}	Perpendicular to the plane defined by the lateral and medial epicondyles and the greater trochanter, pointing anteriorly
Z_{Cf}	Connecting lateral and medial epicondyle, pointing laterally
Y_{Cf}	$Y_{Cf} = Z_{Cf} \wedge X_{Cf}$, for right leg, $Y_{Cf} = X_{Cf} \wedge Z_{Cf}$, for left leg
O_{Cf}	Midpoint between the epicondyle points

Table 4 Tibial coordinates system definition

Tibial coordinate system	
X_{Ct}	Perpendicular to the plane defined by the lateral and medial malleoli and midpoint between the tibia plate, pointing anteriorly
Y_{Ct}	Connecting the midpoint of malleoli and midpoint of tibia plate, pointing proximally
Z_{Ct}	$Z_{Ct} = X_{Ct} \wedge Y_{Ct}$, for right leg, $Z_{Ct} = Y_{Ct} \wedge X_{Ct}$,for left leg
O_{Ct}	Projection of femur centre into Y_{Ct}

5.3 Misalignment between the two systems

Computing the misalignment between the automatic reference frames and the standard ones is important for setting the correct position of the two bones in the marker set-up. A more accurate localization reduces the overall error in the definition of musculoskeletal models, joint axis alignments, and kinematic evaluation. It is also fundamental to study the correlation with the anthropometric data and to setup the scaling model.

5.3.1 Material and Methods

Data on the full legs of seven subjects obtained from previous studies [26-28] are used to define the misalignment. Since these data were described in previous publications, only a brief description of the experimental protocol is reported here. Each leg was scanned using standard CT (STCT) (Brilliance CT 16-slice system, Philips Healthcare), and 3.0 Tesla MRI (MRI 3 T; 3T MR750W GEM ENAB, GE). Details of image scans are listed in [24]. From each scan, 3D models of the entire bones of the femur, tibia, and fibula are obtained by a semi-automatic segmentation process using Medical Imaging Interaction Toolkit (MITK software 2003–2021, German Cancer Research Centre DKFZ). For each subject two pairs of reference systems are defined: 1) the automatic reference frame using the femur and tibia bones cut almost at 100 mm from the knee joint flexion axis, and 2) the standard reference frame obtained by the full bones' images. Identification of anatomical points and best-fitting spheres is performed in Geomagic Studio 2012.

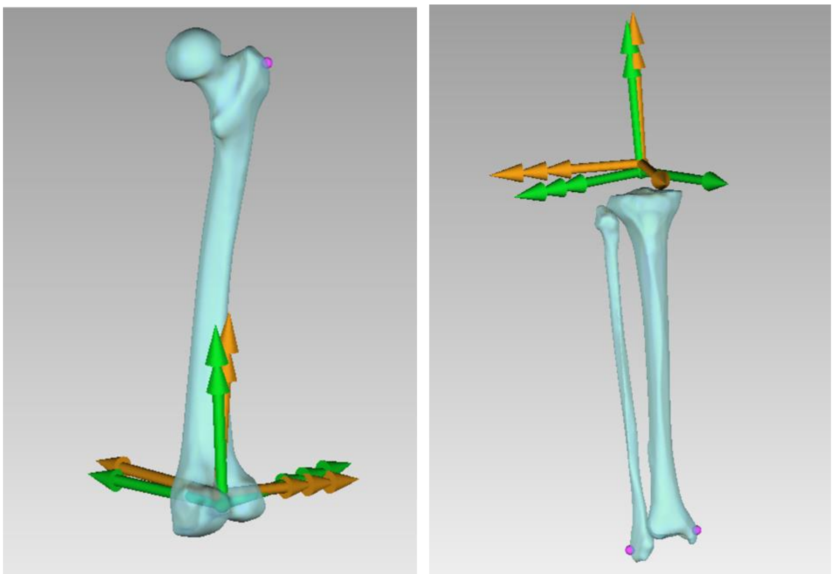

Figure 1 *Femur(left) and tibial (right) coordinates systems. The orange tern is the results of the automatic definition. Green one corresponds to the marker definition*

The measure of the distance (positions and orientation) between reference systems is performed through a recent metric based on platonic solids [25]. A sensitivity study determined the minimum number of slices to stabilize the automatic long axis definition algorithm. Then, the variability of the misalignment between the pair of coordinate systems is obtained and the mean value is computed using the quaternion mean formalism [26]. This mean misalignment denotes a constant error between the automatic reference frame definition and the standard one and is a representative parameter for correcting the bone alignment with respect to the markers' dataset.

5.3.2 Results

The sensitivity analysis results to define the minimum bone length to have a stable definition of the long axis and, consequently, of the anatomical reference frame are shown in Figure 2. It displays the measure of the differences, defined with the platonic solid formalism, between the automatic reference frame and the standard reference frame definition: a small value means that the differences are

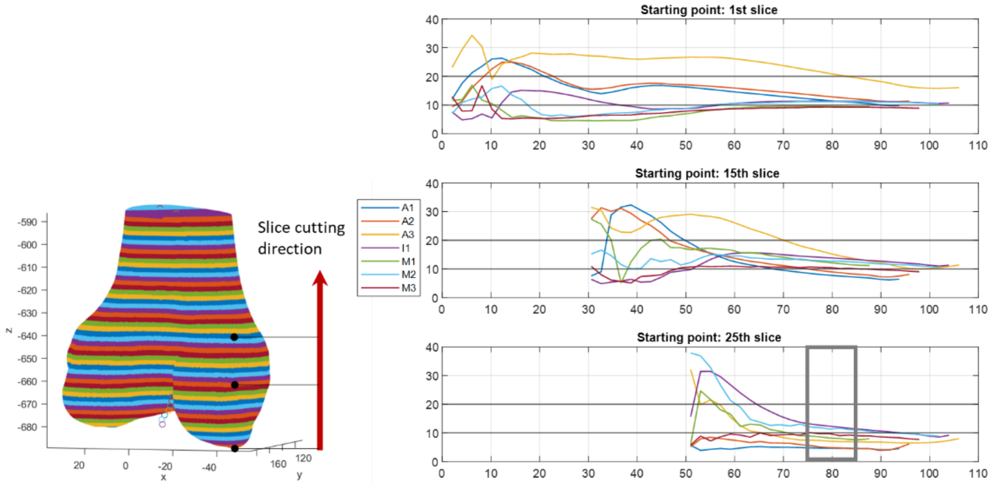

Figure 2 Stability analysis of the automatic reference definition over the cutting slice

small in terms of both orientation and position of the origin of the coordinate system. Each curve is a different subject. Since the automatic algorithm computes the long axis using all the slices analysed, the figure shows the attitude difference starting from 1) the lowest point of the femoral condyle, 2) 30 mm higher than the lowest point, and 3) 50 mm higher, almost at the beginning of the femoral diaphysis. The third case reaches stability faster and with a lower value of misalignments. In particular, the mean of the seven test cases after 80 mm cuts is equivalent to 12.40, 11.64, and 8.33 mm in the three cases. Thus, to have a better axis definition, it is necessary to consider only the femoral diaphysis and cut out the centroids obtained in the epiphysis. Moreover, 80 mm of the femur is sufficient to stabilize the axis detection algorithm and define a meaningful anatomical reference coordinate system.

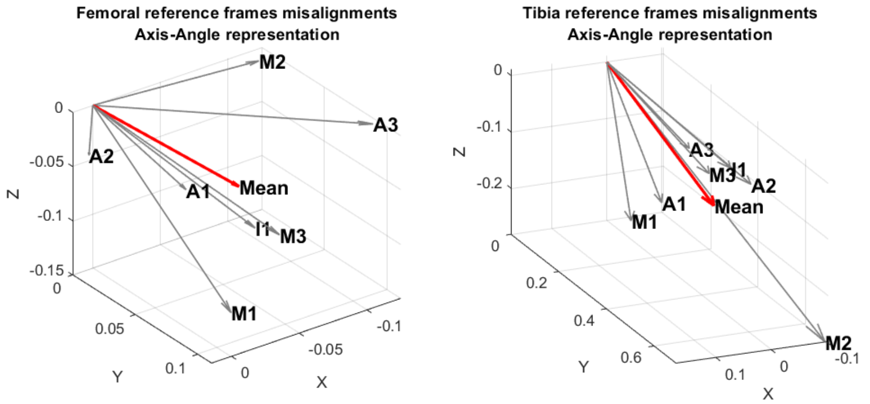

Figure 3 Axis-angle representation of the misalignments between the two coordinate systems of the 7 analysed subjects

Table 5 Results of the femur and tibial misalignments in quaternion formalism

Mean femoral misalignment	
Orientation	$\boldsymbol{q}_f = (-0.9989, 0.0223, -0.0344, 0.0218)$
Position	$\boldsymbol{p}_f = (-6.4331, -3.2410, 0.5945)$
Mean tibial misalignment	
Orientation	$\boldsymbol{q}_t = (-0.9613, 0.0215, -0.2729, 0.0324)$
Position	$\boldsymbol{p}_t = (1.5436, -5.3269, 0.4470)$

The same considerations are valid for the tibia. These conditions are assumed hereinafter.

Figure 3 gathers the visual representation of the rotation that transforms the automatic reference frame into the standard one: the vector direction corresponds to the axis of rotation, whereas the vector magnitude is the angle of rotation. The mean value of the orientation is defined by a quaternion (**q** = (q_0, q_1, q_2, q_3)) and the position (**p** = (p_x, p_y, p_z)) as the mean of the 3D coordinates of vectors among the seven subjects. These terms, for the femur and tibia, are listed in Table 5. These values are used to correct the preliminary alignment of the femur and tibia on the markers experimental data, whose procedure will be described in the next section.

5.4 Automatic alignment of knee MRI images in experimental marker dataset

An automatic procedure for aligning the partial knee MRI images into the experimental marker set is necessary to correlate the coordinates of the knee model with the marker and anthropometric information. In this phase, from each MRI image, the automatic reference frame of both the tibia and femur is detected and corrected with the corresponding misalignments estimated in the previous Section. Even if the population of this study is adolescent and differs from the previous one, which is more mature, it is possible to suppose that the mechanical axis of both the femur and tibia doesn’t change much after childhood.

5.4.1 Material and Methods

Datasets consist of the images of eleven ACL-injured participants recruited from the Children's Hospital of Eastern Ontario (CHEO) and the University of Ottawa. Inclusion criteria included primary ACL injury and no history of major lower limb injury prior to study enrolment. Participants are chosen using the Tanner stages of pubertal development [27], [28]. To create a wide range of adolescents, one male and one female subject from each Tanner stage is selected wherever possible. Mean values of the participant are (age: 15.42 ± 1.4, height: 165.8 ± 6.5 cm, weight: 67.35 ± 15.6 and tanner stage: 3.92 ± 1.2).

For each participant, a multiplanar sequence of MR images is collected at 1.5 T, repetition time/echo time 1400/17 ms, field of view equal to 160 mm, and slice thickness of 0.8 mm (Siemens Magnetom Skyra, Siemens Healthineers AG, Germany). Sagittal, coronal, and axial views of proton density (PD) cube-weighted scans are used to segment the distal third of the femur, the proximal third of tibia and fibula, and the medial and lateral menisci (Workbench 2018.04.2, MITK, Germany). Moreover, each participant performs an experiment with a whole-body cluster set with a hybrid protocol [33] consisting of 84 markers shown in Figure 4. Data are collected at 100 Hz by a 10-camera motion capture system (6 MX and 4T series, Vicon, UK). The automatic alignment procedure consists firstly of the definition of the femur and tibia reference system using the experimental marker

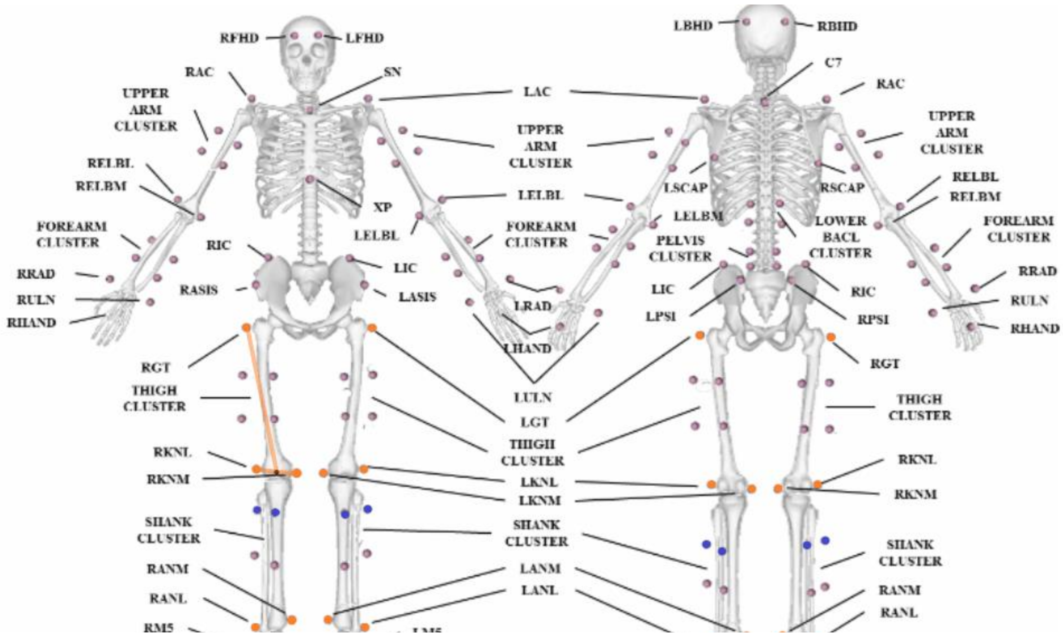

Figure 4 Custom marker set used in the experimental phase

***Table 6** Femur marker coordinate system definition*

Marker coordinate system on the femur	
X_{Mf}	Vector pointing anteriorly of the plane defined by (R)GT, (R)KNM and (R)KNL
Z_{Mf}	Vector pointing laterally connecting (R)KNM and (R)KNL
Y_{Mf}	$Y_{Mf} = Z_{Mf} \wedge X_{Mf}$
O_{Mf}	Middle point between (R)KNM and (R)KNL

***Table 7** Tibial marker coordinate system definition*

Marker coordinate system on the tibia	
X_{Mt}	Vector pointing anteriorly of the plane defined by O_{Mf} , (R)ANL and (R)ANM
Y_{Mt}	Vector pointing up connecting O_{Mf} and the middle point of (R)ANL and (R)ANM
Z_{Mt}	$Z_{Mt} = X_{Mt} \wedge Y_{Mt}$
O_{Mt}	O_{Mf}

set. The markers, highlighted in orange in Figure 4, are necessary to construct the reference system as in Table 6 and 7.

Since the relative position of the femur and tibia is unknown during the marker experiments and differs from the one captured during the MRI, the alignment procedure consists of three steps:

1. Aligning the MRI automatic definition of the femur coordinate system corrected by the mean femoral misalignment to the marker one
2. Correction of the marker tibial coordinate system with the tibial mean misalignment
3. Aligning the MRI tibia coordinate system to the corrected marker one through an optimization process that minimizes the error between the two, moving the tibia within its range of motion, calculated using a validated procedure [29]. Specifically, for every tibia flexion angle from 0°

to 130°, an optimization algorithm maximizing joint congruence, determines the five coupled motion components of the tibia with respect to the femur.

The optimization problem minimizes a measure of the distance between two spatial rigid-body poses [25], called platonic distance. It measures the root mean square (RMS) distance between corresponding virtual points in the two reference systems, placed on the vertices of a platonic solid with radius R. Equivalently, it defines the same RMS distance for any equally spaced and homogeneously distributed points on a sphere. Defining $\boldsymbol{o}_k^j$ as the position vector between the origin of the j-th and the k-th reference systems, and $\boldsymbol{R_{jk}}$ as the relative rotation matrix between the two, the platonic distance d_p is equal to:

$$d_p = \sqrt{\left|\boldsymbol{o}_k^j\right|^2 + 2R^2\left(1 - \frac{tr(\boldsymbol{R_{jk}})}{3}\right)} \tag{1}$$

where $tr(*)$ is the trace of the matrix inside the brackets, and R is the radius of a sphere centred in the body reference systems and circumscribed to a regular polyhedron, that defines the intrinsic weight for the rotational part. R is chosen taking a sphere that approximatively envelopes the knee. In particular $\boldsymbol{R_{jk}}$ and $\boldsymbol{o}_k^j$ are computed between the corrected marker tibial coordinate system and the MRI tibia reference system. The position and orientation that minimize the value of d_p correspond to the tibia reference system with respect to the marker frame. In this way it is possible to determine the relative pose of the femur and tibia consistent with the anatomy and kinematics.

5.4.2 Results

The positions of 5 markers define the marker experimental coordinate systems. The same procedure is performed for the eleven participants, using as input the markers gathered during a static stand-up session. The MRI image of the tibia-femoral joint is correctly positioned for 9 participants, but the positioning fails for 2 cases because the markers of RANL or RANM (see Figure 4) are absent in the marker datasets. Figure 5 shows the results obtained.

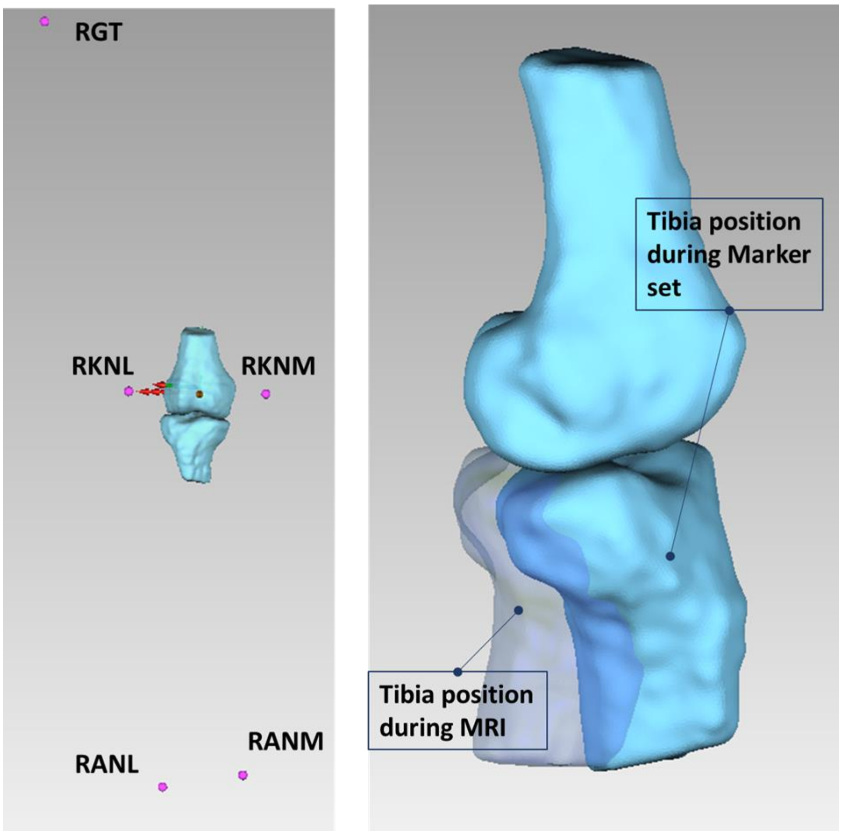

Figure 5 *(left) Alignment of the partial knee in the marker reference systems (right) Relative position of the tibia with respect to the femur during the MRI acquisition and marker experimental set-up*

The position of the markers of the tibia and femur are also used to define the tibial-femoral joints angle in the experimental pose. The mean flexion angle and the standard deviation among the nine knees at the static pose is (10,22 ± 11,28)°. The mean value is consistent with the flexion angle found in literature in the standing position. The standard deviation is high due probably to some factors. The anatomical reference systems from MRI are defined automatically and then corrected to match a modified anatomical reference system, as previously described: the difference with a more standard definition could lead to residual flexion angles depending on the participant. Moreover, there could be intrinsic errors in the markers' position. In addition, the population of the study is adolescents with ACL injuries, and there are no specific studies evaluating the flexion angle in standing position for comparison. However, the results obtained with this procedure seem visually correct. It is a promising tool for aligning partial bone images to experimental marker sets in a more complex biomechanical system using both markers' positions and model-based joint motion predictions.

5.5 PCA

Principal Component Analysis (PCA) decomposes shapes, described by a given number of parameters, into discrete vectors called modes, which represent a basis of principal components in the parameter space. It approximates data $\boldsymbol{x}$ (namely, the parameters of a population) as the sum of its mean values $\overline{\boldsymbol{x}}$ and the weighted sum of n principal components $\boldsymbol{b}_i$ [30]–[32]:

$$\boldsymbol{x} = \overline{\boldsymbol{x}} + \sum_{i=0}^{n} a_i \boldsymbol{b}_i \tag{2}$$

The value of n, which can assume the maximum value of the number of subjects, is chosen so that the accumulated variance explained by each component accounts for at least 90% of the total variation in the population. The principal components $\boldsymbol{b}_i$ describe a basis vector that shapes the features of all datasets, whereas a_i, the so-called principal components scores, quantify the contribution of each feature. The way in which the values of these components are estimated can differ. Following the procedure described in [33], if $\boldsymbol{M}$ is the matrix that contains all measurements, and $\boldsymbol{u}$ the mean of each row, the mean-subtracted matrix $\overline{\boldsymbol{M}}$ is:

$$\overline{\boldsymbol{M}} = \boldsymbol{M} - \boldsymbol{u}\boldsymbol{h}^T \tag{3}$$

where $\boldsymbol{h}$ is a vector of ones of length n, equal to columns of $\boldsymbol{M}$. The covariance matrix is:

$$\boldsymbol{C} = \frac{\overline{\boldsymbol{M}}\,\overline{\boldsymbol{M}}^T}{n-1} \tag{4}$$

from which the eigenvectors and eigenvalues are calculated. The eigenvectors are ordered by decreasing eigenvalue and gathered in the matrix $\boldsymbol{V}$ where the first column corresponds to the eigenvector with the largest eigenvalue. Thus, the coefficients a_i, composing the vector $\boldsymbol{a}$ are solved by the system of linear equations:

$$\boldsymbol{a} = \boldsymbol{V}^{-1}(\boldsymbol{M} - \boldsymbol{u}\boldsymbol{h}^T) \tag{5}$$

The matrix $\boldsymbol{V}$ forms a new space that describes the matrix $\boldsymbol{M}$ where the variances of the measures are maximized, and the covariances are zero. The eigenvectors are the principal components of the data set, and the corresponding eigenvalues are the variance of each principal component. Basically, the basis defined by $\boldsymbol{V}$ (or a subset) is assumed to describe any possible component of a population, so that this new space can be used to predict some components of the measures given other components, using both $\boldsymbol{V}$ and $\boldsymbol{u}$ calculated with the full dataset.

Supposing to have a vector $\boldsymbol{d}$ with *m* data that has fewer rows than the matrix $\boldsymbol{M}$, the principal component scores a_i are calculated from (5) substituting $\boldsymbol{M}$ with $\boldsymbol{d}$, the *m* x *n* sub-matrix of $\boldsymbol{V}$ and the first m values of $\boldsymbol{u}$ and $\boldsymbol{h}$**.** Since the reduced $\boldsymbol{V}$ matrix is not square, the matrix inversion is substituted by the matrix pseudoinverse. The pseudo inversion implicates a least square minimization. Then the predicted values are equal to:

$$\boldsymbol{d}^{*} = \overline{\boldsymbol{M}} + \sum_{i=i}^{n} a_i \boldsymbol{V}_i \tag{6}$$

Another procedure, similar to the one described in [34], extracts the principal components scores with a specific optimization problem. In particular, it consists of three stages: 1) deconstructing the predictor variables into principal components, 2) using an optimization problem to predict the principal components scores, and 3) reconstructing the predicted values by the resolution of the linear regression. Since the purpose of the work is to reconstruct the knee model parameters from experimental marker data and anthropometric measurements, the optimization problem for the prediction stages consists of minimizing the distance between the reconstructed marker position of PCA and the anthropometric values, $f(\overline{\boldsymbol{x}}, \boldsymbol{b}_i, a_i)$ function of the positive unknowns a_i, and the experimental positions of the subject to be explored.

$$min \sum_{j=1}^{M} \left| f(\overline{\boldsymbol{x}}, \boldsymbol{b}_i, a_i) - \boldsymbol{p}_j \right| \tag{7}$$

The two approaches slightly differ from each other, and the results are described later.

5.5.1 PCA feature matrix

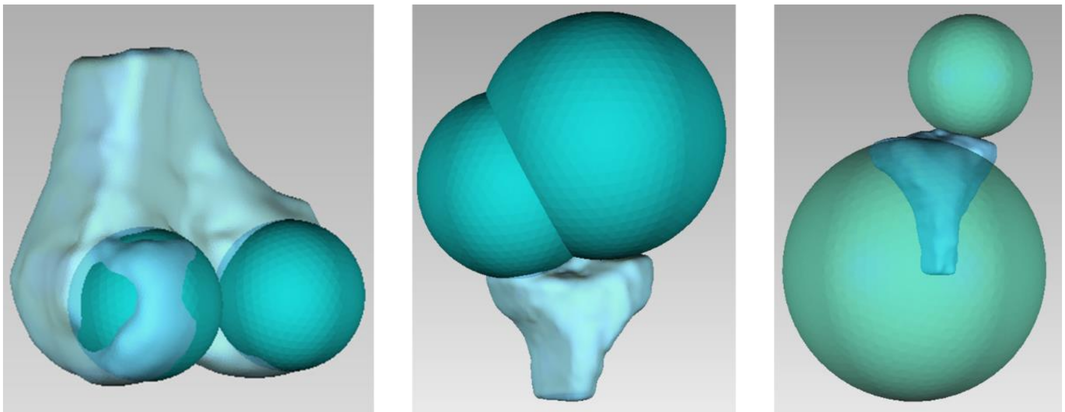

Figure 6 *Spheres that model the condylar surfaces of femur and tibia*

The objective is to use the PCA to scale the geometrical parameters necessary to schematically describe the articular surface and define an advanced knee model given marker data and anthropometric measurements as inputs. The condylar surfaces can be approximated with 1) two planes at the proximal tibia and by two spheres at the distal femur or with 2) two spherical surfaces both for the proximal tibia and distal femur [6], [8].

Each sphere is described mathematically by four parameters: the radius and the vector of centre coordinates. A plane is defined in general by three parameters: for instance, the distance of the plane from the origin and two angles which parametrize the unit vector perpendicular to the plane. However, to have a description of the position of each plane which could be more easily correlated to the overall geometrical features of the tibia, the coordinates of the centre of each tibial plateau are chosen instead of the plane-origin distance, thus obtaining five parameters. With this convention, the numbers of parameters are for:

- distal femur surfaces: 8 parameters
- proximal tibia surfaces: 8 or 10 parameters depending on the approximation used

The PCA is well-defined when the matrix $\boldsymbol{M}$ has column number n , the number of measures, higher than row number m, the number of parameters. In this case, the column number correspond to the MRI images correctly positioned in the marker reference systems and equals 11 for the femur and 9 for the tibia. Thus, the matrix is highly rectangular because it has a number of rows higher than the number of columns, which is not optimal for setting a good PCA feature matrix. The idea is to fill the row matrix with the minimum number of parameters possible, since the present population is low. The minimum number of markers that describe the knee morphology is four: the two markers positioned on the medial and lateral epicondyles and the two proximal markers of the shank, one anterior and one posterior. Thus, the tibiofemoral joint dimensions are defined both in the longitudinal and transverse planes.

For the femur, three different datasets are tested and listed in Table 8. The green colour highlights the known parameters, whereas the orange underlines the one to estimate during the prediction phase. All the points coordinates are referred to the corresponding anatomical coordinate systems defined with markers. The height is measured from the ground to the head top of the subject standing against the wall. The knee width is the length, manually estimated, between medial and lateral epicondyles. The distance, calculated as the sum or differences between the spheres' radius, highly depends on the geometry of the proximal tibia surface, especially the anatomy of the tibia plateau plates.

***Table 8** PCA femur cases*

Case 1	Case 2	Case 3
(R)KNL: Knee Lateral (R)KNM: Knee Medial (R)SHPA: Shank Proximal Anterior (R)SHPP: Shank Proximal Posterior	=	=
Coordinates and Radius of Lateral Femur Sphere	=	=
Coordinates and Radius of Medium Femur Sphere	=	=
	Subject Height	Distance between lateral sphere of femur and tibia
	Subject Knee Width	Distance between medial sphere of femur and tibia

In the analysed data, they were almost flat with convex and concave surfaces depending on the geometry. Therefore, the corresponding sphere could be above or over the knee joint axis. Figure 6 underlines the variation of these spheres' position. The higher variability is in the lateral spheres. Thus, for the distance calculation, if the coupled spheres are on the same side, the sign of the tibia centre coordinates is set to negative. The variability over the sphere's positions returns an unstable PCA analysis, especially for the inability to recognize the relative position between the coupled spheres. Therefore, the convention that describes the tibia with two planes is preferred.

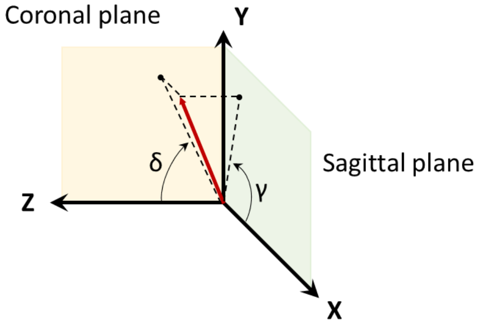

Figure 7 *Projections of the vector over the anatomical planes*

The normal vector $\boldsymbol{n}$ is parameterised using the angle of its projection in the coronal δ and sagittal plane γ:

$$\begin{aligned} \gamma &= atan2(n_y, n_x) \\ \delta &= atan2(n_y, n_z) \end{aligned} \tag{8}$$

To reduce even more the number of parameters for describing the tibia surface, the mean plane between the lateral and medial tibial plane is defined within Geomagic Studio 2012 for all the experimental knees. Figure 8 shows the cited planes.

Similar to the femur analysis, four different datasets for the tibia are tested and listed in Table 9.

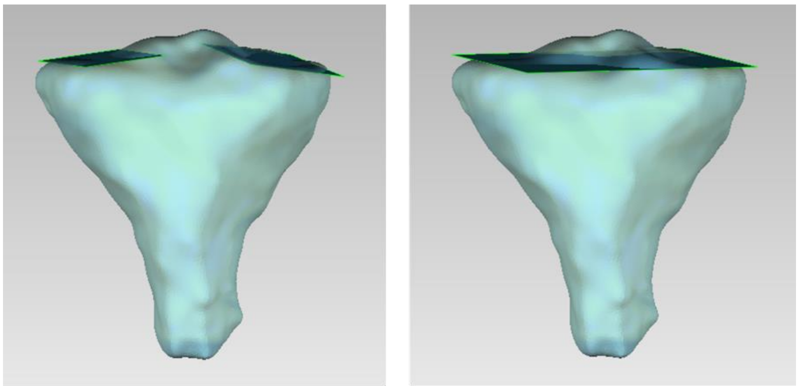

Figure 8 Planes that describe the tibial condyle surface. (left) medial and lateral planes (right) mean plane between the two

Table 9 PCA tibial cases

Case 1	Case 2	Case 3	Case 4
(R)KNL: Knee Lateral (R)KNM: Knee Medial (R)SHPA: Shank Proximal Anterior (R)SHPP: Shank Proximal Posterior	=	=	=
	Coordinates and Radius of Lateral Femur Sphere	Coordinates and Radius of Lateral Femur Sphere	
	Coordinates and Radius of Medial Femur Sphere	Coordinates and Radius of Medial Femur Sphere	
Tibial Lateral plane (position + 2 angles)	=	Tibial Medium plane (position + 2 angles)	=
Tibial Medial plane (position + 2 angles)	=		

5.5.2 LOOCV

The Leave-One-Out Cross-Validation or LOOCV is a procedure to estimate the performance of machine learning algorithms when they are used to make predictions on data not used to train the model. In general, in cross-validation, the entire dataset is split into *k* subsets, which are used as testing sets while all the other subsets train the model. Specifically, in LOOCV the k is equal to the number of measures and defines a methodology for assessing which cases of PCA perform the best prediction. Each column of the matrix M is recursively a testing set, while PCA is calculated with the matrix minus the testing columns. The similarity between the actual and predicted values is measured through the mean squared error (MSE):

$$MSE = \frac{\sum(y_i - f(x_i))^2}{n} \tag{9}$$

where n is the total number of observations, y_i and $f(x_i)$ are respectively the response and the predicted value of the i-th observation. The MSE is calculated for each splitting dataset *k. T*he performance is equal to the mean of the MSE of that specific case. The LOOCV, compared to using a single test set to assess the algorithm efficiency, is less biased because it repeatedly fits the model to a dataset that contains n-1 observations and does not overestimate the mean MSE.

5.5.3 Results

The first five principal components of all the analysed cases account for over 98% of the variance in morphology present in the complete training set, which contains 9 participants. Figure 9 shows the variance for each component and the cumulative variance. However, since the purpose is to reach the highest accuracy without considering computational cost, 8 principal components are used in the LOOCV test.

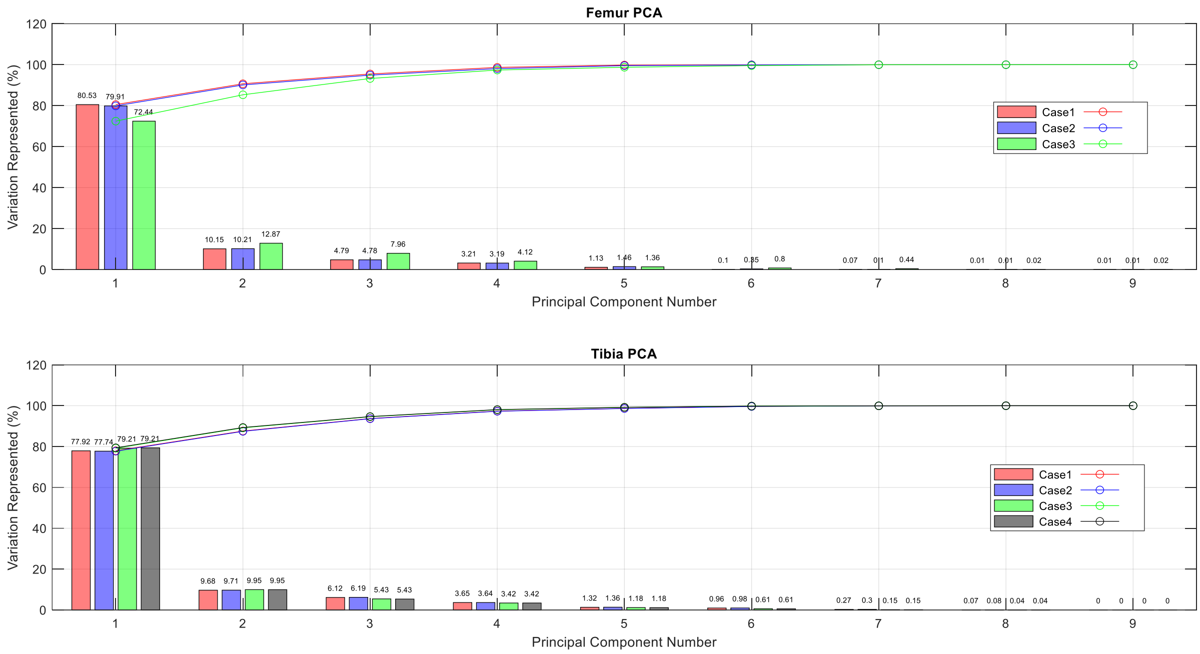

Figure 9 *Variation and cumulative variation represented by principal component number of femur and tibia*

Table 10 *LOOCV femur results*

	Case 1		**Case 2**		**Case 3**	
	Classic PCA	Min.	Classic PCA	Min.	Classic PCA	Min.
1	7.78	39.55	26.92	15.4	31.22	223.96
2	6.62	6.79	9.02	77.31	119.37	254.43
3	16.61	433.12	62.89	100.45	33.49	2377.39
4	19.70	2888.30	71.69	138.86	48.06	62.01
5	12.21	29.52	50.49	29.86	49.54	244.22
6	4.52	6.90	10.56	46.78	50.89	140.08
7	1.05	1.32	0.02	0.47	43.56	44.89
8	5.32	6.37	27.02	34.14	273.45	178.75
9	0.93	0.49	1.07	0.53	74.52	71.87
$\overline{MSE}$	8.3	380.26	9.6	49.31	80.46	399.73

Table 11 LOOCV tibial results

	Case 1	Case 2	Case 3	Case 4
1	22.64	25.21	18.87	21.06
2	51.85	39.36	20.43	24.6
3	52.37	43.21	19.68	26.42
4	108.44	76.64	58.28	60.41
5	98.06	75.57	21.79	70.24
6	16.32	10.53	7.90	11.31
7	3.77	3.31	1.54	1.30
8	78.62	58.87	34.21	47.76
9	3.60	2.96	0.71	0.88
$\overline{MSE}$	48.41	37.29	20.39	29.33

The two resolution methods for determining the principal component scores, i.e. classic PCA and the minimization algorithm, are compared with the LOOCV using the femur training set. Table 10 shows the results of the LOOCV where the number on the left corresponds to the participant whose parameters are predicted using data from the other 8 participants as the dataset.

The classical PCA approach has an $\overline{MSE}$ 5.1 and 4.9 times lower than the minimization algorithm for cases 2 and 3, and the discrepancy is even higher for case 1. Thus, the classical PCA approach performs better and is the only one evaluated for the tibia LOOCV analysis. The results for the tibia are in Table 11.

For the femur, the $\overline{MSE}$ is 8.3 for the case that considers only the spheres coordinates and radius, that increase to 9.6 when adding anthropometric terms. As expected, the case that includes the distance between the spheres is the worst analysed, with an $\overline{MSE}$ of 80.46. The variability over the distance terms makes the prediction more unstable and subject to errors.

For the tibia, case 3 has the best performance, with a $\overline{MSE}$ equal to 20.39. The latter comprehends the femur spheres' centre coordinates and radius, and the coordinates of the medial tibial plane with the corresponding two angles. This case is a good solution because it gathers all the information for assessing the morphological feature of the complete tibia-femoral knee joint. Femoral features are fundamental for increasing the variance of the datasets: case 4, which considers only the tibial medial plane, shows a higher $\overline{MSE}$ (29.33). Similarly, case 2 is performing better than case 1, where only the tibial features are present. Moreover, reducing the feature numbers by substituting the two lateral and medial planes with the mean one is successful because it decreases the parameters to predict and, therefore, the $\overline{MSE}$, especially with a small dataset.

Increasing the dataset numerosity correspond to reducing the $\overline{MSE}$ and diminishing the errors in the prediction. Figure 10 shows the LOOCV result of femur case 1, considering a dataset of 9, 10, and 11 subjects. The $\overline{MSE}$ is lower when the dataset is higher, so likely it is possible to reduce the overall errors by gathering a more numerous knee and marker dataset.

Table 12 shows the absolute error of the worst and the best prediction of sphere centre coordinates and radius for case 1 of the femur and case 3 for the tibia. The worst and the best case correspond to the 4th and 9th subjects for both the femur and tibia: CL and rL indicate the centre and radius of the femur lateral sphere, whereas CM and rM to the medial femoral one. Instead, PM designates a coordinate of a point of the medial tibial plane, and γM and δM the projection angle of the normal vector to the coronal and sagittal femur coordinates system.

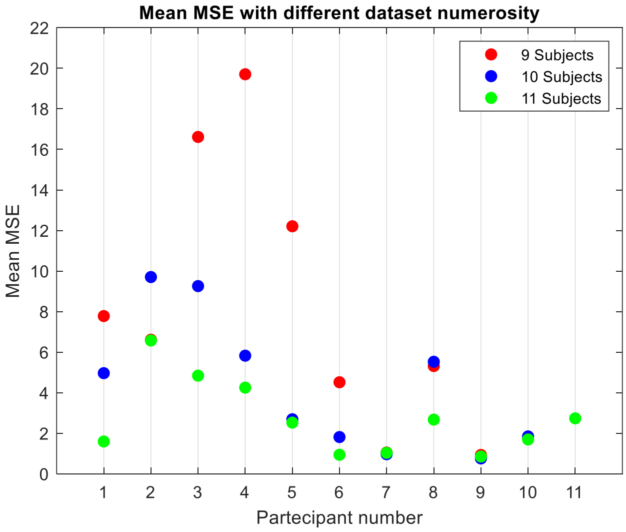

Figure 10 *Variation of* $\overline{MSE}$ *using different numbers of subjects in the dataset*

***Table 12** Absolute error $\left|\boldsymbol{P}_{real} - \boldsymbol{P}_{pred}\right|$ of case 1 for femur and case 3 for the tibia*

		Femur **Case 1**		**Tibia** **Case 3**	
		Worst	Best	Worst	Best
Femur	CLx (mm)	0.73	0.12	0.16	0.009
	CLy (mm)	0.44	0.07	0.04	0.003
	CLz (mm)	10.51	1.81	27.78	1.78
	rL(mm)	1.13	1.4	88.38	4.30
	CMx (mm)	0.6	0.12	0.17	0.009
	CMy (mm)	0.42	0.11	0.03	0.002
	CMz (mm)	3.08	1.82	22.17	1.96
	rM (mm)	0.8	2.43	6.94	3.70
Tibia	PMx (mm)			17.31	11.36
	PMy (mm)			182.09	1.15
	PMz (mm)			118.91	13.58
	γM (°)			11.48	1.21
	δM (°)			237.44	0.31

The highest error is in the prediction of the z coordinates of spheres and plane points, corresponding to the knee medial-lateral axis.

5.6 Conclusions

The work's purpose is to implement an automatic procedure for scaling the morphological features of the tibial-femoral joints using data from experimental markers positioned on anatomical points. Data to feed into PCA algorithms need to be expressed in the same reference system and normalized among all the subjects. Since the only known parameters are the coordinates of the markers, they are used to define the anatomical femur reference system, which is subject-specific and easily identifiable in all the subjects. Instead of using the standard approach, which mathematically estimates the position of HJC, the femur reference system is defined using the marker position of the greater trochanter. The knee surface features are identified from MRI images that contain the partial distal femur bones and the proximal tibial image. An automatic procedure for assessing a meaningful and anatomically significant reference system for the partial bones is defined. Its misalignments with respect to the reference system defined by the greater trochanter are estimated. The misalignment study over seven subjects with total femur, tibia, and fibula bones shows that the angles are stable and similar among the datasets. It confirms the robustness of the automatic algorithm for defining the reference system in partial bones and permits the definition of a correction factor. It is beneficial for translating that custom reference system to the one computed with a more standard procedure.

With the correction angle, the partial bones of the femur are positioned accurately over the experimental setup, thus associating markers' coordinates with the feature of MRI images. Since the relative position of the tibia about the femur is unknown during the marker acquisition, the relative position is computed by a minimization problem. The subject stands up during the data acquisition, and we expect a tibial-femoral angle of around 10°. Minimization results over nine participants confirm that the relative angle is among that range, confirming the validity of the procedure proposed.

For economical and convenience reasons, it is common to scan only partial knee bones with MRI. This automatic procedure is a powerful tool for positioning the anatomical surfaces using the markers set. Specifically, multibody analyses are more performing with subject-specific images. Thus, this procedure is easily implementable into OpenSim or Anybody to increase the automation and goodness of the musculoskeletal model.

If the MRI images are not present, the tibial-femoral features can be predicted with the scaling model developed using the PCA and imported into the software. Precisely, the mean absolute errors over the 9 subject - LOOCV test for the PCA femur case 1 in the prediction of the femur lateral spere are CLx = (0.27 ± 0.33) mm, CLy = (0.18 ± 0.22) mm, CLz = (4.12 ± 5.06)mm and rL = (2.58 ± 3.25) mm, while over the medial spheres are CMx = (0.53 ± 0.72) mm, CMy = (0.6 ± 1.03) mm, CMz = (3.93 ± 4.44) mm and rM = (2.27 ± 2.88) mm. The overall error is always lower than 1 cm, with a maximum STD excursion in the mediolateral axis coordinates. Thus, the prediction of femur spheres using only four markers is precise, performing, and promising. It is demonstrated that the prediction accuracy increases with the numerosity of the dataset: 11 subject-LOOCV results are always lower than the one obtained with fewer participants. Therefore, a primary goal is to increase the number of subjects analysed and diminish even more the overall error.

Increasing the number is particularly necessary for the tibial feature predictions. The tibial model that better performs PCA analysis is the one that substitutes the spheres with corresponding planes. The concavity or convexity of the tibial plateaus makes the sphere variability difficult to control. Nevertheless, the results obtained from replacing the plane are encouraging. Among all the tibia cases analyzed, the one with lower overall error predicts the femoral spheres and the mean tibial plane. In that specific case, the mean absolute errors over the 9 subject – LOOCV of the tibial mean plane are PMx = (58.82 ± 80.59) mm, PMy = (30.30 ± 59.21) mm, PMz = (54.10 ± 54.34) mm, γM = (43.84 ± 70.6)° and δM = (53.92 ± 76.77)°. The overall error is higher and inadmissible to implement in a more advanced setting. However, the procedure remains valid and promising, and future investigation must be done. The number of terms to predict is 8 in the femur PCA, while increments to 13 for the tibia PCA. The PCA feature matrix includes 9 participants, lower than the prediction terms. The corresponding matrix is highly rectangular and unable to perform a good prediction. We are quite sure that increasing the numerosity of the dataset will reduce the overall errors, thus being able to define a scaling law both for the femur and tibia knee joints features.

References

[1] A. Seth, M. Sherman, J. A. Reinbolt, e S. L. Delp, «OpenSim: a musculoskeletal modeling and simulation framework for in silico investigations and exchange», *Procedia IUTAM*, vol. 2, pp. 212–232, 2011, doi: 10.1016/j.piutam.2011.04.021.

[2] A. Scarton *et al.*, «Comparison of lower limb muscle strength between diabetic neuropathic and healthy subjects using OpenSim», *Gait & Posture*, vol. 58, pp. 194–200, ott. 2017, doi: 10.1016/j.gaitpost.2017.07.117.

[3] A. D. Sylvester, S. G. Lautzenheiser, e P. A. Kramer, «A review of musculoskeletal modelling of human locomotion», *Interface Focus.*, vol. 11, fasc. 5, p. 20200060, ott. 2021, doi: 10.1098/rsfs.2020.0060.

[4] F. De Groote e A. Falisse, «Perspective on musculoskeletal modelling and predictive simulations of human movement to assess the neuromechanics of gait», *Proc. R. Soc. B.*, vol. 288, fasc. 1946, p. 20202432, mar. 2021, doi: 10.1098/rspb.2020.2432.

[5] A. Rajagopal, C. L. Dembia, M. S. DeMers, D. D. Delp, J. L. Hicks, e S. L. Delp, «Full-Body Musculoskeletal Model for Muscle-Driven Simulation of Human Gait», *IEEE Trans. Biomed. Eng.*, vol. 63, fasc. 10, pp. 2068–2079, ott. 2016, doi: 10.1109/TBME.2016.2586891.

[6] A. Ottoboni, V. Parenti-Castelli, N. Sancisi, C. Belvedere, e A. Leardini, «Articular surface approximation in equivalent spatial parallel mechanism models of the human knee joint: An experiment-based assessment», *Proc Inst Mech Eng H*, vol. 224, fasc. 9, pp. 1121–1132, set. 2010, doi: 10.1243/09544119JEIM684.

[7] N. Sancisi, D. Zannoli, V. Parenti-Castelli, C. Belvedere, e A. Leardini, «A one-degree-of-freedom spherical mechanism for human knee joint modelling», *Proc Inst Mech Eng H*, vol. 225, fasc. 8, pp. 725–735, ago. 2011, doi: 10.1177/0954411911406951.

[8] R. Di Gregorio e V. Parenti-Castelli, «A Spatial Mechanism With Higher Pairs for Modelling the Human Knee Joint», *Journal of Biomechanical Engineering*, vol. 125, fasc. 2, pp. 232–237, apr. 2003, doi: 10.1115/1.1559895.

[9] S. S. Farshidfar, J. Cadman, D. Deng, R. Appleyard, e D. Dabirrahmani, «The effect of modelling parameters in the development and validation of knee joint models on ligament mechanics: A systematic review», *PLoS ONE*, vol. 17, fasc. 1, p. e0262684, gen. 2022, doi: 10.1371/journal.pone.0262684.

[10] M. Barzan *et al.*, «Development and validation of subject-specific pediatric multibody knee kinematic models with ligamentous constraints», *Journal of Biomechanics*, vol. 93, pp. 194–203, ago. 2019, doi: 10.1016/j.jbiomech.2019.07.001.

[11] K. B. Smale *et al.*, «Effect of implementing magnetic resonance imaging for patient-specific OpenSim models on lower-body kinematics and knee ligament lengths», *Journal of Biomechanics*, vol. 83, pp. 9–15, gen. 2019, doi: 10.1016/j.jbiomech.2018.11.016.

[12] J. P. Charles, F. H. Fu, e W. J. Anderst, «Predictions of Anterior Cruciate Ligament Dynamics From Subject-Specific Musculoskeletal Models and Dynamic Biplane Radiography», *Journal of Biomechanical Engineering*, vol. 143, fasc. 3, p. 031006, mar. 2021, doi: 10.1115/1.4048710.

[13] M. Conconi, A. Leardini, e V. Parenti-Castelli, «Joint kinematics from functional adaptation: A validation on the tibio-talar articulation», *Journal of*

Biomechanics, vol. 48, fasc. 12, pp. 2960–2967, set. 2015, doi: 10.1016/j.jbiomech.2015.07.042.

[14] M. Conconi e V. P. Castelli, «A sound and efficient measure of joint congruence», *Proc Inst Mech Eng H*, vol. 228, fasc. 9, pp. 935–941, set. 2014, doi: 10.1177/0954411914550848.

[15] H. A. Gray, S. Guan, L. T. Thomeer, A. G. Schache, R. de Steiger, e M. G. Pandy, «Three-dimensional motion of the knee-joint complex during normal walking revealed by mobile biplane x-ray imaging», *J. Orthop. Res.*, vol. 37, fasc. 3, pp. 615–630, mar. 2019, doi: 10.1002/jor.24226.

[16] D. L. Benoit, D. K. Ramsey, M. Lamontagne, L. Xu, P. Wretenberg, e P. Renström, «Effect of skin movement artifact on knee kinematics during gait and cutting motions measured in vivo», *Gait & Posture*, vol. 24, fasc. 2, pp. 152–164, ott. 2006, doi: 10.1016/j.gaitpost.2005.04.012.

[17] G. Wu *et al.*, «ISB recommendation on definitions of joint coordinate system of various joints for the reporting of human joint motion—part I: ankle, hip, and spine», *Journal of Biomechanics*, vol. 35, fasc. 4, pp. 543–548, apr. 2002, doi: 10.1016/S0021-9290(01)00222-6.

[18] G. Wu e P. R. Cavanagh, «ISB recommendations for standardization in the reporting of kinematic data», *Journal of Biomechanics*, vol. 28, fasc. 10, pp. 1257–1261, ott. 1995, doi: 10.1016/0021-9290(95)00017-C.

[19] A. Cappozzo, «Gait analysis methodology», *Human Movement Science*, vol. 3, fasc. 1–2, pp. 27–50, mar. 1984, doi: 10.1016/0167-9457(84)90004-6.

[20] A. Leardini *et al.*, «Validation of a functional method for the estimation of hip joint centre location», *Journal of Biomechanics*, vol. 32, fasc. 1, pp. 99–103, gen. 1999, doi: 10.1016/S0021-9290(98)00148-1.

[21] A. L. Bell, D. R. Pedersen, e R. A. Brand, «A comparison of the accuracy of several hip center location prediction methods», *Journal of Biomechanics*, vol. 23, fasc. 6, pp. 617–621, gen. 1990, doi: 10.1016/0021-9290(90)90054-7.

[22] M. E. Harrington, A. B. Zavatsky, S. E. M. Lawson, Z. Yuan, e T. N. Theologis, «Prediction of the hip joint centre in adults, children, and patients with cerebral palsy based on magnetic resonance imaging», *Journal of Biomechanics*, vol. 40, fasc. 3, pp. 595–602, gen. 2007, doi: 10.1016/j.jbiomech.2006.02.003.

[23] H. Kainz, C. P. Carty, L. Modenese, R. N. Boyd, e D. G. Lloyd, «Estimation of the hip joint centre in human motion analysis: A systematic review», *Clinical Biomechanics*, vol. 30, fasc. 4, pp. 319–329, mag. 2015, doi: 10.1016/j.clinbiomech.2015.02.005.

[24] G. Durastanti, A. Leardini, S. Siegler, S. Durante, A. Bazzocchi, e C. Belvedere, «Comparison of cartilage and bone morphological models of the ankle joint derived from different medical imaging technologies», *Quant. Imaging Med. Surg.*, vol. 9, fasc. 8, pp. 1368–1382, ago. 2019, doi: 10.21037/qims.2019.08.08.

[25] C. Mazzotti, N. Sancisi, e V. Parenti-Castelli, «A Measure of the Distance Between Two Rigid-Body Poses Based on the Use of Platonic Solids», in *ROMANSY 21 - Robot Design, Dynamics and Control*, vol. 569, V. Parenti-Castelli e W. Schiehlen, A c. di Cham: Springer International Publishing, 2016, pp. 81–89. doi: 10.1007/978-3-319-33714-2_10.

[26] F. L. Markley, Y. Cheng, J. L. Crassidis, e Y. Oshman, «Averaging Quaternions», *Journal of Guidance, Control, and Dynamics*, vol. 30, fasc. 4, pp. 1193–1197, lug. 2007, doi: 10.2514/1.28949.

[27] W. A. Marshall e J. M. Tanner, «Variations in the Pattern of Pubertal Changes in Boys», 1970.

[28] W. A. Marshall e J. M. Tanner, «Variations in pattern of pubertal changes in girls», *Archives of Disease in Childhood*, vol. 44, fasc. 235, pp. 291–303, 1969, doi: 10.1136/adc.44.235.291.

[29] M. Conconi, N. Sancisi, e V. Parenti-Castelli, «Prediction of Individual Knee Kinematics From an MRI Representation of the Articular Surfaces», *IEEE Trans. Biomed. Eng.*, vol. 68, fasc. 3, pp. 1084–1092, mar. 2021, doi: 10.1109/TBME.2020.3018113.

[30] J. T. Lynch *et al.*, «Statistical shape modelling reveals large and distinct subchondral bony differences in osteoarthritic knees», *Journal of Biomechanics*, vol. 93, pp. 177–184, ago. 2019, doi: 10.1016/j.jbiomech.2019.07.003.

[31] M. T. Y. Schneider *et al.*, «Men and women have similarly shaped carpometacarpal joint bones», *Journal of Biomechanics*, vol. 48, fasc. 12, pp. 3420–3426, set. 2015, doi: 10.1016/j.jbiomech.2015.05.031.

[32] I. Joliffe e B. Morgan, «Principal component analysis and exploratory factor analysis», *Stat Methods Med Res*, vol. 1, fasc. 1, pp. 69–95, mar. 1992, doi: 10.1177/096228029200100105.

[33] J. K. Moore, J. D. G. Kooijman, A. L. Schwab, e M. Hubbard, «Rider motion identification during normal bicycling by means of principal component analysis», *Multibody Syst Dyn*, vol. 25, fasc. 2, pp. 225–244, feb. 2011, doi: 10.1007/s11044-010-9225-8.

[34] C. M. Saliba, A. L. Clouthier, S. C. E. Brandon, M. J. Rainbow, e K. J. Deluzio, «Prediction of Knee Joint Contact Forces From External Measures Using Principal Component Prediction and Reconstruction», *Journal of Applied Biomechanics*, vol. 34, fasc. 5, pp. 419–423, ott. 2018, doi: 10.1123/jab.2017-0262.

Conclusions

This thesis deals with methodologies and protocols for preventing workers' musculoskeletal disorders with wearable inertial sensors. In particular, an IMU MoCap system made of 17 IMUs, is used to assess the OCRA index. It is an ergonomics standard for reducing worker's injuries for repetitive and low loads industrial tasks, by calculating several risk factors among which posture and force multipliers. The first one is measured by estimating the percentage of time in which the worker's upper-limb angle joints exceed the limits imposed by the normative. The Standards suggest three different methods for estimating the force multipliers: using the Borg Scale, EMG sensors, or by the ratio between the estimated force over the hand and the one specified by EN 1005-3 in precise and common working positions. While the posture multiplier is easily identifiable with IMU MoCap algorithms and is simply definable in real-time, the force multiplier computation is not straightforward. Thus, we propose two different methodologies for determining this value. The first one uses AMS, a multibody modelling software with a detailed and validated upper-limb musculoskeletal model, by substituting the EMG signal with the muscle activity estimated by the simulation. The second one is derived by the ratio between the upper-limb joint moments computed online using the IMUs and a force/torque sensor, by a maximal admissible torque estimate by some assumption of EN 1005-3. The two assessments show similar results in estimating the force multiplier in a collaborative robot scenario, where a commercial cobot assists the workers in performing four holes in a laboratory test. This promising outcome validates the online algorithm for dynamic estimation of upper-limb wrenches as a powerful tool for assessing ergonomics evaluation in real-time in industrial scenarios. The latter, even if the algorithm is upgradeable with reductive and subject-specific musculoskeletal models, represents an innovation in ergonomics assessments. An extensive literature review has shown that no studies have performed a dynamic evaluation of force multiplier using IMUs and force/torque sensors in real time.

Another novelty of this thesis is using AMS for estimating the physical-human robot interactions under different cobot control algorithms. Through this study, the advantages of using collaborative solutions for reducing loads and awkward postures on the workers are estimated with AMS. The joint angles and the muscle activities exerted in a standard drilling task are compared with the one obtained with a cobot controlled with admittance control and gravity compensation and one with a velocity controller that moves the EE in the drilling directions. This study's results confirm that the cobot supports the workers' upper limbs by drastically reducing the load over the joints and activity of the shoulder muscle and forces the workers to maintain safer postures during the operation. Thus, cobots are promising tools for diminishing the worker's efforts and preventing musculoskeletal disorders, particularly if used as assistance devices for repetitive tasks.

In general, IMU MoCap systems, if well calibrated, has high performances in ergonomics assessments. For a precise estimation of the position of the workers, proper sensor-to-segment calibration is needed. In this thesis, we proposed a novel calibration method only by using the orientation outputs of each sensor, thus reducing the number of signals to send to the workstation and cutting down the latency of the entire system. After comparing different procedures, the more performing pipeline consists of performing three static poses, namely the T-pose, N-pose, and C-pose, and correcting the initial estimation with controlled functional movements of the elbow and wrist. This procedure outputs joint angles that have errors comparable with other methods proposed in the literature, confirming its validity for correctly estimating the human kinematic. IMUs are wearable, compact, and lightweight and could be worn by workers during the day and constantly track motion and used as preventive devices for diminishing musculoskeletal disorders. As a future development, visual or auditive signals could be integrated with the IMU MoCap systems and warn the workers if potentially dangerous situations are occurring. Moreover, IMUs are an effective alternative to vision systems to ensure no collision with the cobot during a collaborative task. They show a robust motion estimation that could be used to command cobot joint torques to avoid unexpected and hazardous collisions with the cobot.

To increase even more the accuracy of IMU MoCap systems two possible strategies could be performed: an accurate calibration of the gyroscope and accelerometer to have more stable attitude estimation, and a subject-specific musculoskeletal model with more complex kinematic joints model to filter out noises and errors of IMU MoCap algorithm. In those directions, we proposed a low-cost calibration of gyroscope and accelerometer sensors using the free-fall motion of a pendulum, and a reduced and subject-specific biomechanical model gathering joint axis directions with functional movements. While the first study shows promising results, the second one is only partially implemented offline in Matlab, and as future developments, more experiments for determining the actual improvements of this model over a more standard one are needed.

It is universally accepted that the more the biomechanical model describes the properties of the human body evaluated, the more the kinematics and dynamics results describe the actual human behaviours. Thus, as a final part of this extensive work for ensuring safety at work, an automatic method for scaling sophisticated and subject-specific joint models from markers position is developed using PCA. By using the positions of only four markers near the knee is possible to determine, with a good approximation, the position and radius of the two spheres in the femur and the position and normal direction of a plane in the tibia that fully describe the tibial-femoral joints with more details. The results are promising; however, it is proven that the prediction accuracy can increase even more with a higher number of studied populations.

In conclusion, in this thesis, different strategies for preventing workers' musculoskeletal disorders are outlined, tested, and validated in laboratory settings. The next step is to perform the same studies in working scenarios, thus evaluating the effective feasibility of the proposed methods in real life.

Acknowledgments

First, I want to extend my sincere thanks to my supervisor, Prof. Nicola Sancisi, who fully supported me during this period with patience and kindness. It was a pleasure to learn from your experience and share this journey with you.

I must thank Prof. Vincenzo Parenti Castelli, who, during the master's thesis, was the first to believe in me and convince me to embark on this career. Working with you on the patents of the laparoscopic instrument was challenging and thrilling, and it is one of the results to be prouder of.

I want to thank Prof. Daniel Benoit, who had the great humanity to accept me in his group as a remote student with very little forewarning. The weekly meeting made me feel part of the group, even if it was behind a screen.

Thanks to Prof. Nicola Francesco Lopomo and Prof. Giacomo Palmieri for their technical and editorial support during the thesis writing process.

Moreover, I want to thank Prof. Michele Conconi for his helpful and concrete suggestions, especially in the last part of the program, and Prof. Rocco Vertechy to have hosted me in the Saima Lab in Monte Cuccolino.

Working with the view of the hills of Bologna boosted my energy and gave me the possibility to share the experience with a fantastic group of people: Lorenzo, with his tireless desire to create the best, Chen for his deep knowledge and patience to teach me, Marco, with its irony and unconditional availability, Nicolo, with its ability to say the wrong thing at the right time, Emanuele, for his strength and good pieces of advice, Federico, with his kind and sweet words, Eugenio, for his priceless help with the robot, and Guido, Luca, Amedeo, Riccardo, and Marcello for sharing laughs and fun during the lunches and breaks. Thank you for being with me through thick and thin. Thanks also to Alessandro for making the last year funny and full of great discussions.

Finally, I want to thank all the people who crossed my path in the last three years enduring and supporting me during my stressful moments. Thank you all for being with me: you were great companions. A special thanks to my family, who were tested by the hardness of life in the last year. This result is for you, Tiziana, Matteo, and Maria, and in memory of who is not more with us.